論文 / 著書情報
Article / Book Information

題目(和文)	リチウムイオン電池の正極合材中における界面反応
Title(English)	Interfacial Reaction in Cathode Matrix of Lithium Ion Batteries
著者(和文)	梶山亮尚
Author(English)	Akihisa Kajiyama
出典(和文)	学位:博士(工学), 学位授与機関:東京工業大学, 報告番号:甲第10032号, 授与年月日:2015年12月31日, 学位の種別:課程博士, 審査員:菅野 了次,大坂 武男,北村 房男　,中村 二朗,平山 雅章
Citation(English)	Degree:Doctor (Engineering), Conferring organization: Tokyo Institute of Technology, Report number:甲第10032号, Conferred date:2015/12/31, Degree Type:Course doctor, Examiner:,,,,
学位種別(和文)	博士論文
Type(English)	Doctoral Thesis

Interfacial Reaction in Cathode Matrix of Lithium Ion Batteries

（リチウムイオン電池の正極合材中における界面反応）

Akihisa KAJIYAMA

Dissertation

Submitted to the Department of Electronic Chemistry
Interdisciplinary Graduate School of Science and Engineering
Tokyo Institute of Technology
In Partial Fulfillment of the Requirement for the Degree of

Doctor of Engineering

Tokyo Institute of Technology
September 2015

Contents

Chapter 1. Introduction

1.1. Preface

The demand for Li-ion batteries has increased as new portable electronic devices continue to be developed. For example, a rechargeable Li battery with a $LiCoO_2$ positive electrode was reported by Mizushima and Goodenough et al. [1] that is suitable for practical applications. In addition, this technology has become established as a promising power sources not only for mobile devices but also for more important applications such as electric vehicles (EVs) that emit zero CO_2.

Furthermore, the commercialization of Li-ion batteries that can power entire homes has also been proposed recently. This application was inspired by the serious earthquake that struck Japan in 2011, which was followed by the long-term shut down of the electrical supply. In this context, the development of energy storage systems (ESSs) that could enable us to stockpile enough energy to power an all-electric house has begun. It is not uncommon that a house might be powered by a combined ESS that includes solar batteries that enable increased electrical self-sufficiency, and the excess electricity produced by such combined systems could be sold to energy suppliers. A self-sufficient system's applications can be further expanded by combining it with the EV described above. Some EVs that exhibit energy densities equivalent to that required to power a private home for one night have appeared on the market.

One reason for this rapid growth of the demand for Li-ion batteries could be the development of new fine ceramic materials since the 20th century. The reported results of interface studies are also an important contributor to this increase. In fact, these studies have been playing an important role in achieving control of the many potential side reactions hindering the commercialization of Li-ion batteries.

One example of the result of impactful interface study is as follows: In primary Li metal batteries, the interface between the Li metal negative electrode and the electrolyte is stabilized by a protective film known as the solid electrolyte interphase (SEI), which is a byproduct produced by the reaction of a small amount of H_2O and the impurities in the electrolyte. [2]

In contrast, secondary Li batteries initially showed poor reversibility because of

the repetitive consumption of Li^+ ions. The cycle of the electrochemical dissolution and deposition of Li^+ in these systems resulted in inactive byproducts. Furthermore, because Li^+ deposition to generate Li metal following dendrite generation tends to be inhomogeneous, Li-ion batteries had exhibit internal short circuiting through adjacent microspores of the separator.

One solution for these interfacial problems is the use of a material that contains Li^+-storage sites in its structure. Yazami et al. and many researcher who presented at the International Meeting for Lithium Batteries in 1982 [3] reported that graphite can electrochemically intercalate and de-intercalate Li^+ ions. As a result, carbon electrodes have become popular negative electrodes in Li-ion batteries.

As the demand for Li-ion batteries is continuously increasing, the requirements for these batteries are also continuously expanding, including higher energy density, longer life, higher power, improved safety, and better cost performance. To obtain higher energy batteries, the most common method is to increase the electrical capacity by increasing in the number of reversible Li^+ ions in conventional electrode active materials. However, because most of these materials have an ordered rock salt structure (R-3m), which consists of alternating Li^+ and MO_2 layers, they exhibit instability in their crystal structures. Indeed, the excessive removal of Li^+ from the crystal structure will actually decrease the battery's capacity. [4]-[8] And more, increasing the Li^+ extraction also increases the electrochemical potential of the cut off voltage of cathode active material.

Figure 1 shows the energy maps of various active materials, in which the horizontal axis shows the electrical capacity and the vertical axis shows the potential vs. Li^+/Li. Because the energy is a product of these dimensions, it can be determined using the inversely proportional curve. As can be seen in this figure, increasing the cut-off charging voltage from 4.3 V, as used in conventional devices, to 4.4 or 4.5 V versus Li^+/Li could result in a $LiCoO_2$ (LCO) energy density comparable to that of Li_2MnO_3-$Li(Ni,Co,Mn)O_2$ (HE), a so-called high-energy material.

In this context, many of the efforts aimed at material development in this field have focused on active materials with R-3m structures such as LCO, NCA, and $Li(Ni,Co,Mn)O_2$ (NCM). Additionally, Ni-rich NCA and NCM have been produced recently.

Moreover, some promising positive electrode materials that could achieve higher energy densities, such as $LiNi_{0.5}Mn_{1.5}O_4$ (HV spinel), have been investigated. The driving

force of the motors used in EVs depends on the voltage of the power source. HV spinel could reduce the cell number in the series of unit cells in the battery pack because of its high voltage and, thus, increase the free space in the vehicle. However, before this material can be further developed for practical applications, some problems caused by interfacial side reactions resulting from its high voltage [9]-[16], must be solved.

As mentioned above, the increase in state of charge result in the increase in the cut off voltage of the battery charging, with conventional active material use. Thus, it is quite important and strongly required to take protective care for the high voltage regardless to conventional R-3m materials or next generation HV spinel. The interfacial environments of the cathode active materials in battery cells include both the interaction between the solid-liquid interface and the organic electrolyte and that between the conductive agent and the binder. These interactions are the subject of many studies.[17]-[39] because it is very important to understand the resulting reactions to make effective improvements. As the voltage increases, the side reactions also increase, and as a result, some unwanted effects such as collapse of the crystal structural, electrolyte decomposition, and generation of a resistive film in the interface will occur more frequently.

In summary, the research and development efforts relating to the commercialization of Li-ion batteries have tied to break through the trade-off between the stability of the crystal structure as Li^+ extraction increases and the high-voltage durability.

1.2. Benchmarking of various active materials: Crystal structure, capacity, power, safety, cycle life, and cost performance

1.2.1. Structural comparison

In this section, the benchmarking of various materials is described, and all syntheses and electrical studies of these materials were performed by our group. Table 1 lists some major cathode active materials that exhibit the following crystal structures: layered (ordered rock salt) (R-3m), spinel (Fd-3m), and olivine (pmnb). HE is listed at the boundary between R-3m and Fd-3m because it exhibits a phase transition from an R-3m-like phase to Fd-3m-like one during the first charging.

Table 1 Summary of the cathode active material data sorted by its structure.

structure	Layered (R-3m),hexagonal				Spinel (Fd-3m), cubic		Olivine (Pmnb), ortho.	
Material	$LiCoO_2$ (LCO)	$Li(Ni,Co,Al)O_2$ (NCA)	$Li(Ni,Co,Mn)O_2$ (NCM111)	Li_2MnO_3-NCM (HE-LNMC)	LiMn-spinel (LMO)	Li(Ni,Mn)-spinel (LNMO)	$LiFePO_4$ (LFPO)	$Li(Mn,Fe)PO_4$ (LMFPO)
Cut-off	3.0-4.3			2.0-4.6	3.0-4.3	3.0-5.0	2.0-4.3	2.0-4.5
Average Voltage	3.97	3.72	3.74	3.60	3.80	4.75	3.16	3.71
Charge (mAh/g)	163.8	215.9	177.4	326.1	106.9	150.4	166.2	158.5
Discharge (mAh/g)	154.9	185.4	160.3	276.8	105.4	146.5	162.3	156.6
Efficiency (%)	94.6	85.9	90.4	84.9	98.6	97.4	97.6	98.8

1.2.2. Energy density

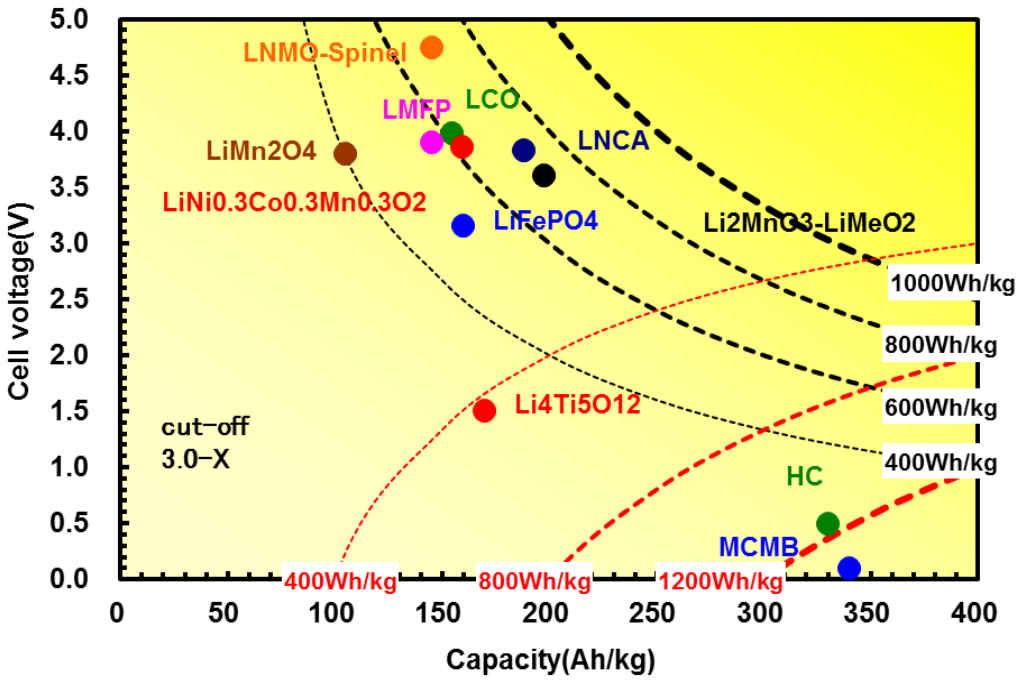

Figure 1 Energy Map of various cathode active material all materials were produced by BASF TODA and the evaluation have also been made by BASF TODA.

In academic circles, batteries' capacities are reported in terms of mAh g^{-1}. However, for practical device applications, batteries powers' must be determined in terms of Wh, as shown in Figure 1. As mentioned above, energy density can be calculated using the inversely proportional curve. On such a plot, the upper right quadrant and lower right quadrants are the optimal areas for the cathode and anode, respectively. Plotting the power Wh g^{-1} is particular relevant for EV applications because automobile manufacturers make decisions regarding the parts to use in their vehicles based on cost per weight.

From the mobile device perspective, the volume the battery occupies within the electrical device is an important parameter. Therefore, mobile phone manufacturers discuss the energy density as a function of Wh per volume. Figure 2 presents a map showing the volumetric energy, which indicates the usability of high-true density materials such as LCO and NCA. HV spinel is predicted to be located in the high-energy region because it shows the highest voltage and was best able to compensate for the low electrical capacity. HE also appeared to be a promising material because of its high electrical capacity.

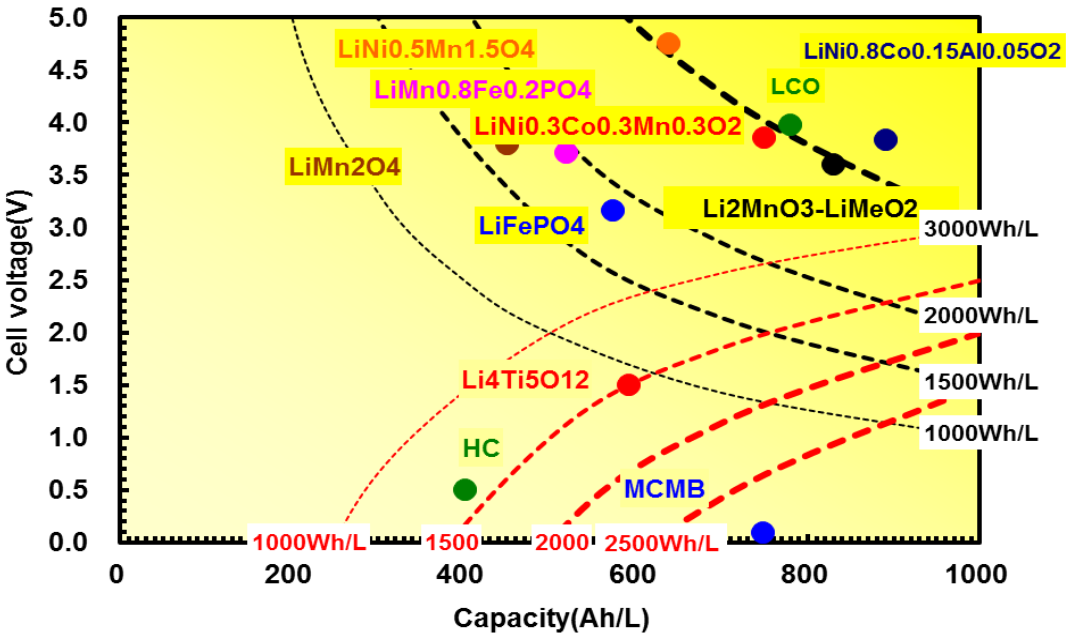

Figure 2 Energy Map (Ah L^{-1}) (All Materials have been made and evaluated by BASF TODA).

1.2.3. Power

Figure 3 shows the voltage profiles during discharge at discharging rates of 0.1, 1, 2, and 5 C. Figure 4 shows the discharge capacity results for all the C rates tested. Regarding the power, these figures indicate that the Li^+ ion's anisotropic diffusion was more important than its characteristic ionic conductivity, as reported previously [1], [40]-[46]. We believe that the reason for this difference can be attributed to the R-3m structure of the materials, even though this structure contains a two-dimensional free-Li^+ ion diffusion path within its crystal framework. However, these materials could have sufficient possibility because the diffusion coefficient can be increased as the cross-sectional area of the Li^+-diffusion path and, thus, the charge state increase during Li^+ extraction. A characteristic property of these materials is that the crystal's c axis increases with the charge state because the attraction of the adjacent oxygen anion to the Li^+ static charge gradually changes to repulsion as Li^+ extraction proceeds.

As described in Chapter 2, the design of particle structures that enhance battery performance must ensure an anisotropic Li^+-diffusion direction.

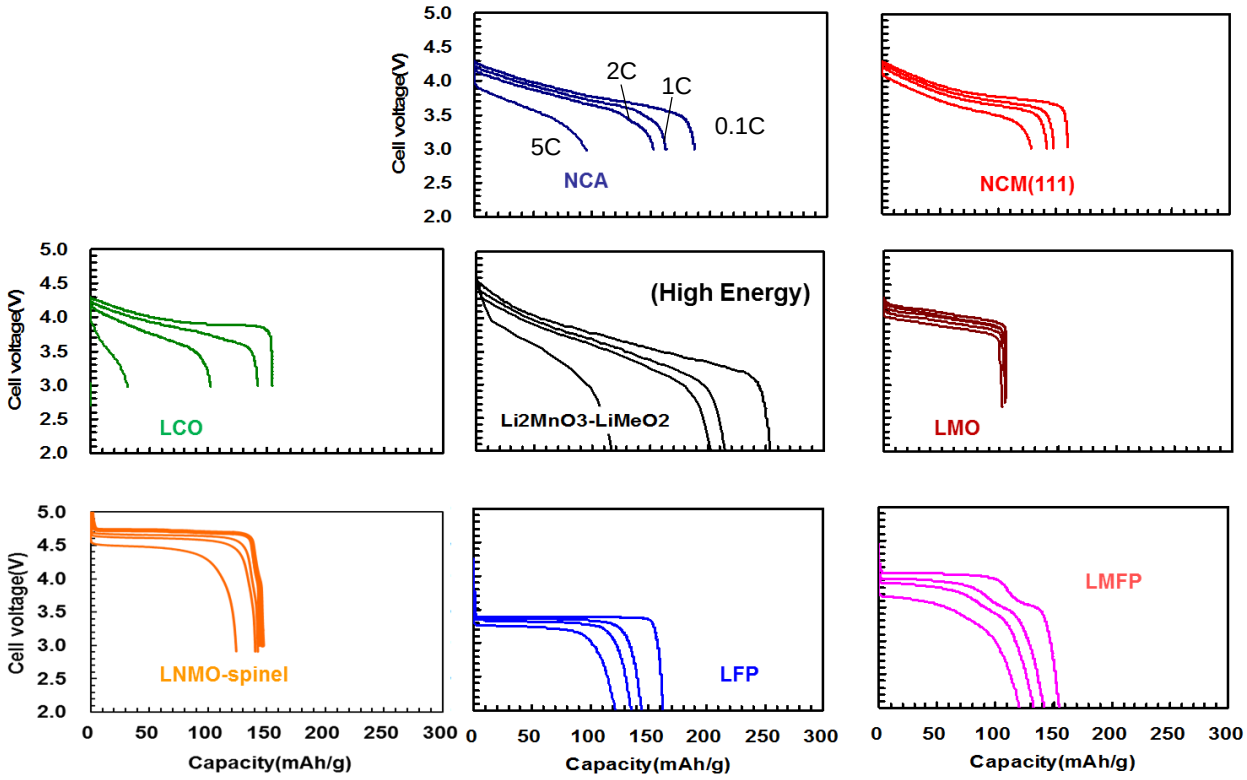

Figure 3 Voltage profile of various electrode materials during discharge with various C-rate.

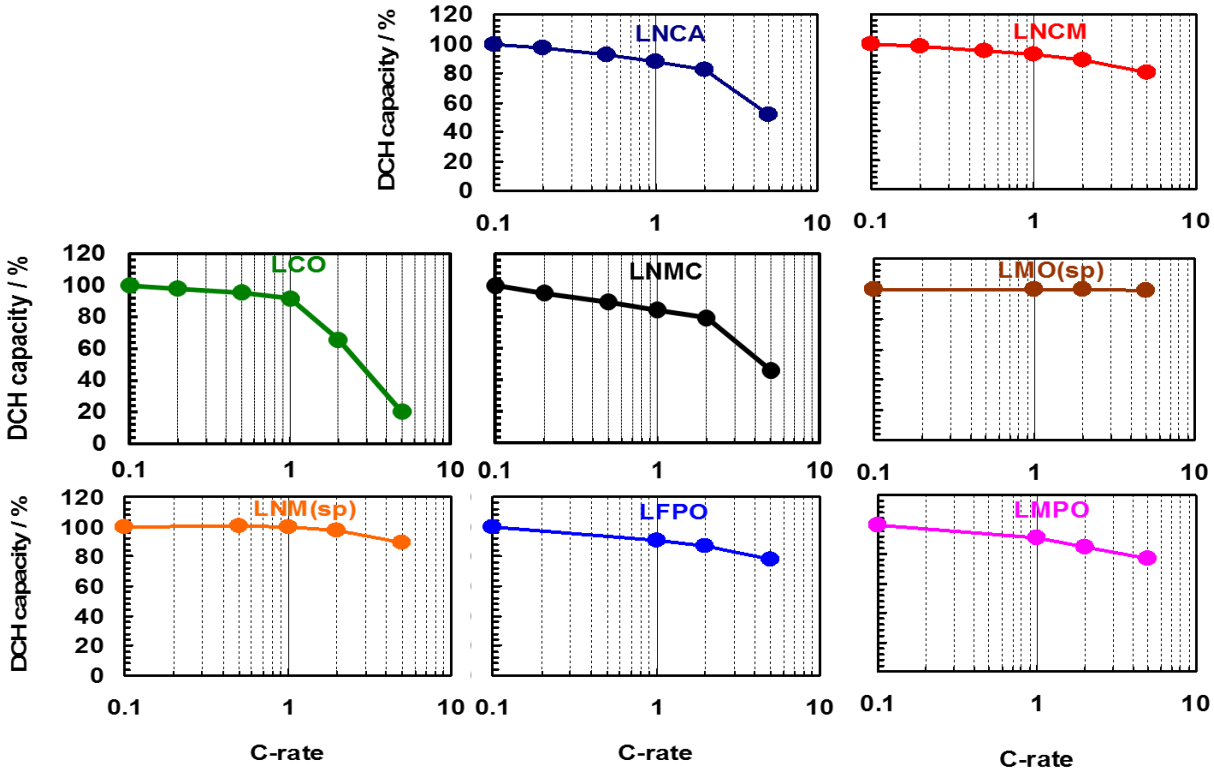

Figure 4 Discharge capacity of various electrode materials under various C-rate.

1.2.4. Cycle life

The cycle life is the main focus of this thesis and will be described in detail in Chapter 2. From the consumer's perspective, the cycle life is equivalent to the battery life and is an important property, especially for EVs because the cruising range depends on it. If the cycle life is poor, the vehicle may not be able to reach the desired destination, even it could have when the vehicle's battery was new. Additionally, under these conditions, the operator may need to turn off the air conditioner or navigation system to ensure reaching the desired destination.

As manufacturers of these materials, we have a different perspective from that of manufacturers who apply these materials to produce other goods. We supply materials to the market after complete analysis, including determining the nature of each material and its productivity, cost performance, and safety issues.

When focusing exclusively on the cycle performance, the most promising active materials appear have spinel and olivine structures, which are three-dimensionally stable.

The same observation can be made for the anode material $Li_4Ti_5O_{12}$ spinel (LTO). This structure is more stable than other three-dimensional materials because its volume change during charge and discharge is almost zero due to the fact that the ionic radii of Ti^{4+} and Ti^{3+} are equivalent. Furthermore, this material does not exhibit capacity degradation resulting from Mn^{2+} dissolution, unlike graphite. Hence, combinations of these three-dimensional-framework cathode and anode materials show the excellent cycle lives. Currently, a battery system consisting of a LCO cathode and a LTO anode is used as a backup energy source in EVs. However, this system cannot be used as the primary battery because of the LTO anode's relatively high redox potential, which reduces the battery voltage, and its relatively low energy density.

As described above, LCO, NCA, and NCM are promising candidate cathode active materials that could be developed in the near future. Although they appear to be similar to classically used materials, their high energy densities, which are comparable to those of HE, are extremely attractive for practical applications. In particular, the Ni-containing R-3m materials NCA and NCM are Ni- and Mn-substituted, stable variations of LCO, and they are currently being developed to achieve deep charge states. These materials could exhibit three-dimensional anisotropic free-Li diffusion despite their two-dimensional diffusion crystal structure and relatively high cut-off voltage through a unique particle design, as described in Chapter 2.

1.2.5. Safety

Figure 5 shows the heat stability data measured with Differential Scanning Calorimetry (DSC) by ourselves. Each materials were once charged to the state of charge of 100% in the coin cell, then obtained by cell de-assembling. Obtained cathode and 0.4 μl electrolyte were enclosed in closed stainless steel pan that has high pressure durability after the rinse with De-methyl Carbonate (DMC).

Figure 5 shows the heat-stability data obtained using differential scanning calorimetry (DSC) in this work. All of the materials were charged to 100% charge state in a coin cell and then retrieved by disassembling the cell. 4mg of the retrieved cathode and 0.4 μL of electrolyte were placed in a 4 mm diameter closed stainless steel pan with high-pressure durability after being washed with dimethyl carbonate (DMC).

$LiFePO_4$ was shown to be extremely stable, and LMO was found to exhibit good stability as well. The stability of these materials depends on the charge states of the

transition metal ions (Fe^{3+} and Mn^{4+}). In contrast, LCO and NCA showed relatively poor performance. These materials' higher heat flows during heating were attributed to the instability of the unusual, electrically oxidized Ni^{4+} and Co^{4+}; these ions are rarely observed in nature.Similarly, HE and HV spinels, which also include Ni^{4+} in their charged structures, exhibit poor heat stabilities.

NCM's good potential for applications in high-energy-density batteries can also be seen in Figure 5. Unlike LCO and NCA, the durability of NCM is evidenced by its relatively high onset temperature. The reason underlying this difference is that NCM contains a higher Mn^{4+} concentration than other R-3m materials. However, as will be shown below in Figure 7, the method of increasing the capacity of NCM is increasing the Ni concentration. To compensate for the instability caused by Ni^{4+}, the appropriate balance between Ni and Mn must be determined. Alternatively, NCM's capacity can be increased by doping appropriate elements into the structure or applying an interface coating. Currently, most of these studies remain unreported, but relevant results appear to

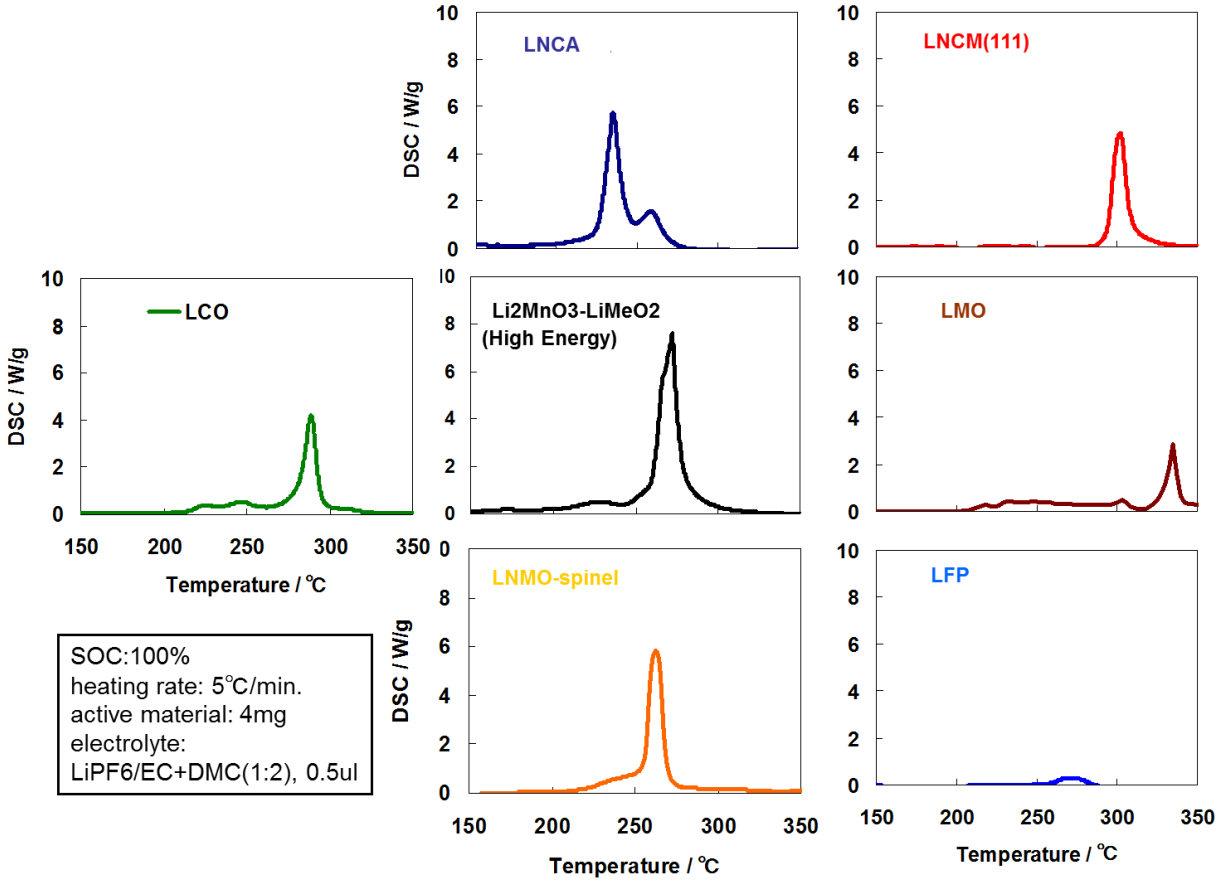

Figure 5 DSC curve of charged positive electrode.

be gradually emerging as patents are granted.

1.2.6. Gas generation (swelling)

Gas generation in batteries results in severe performance degradation, especially in prismatic and laminate cells. Unlike cylindrical cells, these types of cells tend to experience inhomogeneous contact pressure in the electrode plane.

Specifically, the center region of the plane can be easily weakened because of the geometric effects of the cells. Hence, once gas is generated and migrates to the space between the anode and cathode electrodes, it functions as an ionic insulator, thereby decreasing the cell capacity. This phenomenon leads to local overcharge and overdischarge, as observed using disassembled battery cells.

This gas generation can result from excess Li in the cathode active material and moisture contamination from the atmosphere in which the cell was assembled. Although the gas-generation problem has been overcome, it occasionally re-emerges when product manufacturing place start to leave Japan to the other Asian regions. Precise control over manufacturing conditions is required to avoid this problem.

Cathode materials should be developed that are amenable to the high-voltage shifts expected for future batteries. However, the development of these materials is complicated by some issues that cannot be overcome using only the technique described above. Chapter 3 presents some proposed methods to suppress electrolyte decomposition.

1.2.7. Cost

Table 2 lists criteria, which includes typical cost based on raw material costs and processing costs. As shown in Figure 6, LCO is the most expensive, whereas because Mn is a relatively low-cost material, LMO's cost is four times lower. The cost of $LiFePO_4$ (LFP) is not the lowest because of its processing cost: Atmospheric control is required to achieve inert calcination and obtain Fe^{2+}.

Table 2 Evaluation criteria of the rader chart.

		1	2	3	4	5
Energy	Ah/g*V*SD*P	1500≦	<1500	1500-2000	2000-2500	2500≦
Power	retention @ 5C	50≦	<50	40-60	60-90	90≦
Cost	price ∝ raw amterial + processing fee	2500<	≦2500	≦2000	≦1500	≦1000

1.2.8. Rader Chart - Summary of the materials bench marking

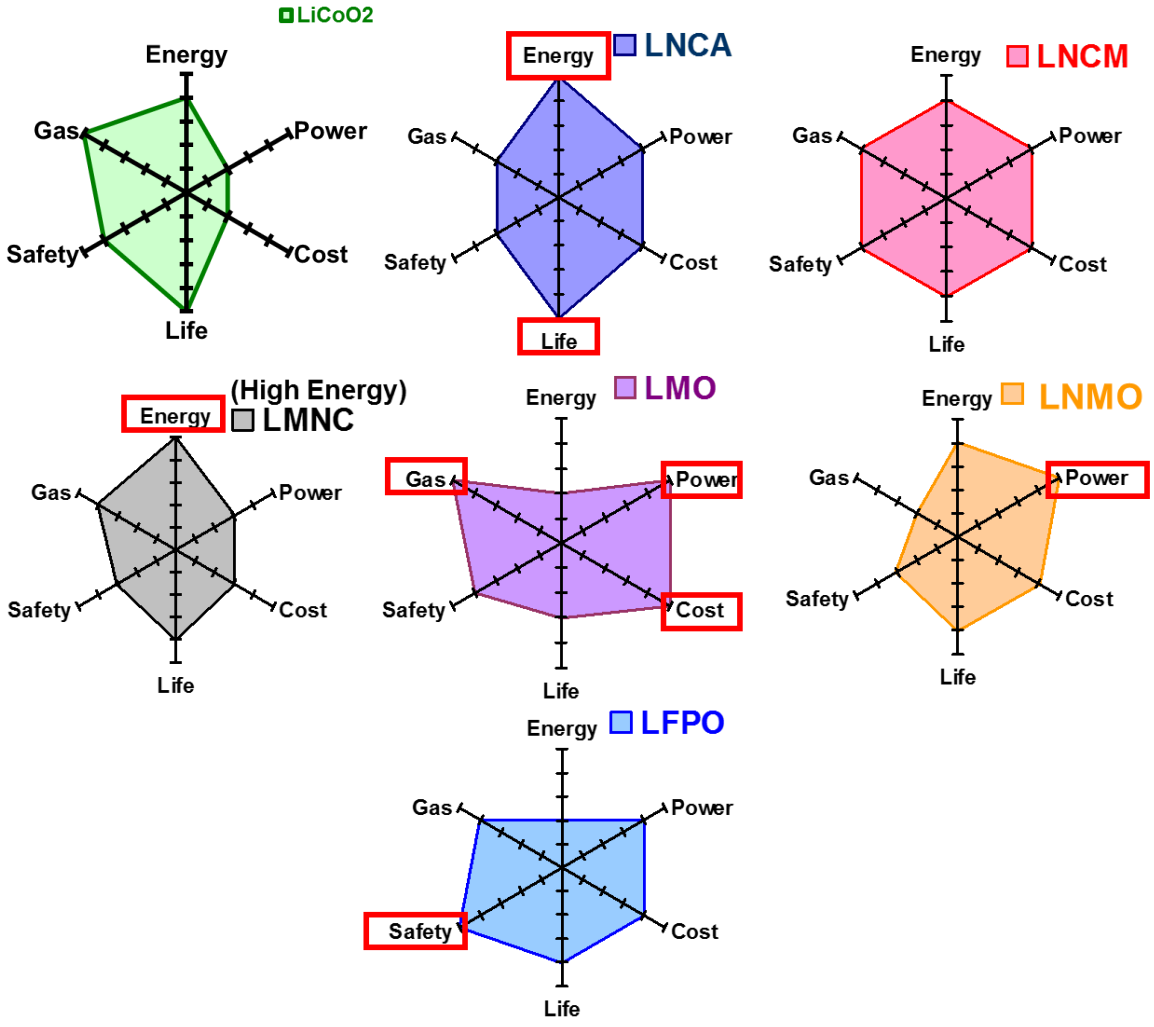

Figure 6 Summary of bench marking (Rader Chart) with some key factors.

Figure 7 is a summary of all above properties. They are quantified on the basis in Table 2 criteria. It shows that there are not full satisfied material so that we should blend

some material in the electrode in appropriate ratio. However, it could be notable the balanced character of NCM hence, it will be most promised material for near future material.

1.3. Purpose of this Thesis

In this section, the purpose of this study is discussed.

- Designing a cathode active material able to endure a deep charge state - substantial Li^+ extraction
  - Structural stability

    To meet the present demand for Li-ion batteries, increasing both the Ni concentration of NCM and the charge state are important research and development areas, as shown in Figure 7. However, both of these goals require increasing the extraction of Li^+ from the active materials. Increasing the extraction of Li^+ from R-3m materials increases the difficulty of maintaining their crystal structures.

    Although the general method to achieve these goals is doping an appropriate element into the structure, this thesis describes an interfacial study of a homogeneous electrochemical reaction to prevent local overvoltage. The capacity-faded battery cells should be disassembled to confirm the presence of some local collapse of the crystalline structure near the interface, a characteristic of local overcharge. Currently, the cut-off charges are not determined based on the equilibrium state of the charge; instead, these values are established based on empirical data, which include many inhomogeneous results. Hence, there is still substantial room for improvement. It would be desirable to describe effective methods experimentally.

  - Controlling interfacial reactions

    One technique to achieve homogeneous Li^+ intercalation and de-intercalation is decreasing the crystallite size of the cathode active materials. Most cathode materials are designed according to the polycrystalline effect to achieve this. However, decreasing the crystallite size has revealed a new problem: particle cracking or exfoliation along the polycrystalline material's grain boundaries. In this thesis, designs that consider grain boundaries as a type

of interface are considered to be quite important. A solution for this problem was determined by subjecting currently commercially available cathode particles to pulsed laser deposition (PLD) membrane experiments.

Studying the techniques used to observe side reactions and collect evidence of interfacial reactions is an important endeavor.

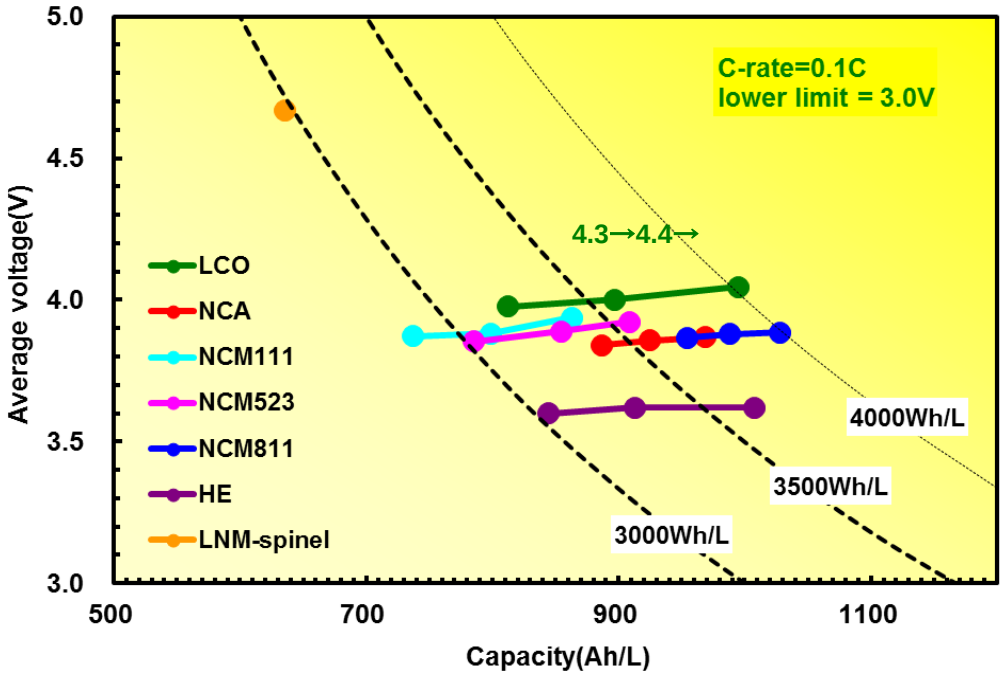

Figure 7 Energy Map of Ni-based Cathode active materials with high voltage use (per volume). Energy could be increased with either Ni content in the NCM material or cut of voltage.

- Material design for high-voltage-durable cathode materials

As mentioned above, deep charging of the battery causes the cut-off voltage to rise. The cut-off voltage has increased from 4.2 V in the 1990s to 4.3 V in 2011 and, finally, to its present value of 4.4 V versus Li+/Li. To avoid potential safety issues, durability at 4.5 V is necessary. However, 4.5 V is no longer the normal point at which the battery components such as the electrolyte, conductive agent, and binder begin to exhibit abnormal reactions. Specifically, this thesis describes the contributions of various conductive agents to gas generation. The interfacial reaction model and the key factor for improvements are also discussed.

- Interaction between active materials and electrolyte.

HV spinel is a useful active material to study the cathode-electrolyte interface in the high-voltage state because it has a redox potential of 4.7 V versus Li^+/Li. The novel results of this investigation were an abnormal electrochemical reaction of the conductive agent and a local battery-like reaction including HV spinel, the electrolyte, and the carbon materials. The proposed reaction is discussed in Chapter 3.

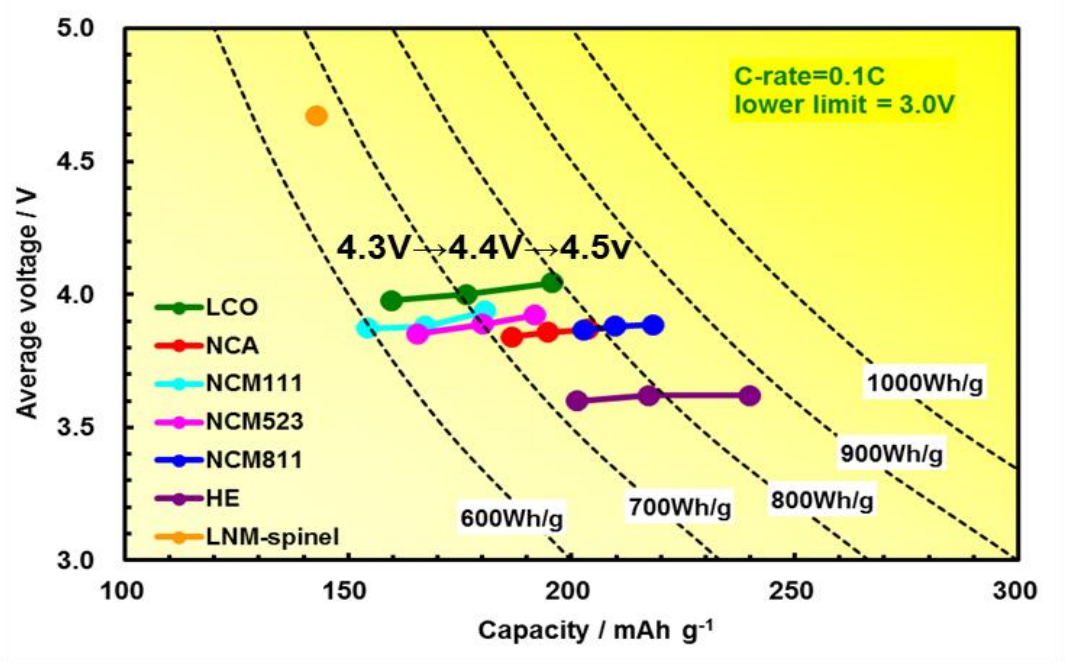

Figure 8 Energy Map of various Cathode active materials (per weight).

Chapter 2. Grain boundary composition effect on battery life

2.1. Grain boundary - important interface to the electrolyte -

2.1.1. Stability of the crystal structure

As described in the previous chapter, there are many positive electrode materials that have an ordered rock salt structure of R-3m. As this material generates its battery capacity by a redox couple of its transition metal along with electrochemical Li^+ intercalation and de-intercalation, Li also plays a role in sustaining its crystal framework. Therefore, the number of Li^+ ions that could be extracted and re-inserted into the host structure without destroying the crystal is quite an important issue when attempting to increase the reversible battery capacity. In this chapter, some of the degradation modes that should be overcome will be described.

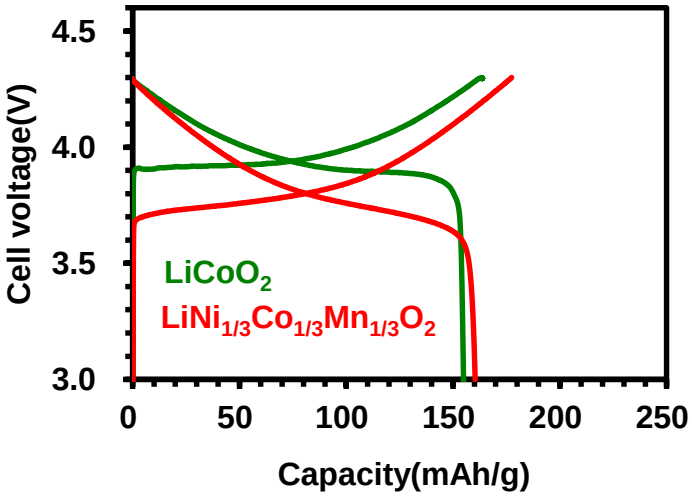

Figure 9 Charge discharge curve of LCO and NCM111.

2.1.2. Durability for deep charging and discharging - increasing in the reversible Li^+ ion

At the Li ion battery's initial commercialization, LCO could only be charged to 4.2 V versus Li^+/Li which is equal to the reversible inter/de-intercalation number of approximately 0.5 Li^+ per unit cell of LCO. The practical capacity was only 140 mAh g^{-1}. After that, several research and development studies were conducted to address the continuous increase of the market needs that produced a material that could be charged

to 4.3 V with a capacity of 160 mAh g^{-1}, which then reached 4.4 V with 175 175mAh g^{-1} [47]. As shown in Figure 10, the NCM charge discharge voltage is lower than that of LCO due to the existence of the redox couple between Ni^{2+} and Ni^{4+}. One major cathode active material of NCM could be designed based on its reversible capacity to not only increase in cut off the charging voltage but also change in its Ni/Co/Mn composition. Specific potential profiles during the charge discharge are shown in Figure 10. Three different compositions of NCM, $LiNi_{1/3}Co_{1/3}Mn_{1/3}O_2$ (NCM111), $LiNi_{0.5}Co_{0.2}Mn_{0.3}O_2$ (NCM523), and $LiNi_{0.6}Co_{0.2}Mn_{0.2}O_2$ (NCM622), are shown in the figure.

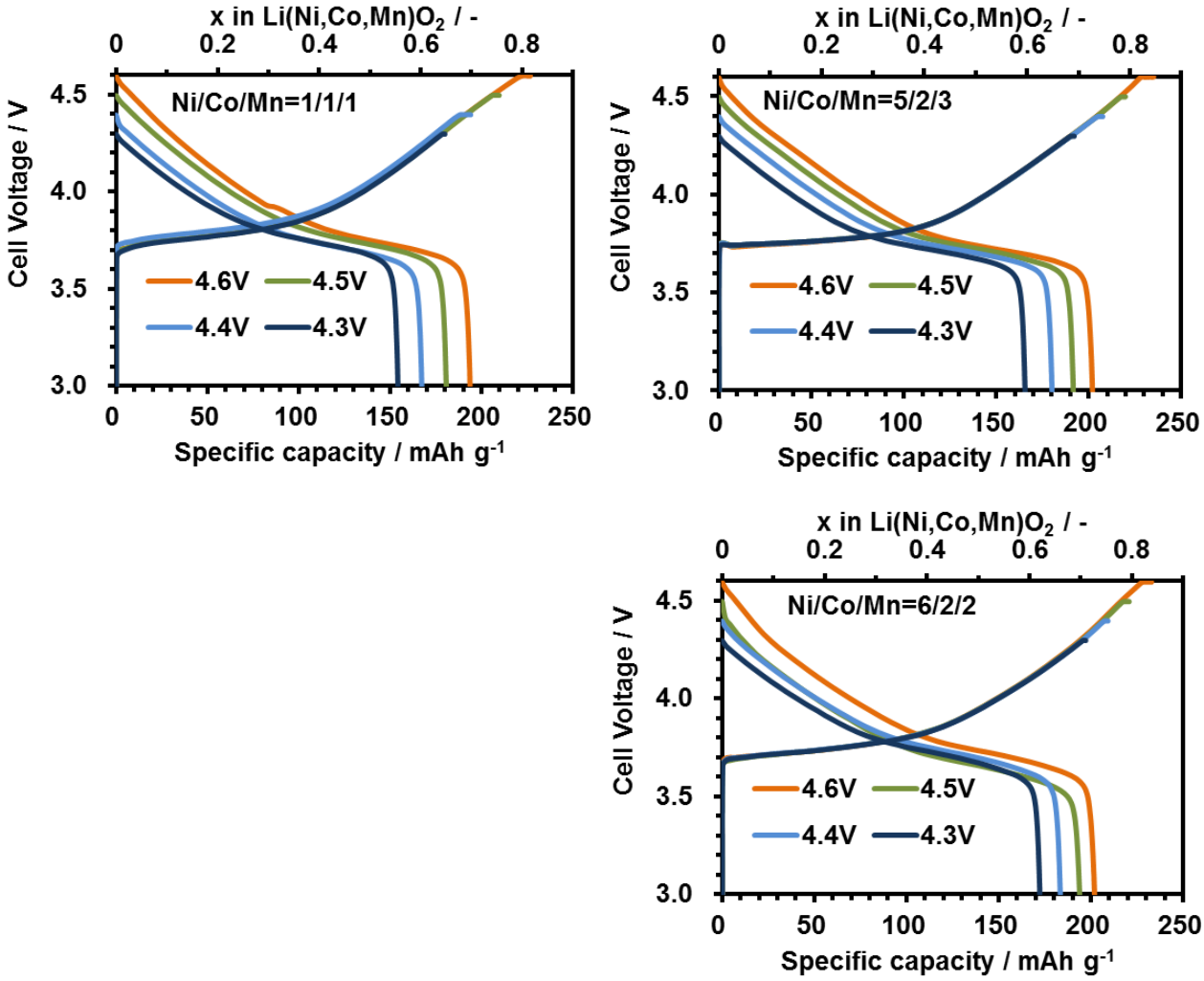

Figure 10 Charge discharge curve of NCM111, 523, 622 with cut off voltage of 4.3, 4.4, and 4.5 V.

The chemical formula of NCM could be described as follows:

$[Li^{+}]_{3a}[Ni^{2+}{}_{\alpha}Ni^{3+}{}_{\beta}Co^{3+}{}_{\gamma}Mn^{4+}{}_{\delta}]_{3b}[O^{2-}{}_{2}]_{6c}$:Space Group R-3m

When $\delta<\alpha+\beta$, the average valence of the 3b site to compensate the charge balance is 3+, and the mixed valence of Ni^{2}+ and Ni^{3+} is balanced by electrochemically inactive Mn^{4+}. Moreover, since the number that fills the 3b site is 1, the electron number required to oxidize the transition metal in the site is 1 regardless of the Ni/Co/Mn ratio in the 3b site. For confirmation, the estimation for NCM111, NCM523, and NCM 622 are listed as follows:

NCM111 : $[Li^{+}]_{3a}[Ni^{2+}{}_{1/3}Co^{3+}{}_{1/3}Mn^{4+}{}_{1/3}]_{3b}[O^{2-}{}_{2}]_{6c}$

NCM523 : $[Li^{+}]_{3a}[Ni^{2+}{}_{0.3}\ Ni^{3+}{}_{0.2}Co^{3+}{}_{0.2}Mn^{4+}{}_{0.3}]_{3b}[O^{2-}{}_{2}]_{6c}$

NCM622 : $[Li^{+}]_{3a}[Ni^{2+}{}_{0.2}\ Ni^{3+}{}_{0.4}Co^{3+}{}_{0.2}Mn^{4+}{}_{0.2}]_{3b}[O^{2-}{}_{2}]_{6c}$

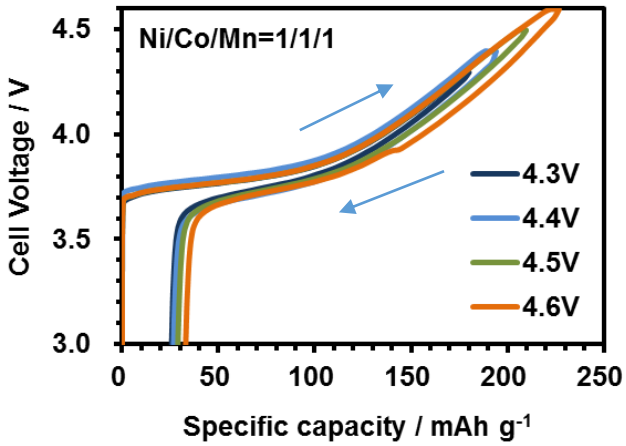

Figure 11 Charge discharge round trip curve of NCM with varous cut off voltage.

Because the possible electrochemical reaction to the full charge of 4+ is 1 for all compositions, the theoretical capacities of the compositions are almost the same with quite a small difference due to their molecular weight.

However, as shown in Figure 7, 8, and 9, the actual redox couple between Ni^{2+} and Ni^{4+} is lower than that of Co^{3+} to Co^{4+}. As the Ni composition increased, the redox potential of NCM shifted to a lower value. Consequently, even if they are charged to same cut off charge condition, the extraction number of the Li^{+} ion from the Ni-rich NCM becomes larger and thus provides a larger electrical capacity. Therefore, in the same cut off condition of the batteries, an increase in the Ni composition method is selected for a higher energy density material.

Another method used to increase the capacity is an increase in the operating voltage along with an increase in the cut off limit voltage of charging. As shown in Figure 11, with well synthesized NCM111, there is no increase in the irreversible capacity ranging from 4.3 to 4.5 V cut off charging limits. Namely, the reversible capacity and the reversibility increased in this voltage range; however, it is not suitable for the 4.6 V range because the irreversible capacity increases suddenly, and the discontinuous inflection point at the middle of the discharging curve indicating the phase transition also appears. As discussed in Chapter 3, 4.5 V is a boundary voltage from which an abnormal electrochemical reaction has been observed. The present highest limit of the voltage window for the conventional lithium ion battery seems to be 4.5 V.

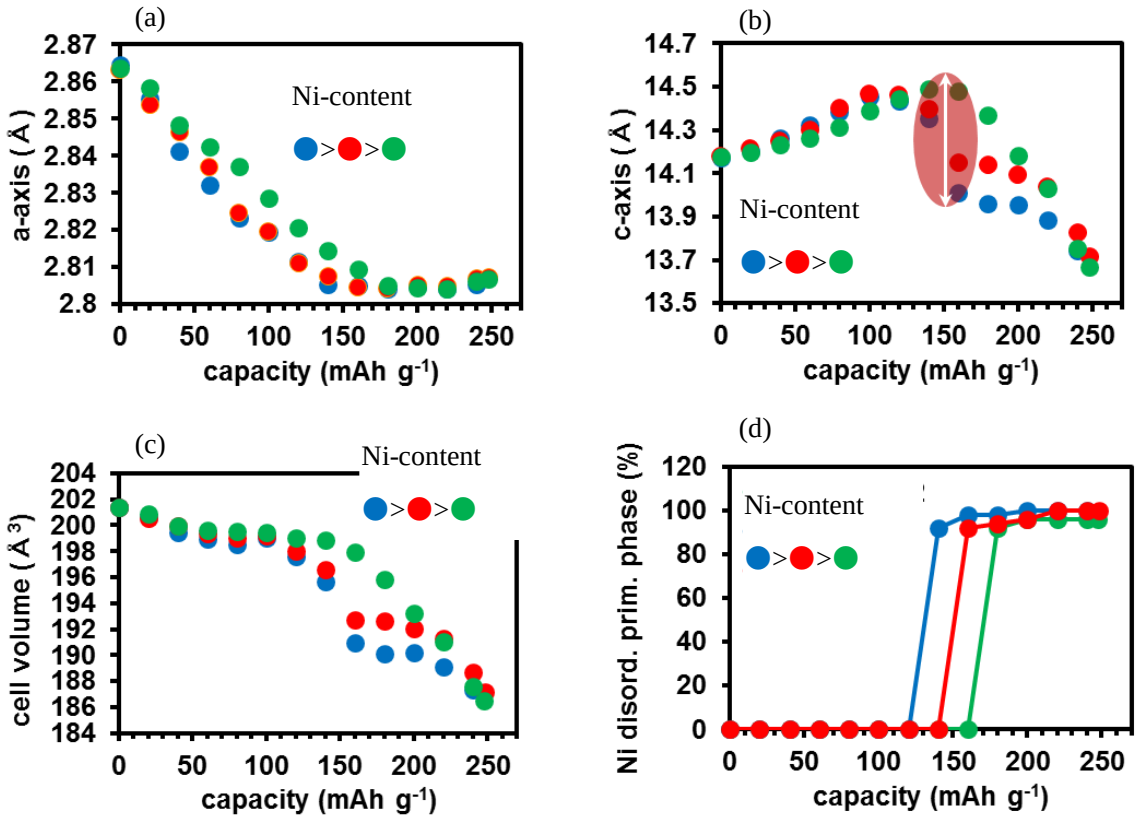

Figure 12 Changing of lattice constant a (a), c (b), unit cell volume (c), and site occupancy of Ni-ion in 3a (d).

The structural instability caused from the Ni increase in the NCM framework is

illustrated in Figure 10. The potential profiles of NCM622 with a cut off charging voltage of 4.5 and 4.6 V are slightly lower in the continuous trend of the cut off voltage increase of 4.3 and 4.4 V. In contrast, both NCM111 and NCM523 show stable responses for the voltage limits. The R-3m structure has a tendency for the Ni ion's migration from the 3b to the 3a Li^+ site (cation mixing) [47], and Figure 10 shows the influence of the phenomena.

Next, the measurement was performed to analyze the structural change as functions of the Ni concentration and the state of charge. To enhance the Ni influence, relatively high Ni compositions of NCA were used as samples. Figure 12 shows the in-situ XRD analysis results. As the charge progressed, the a-axis decreased, and the c-axis increased. Consequently, the volume of the unit cell monotonically decreased. It could be said that the unit cell of the R-3m changed its shape anisotropically. The influence of this crystal shape change is discussed after. Because it has a quite close relationship with battery life. Once the c-axis reaches the maximum point of charging, it decreases sharply. The Rietveld refinement revealed that the Ni occupancy in the 3a Li site also shows an abrupt increase as the c-axis decreases.

2.1.3. Experiments

Synthesis of NCM, NCA

First, $(Ni,Co,Mn)(OH)_2$ and $(Ni,Co,Al)(OH)_2$, as raw materials of NCA and NCM, were synthesized through hydrothermal crystallization. The Ni/Co/Mn and Ni/Co/Al compositions were adjusted in this process. The obtained complex hydroxide was thoroughly mixed with Li_2CO_3 or LiOH in appropriate ratios and then calcined by appropriate conditions, such as the heat pattern, temperature, and oxygen pressure..

Synthesis of LCO

First, CoO(OH), a raw material of LCO, was synthesized through hydrothermal crystallization. Then, the obtained oxyhydroxide was thoroughly mixed with Li_2CO_3 in an appropriate ratio and then calcined by appropriate conditions, such as the heat pattern, temperature, in the air.

Characterization

The X-ray diffraction (XRD) patterns were measured with an X-ray diffractometer Smart-Lab (RIGAKU Corp.,). The condition was 40kV, 200mA for the Cu Kα radiation. The scanning range was 2θ/ω= 10-90° with a scanning speed and step of 1° /min. and 0.02°, respectively.

The phase changes of the NCA samples during the charge-discharge test were examined by in-situ XRD measurements using an in-situ XRD lithium battery cell (Rigaku Corp.; in-situ attachment) and Smart-Lab diffractometer (Rigaku Corp.). The XRD patterns were recorded using Cu Kα radiation (45 kV, 200 mA), 2θ diffraction angles ranging from 10° to 90° with a 0.02° step width, and a fixed time of each step of 1.0 s. The cell charging was stopped during the XRD measurement at a predetermined state of charge

The observation for the cross section of the cathode active materials was carried out with a cross section polisher SM-09010 (JEOL) with an Ar ion beam of 5.5 KV, 120 mA for 5hours. The partial pressure of the Ar was 2×10^{-2} Pa. The cross section was observed with a Scanning Electron Microscope (SEM) JSM-7100F (JEOL).

TEM-EELS, TEM-EDS, and NanoSIMS were employed for the analysis of the fine structure of the ex-situ cross section. First, the sample was sliced by a Focused Ion Beam (FIB) JEM-9320FIB (JEOL) with Ga ion beam at 20kV, 20nA conditions and then ion milled with Ar to decrease the fluctuation of the cross section plane. The Nano Secondary Ion Mass Spectroscopy (NanoSIMS) machine (NanoSIMS50L) was made by Cameca, and a predetermined area was etched with a Cs^+ ion beam with a spatial accuracy of approximately 50 nm square in its maximum precision potential.

The electrochemical properties were measured using a 2032-type coin cell in which the working electrode was composed of each conductive agent and a binder in a 1:1 weight ratio on an aluminum current collector (carbon electrode), and the counter electrode was Li metal. The cut-off voltages for the cyclic voltammetry were 3.0 and 5.0 V with a scan rate of 0.17 mV s-1 at 60 °C. The galvanostatic charge-discharge tests were also performed for the cathode active materials described.

The coin cells were composed of a 1M-$LiPF_6$/(EC+DMC) (1:1 in volume) electrolyte. Each cathode active material was thoroughly mixed with a conductive agent and PVDF (from KUREHA; L#1120) in the appropriate ratio of active materials/conductive agent/PVDF in 94/3/3 or 90/6/4. The electrodes were compressed until the electrode density reached 3.0 g/cm^3, followed by vacuum drying at 100 °C

overnight. The separator used in the present study was a polypropylene sheet (from Celgard LLC; #2400), which is stable against high-voltage usage. All cell constructions were done in an Ar filled globe box at a dew point of under -80 °C.

The galvanostatic charge discharge test conditions were cut-off voltages of 3.0 for the lower limit and 4.3, 4.4, 4.5, 4.6 V for the charging limit.

The cycle life test was accelerated to store the cells in a 60°C oven during the test. After the cycle test, the cells were placed back in the globe box and then dissembled carefully to prevent an electrical short. The obtained electrodes were rinsed with a fresh De-Methyl Carbonate (DMC) with vacuum immerging and then vacuum dried at a temperature of 40 °C.

2.1.4. Results

2.1.4.1. Grain boundary cracking in the polycrystalline particles.

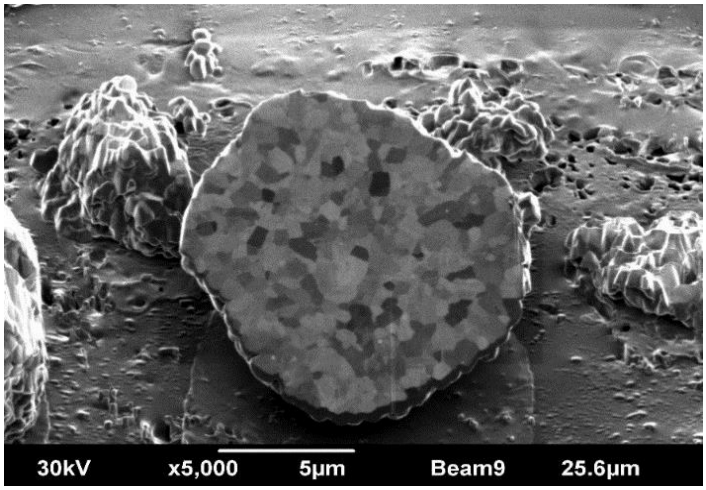

Figure 13 FIB-SIM Image of polycrystalline LCO.

The biggest contribution to the increase in the amount of the reversible Li^+ ions from the crystal framework in these days is appeared to be the particle design for the active materials. For instance, for a large mono crystal like LCO, there is a problem concerning to the Li^+ diffusion kinetics in which the Li^+ diffusion of the particle center

cannot respond to the applied voltage.

On the other hand, in the case of fine particle active materials, that problem is solved because both effect of Li^+ diffusion path shortening and increase in specific surface area; however, there are still some differences in the Raman shift for both samples. Figure 18 also shows the homogeneous electrochemical reaction because there is no Co_3O_4

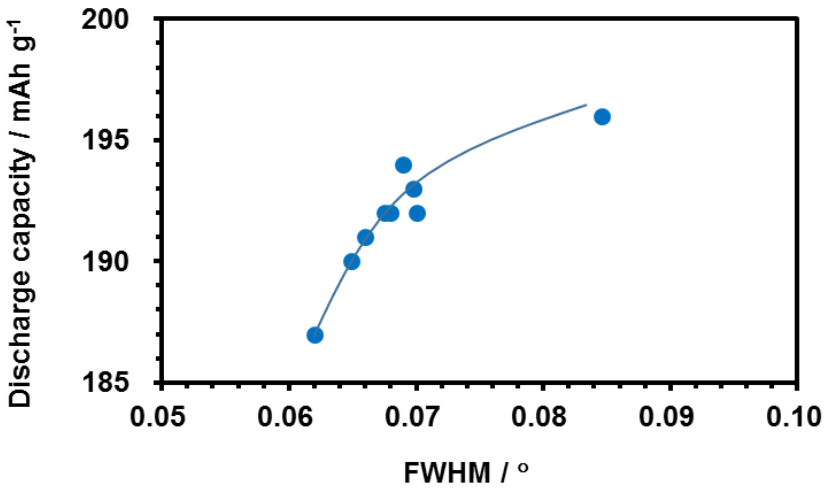

Figure 14 Relation between FWHM (110) XRD peak vs. specific capacity in polycrystalline $LiCoO_{2..}$

signal. Figure 13 and Figure **14** show the supporting data for the particle refinement. Figure 14 shows the discharge capacity of polycrystalline LCO with a constant cut off charging voltage of 4.5 V as a function of the FWHM of the LCO (110) diffraction peak. As the FWHM increased, the reversible capacity increased. It has been shown that if the smaller crystal should cause a homogenious Li^+ extraction from the crystallites with a small amount of structural destraction, then the reversible capacity has been increased.

Another important thing to consider is the risk for the decrease in the actual electrode density. If the focus is only on the particle design as an isolated small particle, then only the amount of the total surface area of the active material increases. This results in the increase of either a PVDF binder or a conductive agent particle. Thus, the active material concentration in the electrode decreases. One efficient solution to this problem is the particle design of the polycrystalline secondary particles, as shown in Figure 13. Most of the active materials for the electrodes have a similar design with a 50 to 300 nm

size of primary crystallites that construct a 5 to 20 mm secondary particle as a motion unit. The large secondary particle unit produces benefits, such as an easy dispersion in the kneading process to prepare the electrode paint and the prevention of the transition metal ion's dissolution into the electrolyte, which is a serious problem in the capacity deterioration of a graphite anode.

It is important to note that to use these polycrystalline efficiently, recognizing the secondary particles as a combination of the bulk and the interface is required. One of the action of that is a control of the contact interface between the crystallites as to the grain boundary.

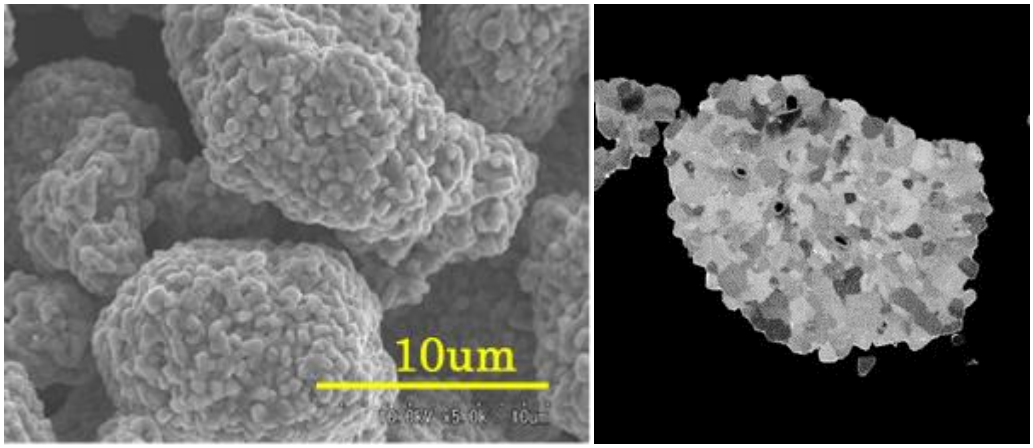

Figure 15 Typical polycrystalline cathode active material (surfece, and cross section).

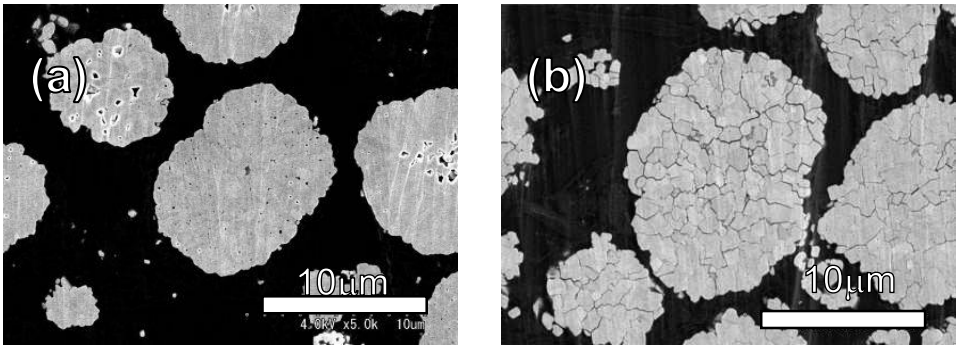

Figure 16 Cross section of polycrystalline cathode active material, before cycle (a), after capacity deterioration by cycling (b).

When observing the cross section of the particles, which were taken out from the

charge discharge cycled battery cell, there was obvious particle cracking along the grain boundary in the capacity faded cathode, as shown in Figure 16. The grain boundary is an important Li^+ ion and electron path, as shown in Figure 17. If this section is fragmented, the isolated crystallites become no more work to the electrochemical reaction. As a result, the entire capacity of the secondary particles will decrease.

In general, the reason for the cracking is considered to be a volume change of each crystallite, as shown in Figure 12. The repeated volume expansion and contraction is generally known [1], [4], and many studies of the particle cracking regarding the strain have been published [49]-[57] ; however, it appears to be almost impossible to search for the electrochemically active materials in the R-3m family. Furthermore, it is not always a disadvantage for the polycrystalline particles to repeatedly expand and contract since it causes the breathing effect of electrolyte to carry the Li^+ ions in the electrolyte for each crystalline in particular for the particle located in the core of the secondary particles.

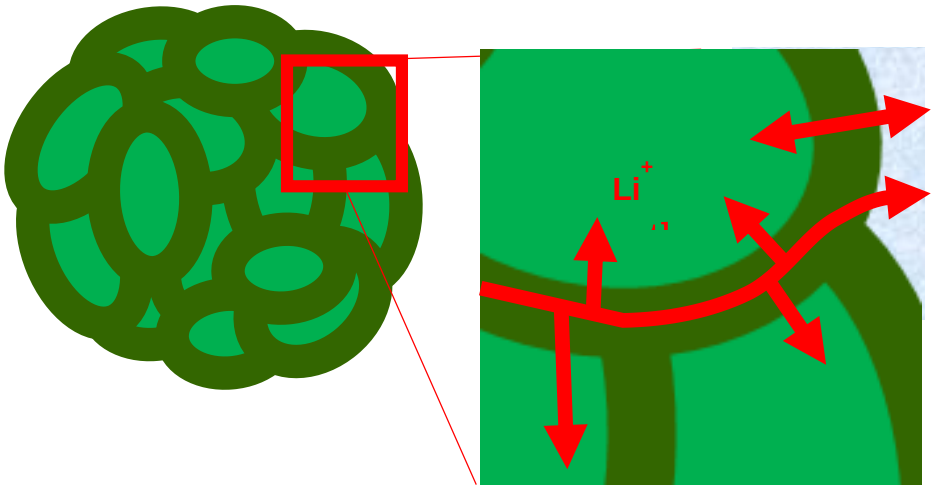

Figure 17 Schematic diagram of Li path in the polycrystalline active particle.

2.1.4.2. Detection of the local destruction area

To consider the relationship that may have been able to combine both the phenomena of the crystal phase transition and the resistive composition, the detection of the crushed site was performed.

The Microscope Raman analysis of Figure 18 indicates that the peak shift to the right direction of the horizontal axis corresponds the amount of Co^{3+} to Co^{4+} oxidation accompanied by the electrochemical Li^+ de-intercalation. There is evidence that the LCO

causes the local destructruring of the inactive Co_3O_4 when the overcharge has taken place because the crystallite size is too large. The overvoltage increases at the particle surface, followed by a phase of destruction by the overshoot Li inter/de-intercalation. Hence, Co_3O_4 was observed locally at the particle surface in the solid/electrolyte interface in the battery. Thus, the battery performance deteriorated. Furthermore, there is information

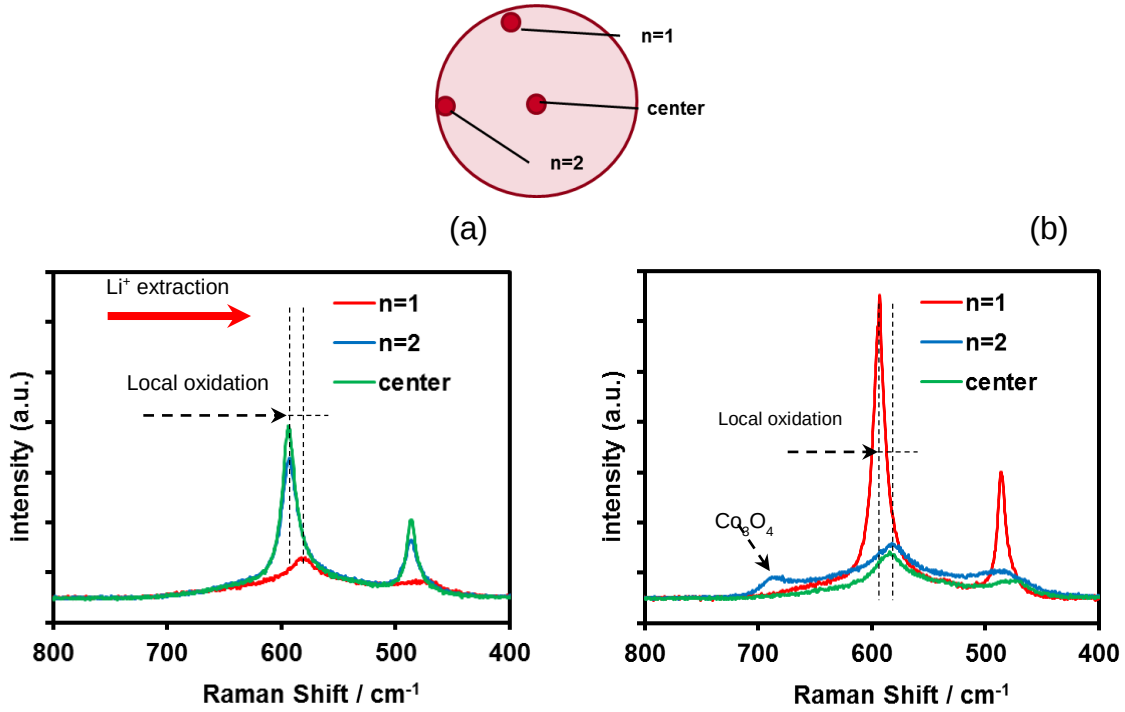

Figure 18 Raman spectroscopy results, to observe the homoginiety of Li^+ intercalation reaction that depends on the crystallite size. Poly crystalline LCO (a) and Large crystallite LCO (b).

about this measurement regarding the existence of the localization of the oxidation state, even if it is in polycrystalline LCO. Although the polycrystalline LCO does not show the over voltage impurities, it is considered to need additional improvements.

The analysis to observe the local transition was carried out for Ni-rich NCA.

The HAADF-ABF TEM analysis results are shown in Figure 19. The samples were charged and discharged repeatedly and then analyzed with ex-situ at a predetermined cycle similar to a previous study [50].

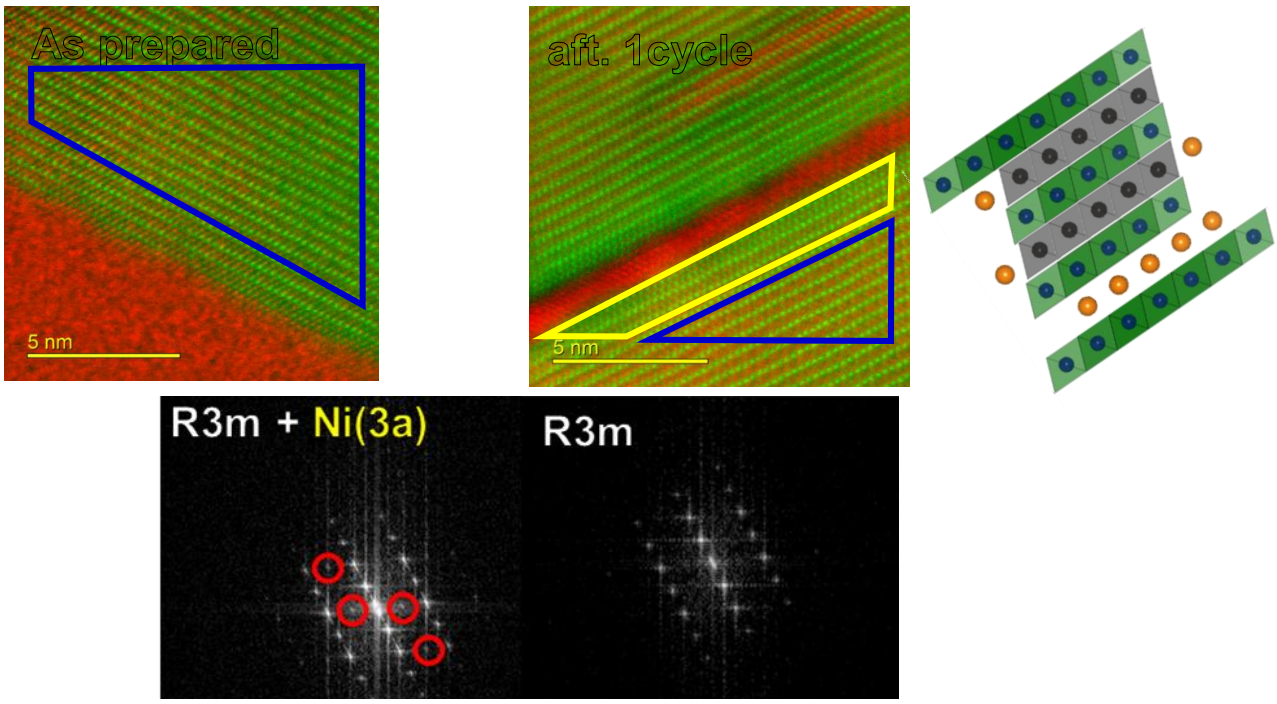

Figure 19 ABF-HAADF composite image of before and after 1st charge discharged Ni-rich NCA, green and red colors are HAADF and ABF image, respectively. FFT image are also showed.

These ABF-HAADF composite TEM images were observed along the (110) projection that is perpendicular to the (003) face. Although it appeared that the transition metal ions were in an ordered array, some disordering occurred after two charge and discharge cycles, and the disordering seemed to be take place in the interface. The FFT spot of this local disordered area indicates the special spot, as marked with a red circle. These results also reveal the structural destruction that takes place at the surface of the crystal, namely, the solid electrolyte interface.

The same analysis for the 100 cycled sample is shown in Figure 20. The structural destruction proceeds to the next step, and the disordered phase in Figure 19 is the transition to the rock salt NiO. The NiO is no longer the insulator for the battery reaction. As previous studies described [58]-[60], this is undesirable formulation. It is serious consequence because the location of the insulator has a stronger impact than that located in the core of the particle since it could be recognized as a insulate barrior for the Li^+ diffusion.

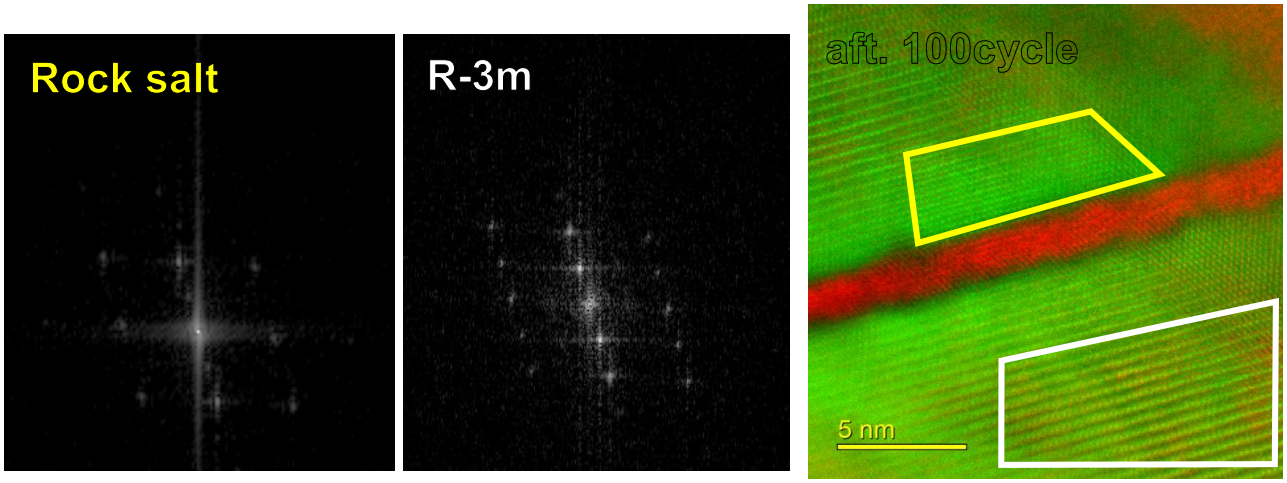

Figure 20 ABF-HAADF composite image of after 100th charge discharged Ni-rich NCA, green and red colors are HAADF and ABF image, respectively. FFT image of yellowed rectangular region for rock salt and white rectangular part for R-3m.

$$[Li]_{3a}[Ni]_{3b}O_2 \Leftrightarrow [Li_{1-x}Ni_x]_{3a}[Ni]_{3b}O_2 \Rightarrow NiO$$

For the NCM shown in Figure 10 and Figure **11**, no HAADF or in-situ XRD data was observed, but it could easily be assumed that the same phenomena occurred, particularly the constant irreversible capacity ranging from the cut off voltage of 4.3 to 4.5 V, indicating the constant generation of the resistive local domain at the interface. Cation mixing and the rock salt NiO have a more resistive impact than its fraction.

Based on the results, the key factor that could enable the increase in the stability of the crystal structure is in the interface. In this thesis, both the lattice expansion and the contraction are permissible. Thus, the focus is on the interfacial reaction that could cause a homogeneous reaction to obtain the stable material that has no crack after charge discharge cycling. One potential solution to solve the problem is implied in Figure 21. The cracking is accompanied by a resistivity increase.

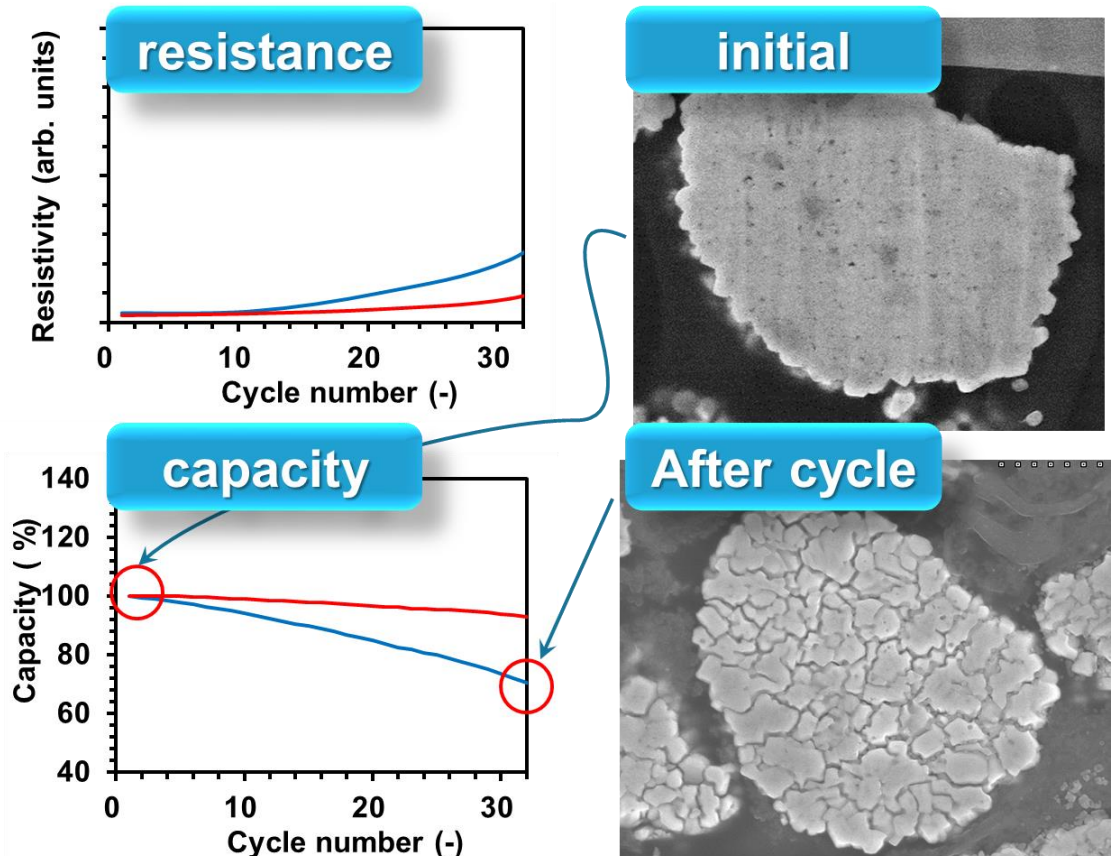

Figure 21 Typical resut that shows capacity fading and resitance growth by Grain boundary cracking.

One of the most useful examples described in this thesis is the grain boundary composition that could suppress the grain boundary cracks and cause a longer life cycle, even if their samples have the same bulk composition. Consequently, they have the same lattice expansion and contraction nature, but the composition in the grain boundary could improve the weak points.

2.1.4.3. Suppression of the resistive components

As mentioned, the structural destruction and the consequent resistive phase generation proceed the over voltage in the battery system [39]. As a result, a higher voltage gradient than the nominal could be generated in which a side reaction between the electrolyte and the electrode is further enhanced [58]-[60]. This is not only a problem for the inorganic phase on the surface but also for the component that is composed of an organic-inorganic complex, such as a resistive film.

The influence of overvoltage on the electrode surface is not ignorable since the impact is not insignificant. Although the analysis for this resistive film focused on the anode SEI before [17]-[33], cathode-related studies in this field are increasing as recent analysis techniques develop [34]-[39].

Furthermore, in the synthesis process for NCM or NCA, it is a conventional technique, such as over stoichiometry Li source addition to prevent the cation mixing in the NCM and NCA, that results in the impedance growth because the Ni ions that migrated to the Li^+ layer hinder the Li^+ diffusion [61]; however, an excessive Li addition becomes reaction inhabitant components if the composition is not correct. In particular, the residual Li components left behind the grain boundary cause a resistivity increase.

The excess Li components are clearly precipitated on the surface of the sintered particles, so it appears to become the origin of the over voltage. This over voltage generation either on the surface or in the grain boundary seems to help promote the generation of resistive layers.

Likewise, Ni migration into the Li site (cation mixing) also seems to influence the side reaction similarly to the excess lithium components. Therefore, it must be quite important, and the basic requirements, such as an appropriate synthesis condition consisting of a mixed ratio of raw materials, mixing methods, heating ratios, calcination temperatures, complex patterns, cooling rates, post annealing, and partial oxygen pressures, are necessary to obtain the full performance of the material's innate ability.

An example of this is shown in Figure 22. They have the same composition, so they have the same lattice expansion and contraction property; however, it could be improved by an interfacial treatment, which is caring for the composition in the grain boundary. The STEM-HAADF of the as-prepared NCM cross section will be discussed. Figure 23 shows a poor cycle performance sample, and Figure 24 shows the sample with improved cycle life. It is important to note that the post annealing for the sample shown in Figure 23 could be improved in its cyclability without a bulk composition. Figure 25 shows the ELNES results of this sample. With the measuring point moving from the center of a crystallite to the surface, the O-K edge signal causes the NiO existence at the surface point. The Ni-L edge is consistent with the implication since it shows the Ni ion's

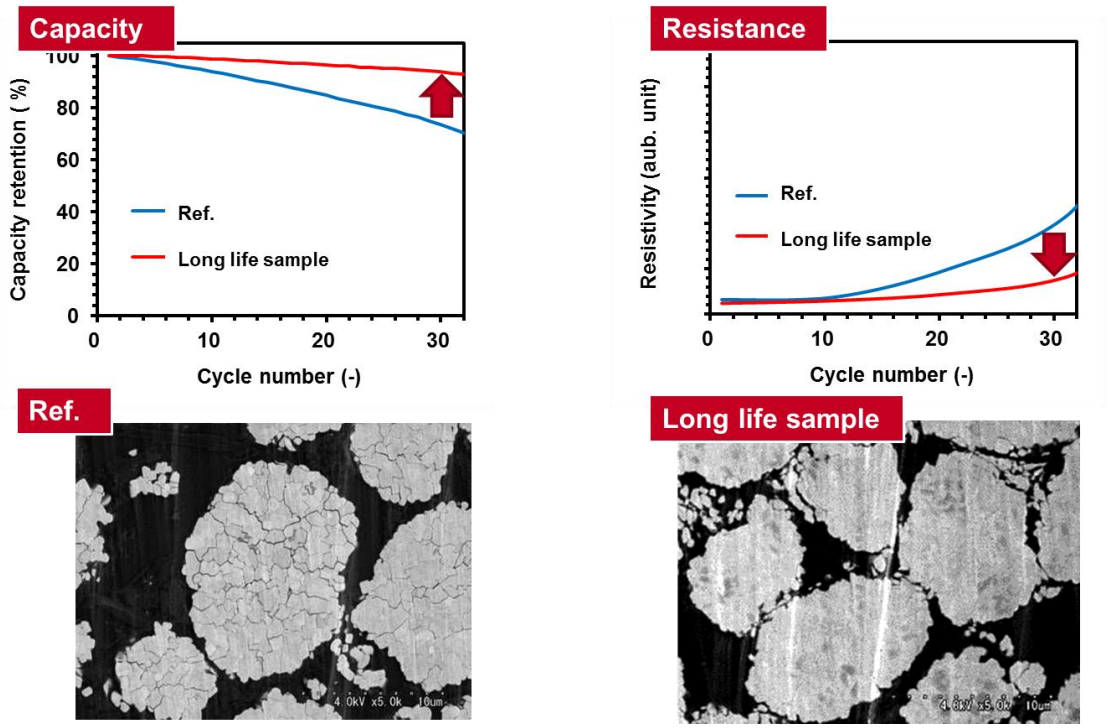

Figure 22 An example for long cycle life and short cycle NCM, having a same composition.

slight reduction at the near surface of the crystallite.

On the other hand, in the long life sample shown in Figure 26, neither a peak shift of the O-K edge nor an Ni-L edge were observed. Hence, this indicates that the post annealing made the localized NiO on the crystallite surface revert to the original R-3m NCM with an oxidation effect. Since each surface of the crystallite was recovered with its structure through the annealing treatment, it appears that the cycle performance closed to the NCM nature performance. For these reactions to occur, the existence of the counterpart component lithium is absolutely essential. The results of the evaluation of the Li existing place is described next.

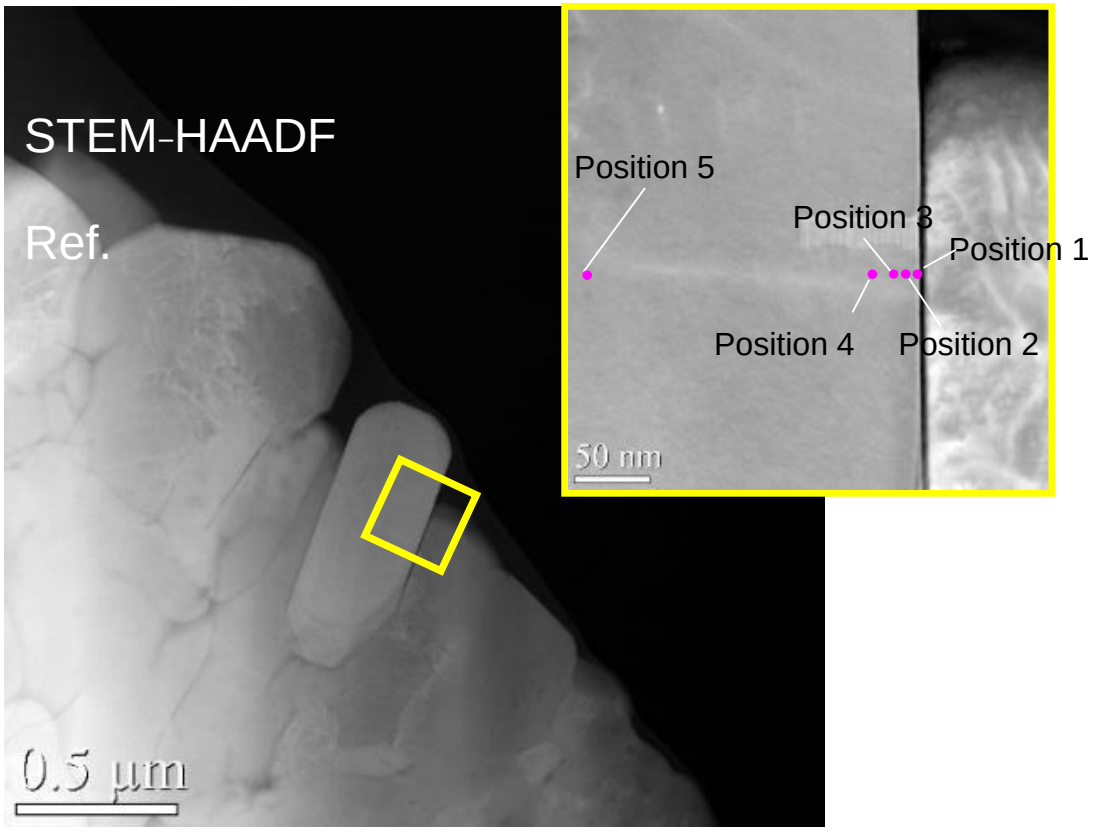

Figure 23 HAADF image for ref. NCM particle.

Figure 24 HAADF image for Improved NCM particle.

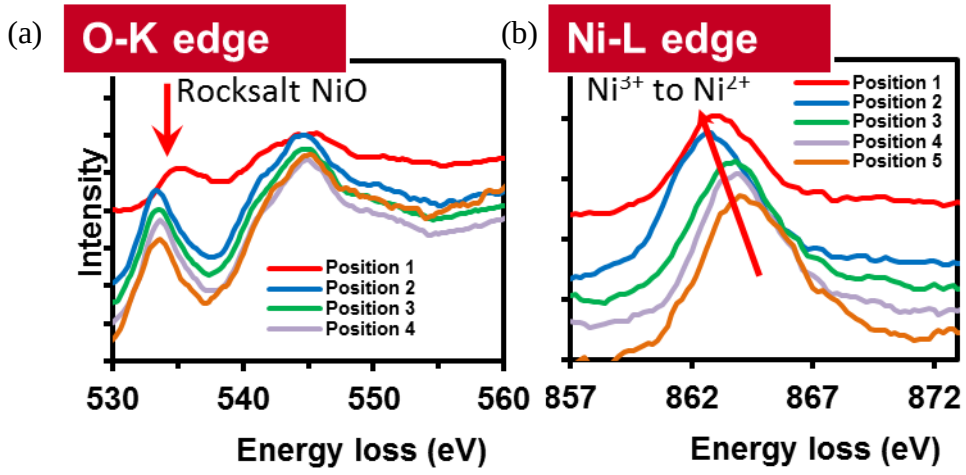

Figure 25 EELS of O-K edge (a), and Ni-L edge (b) for reference NCM cross section. Each position are denoted in Figure 23.

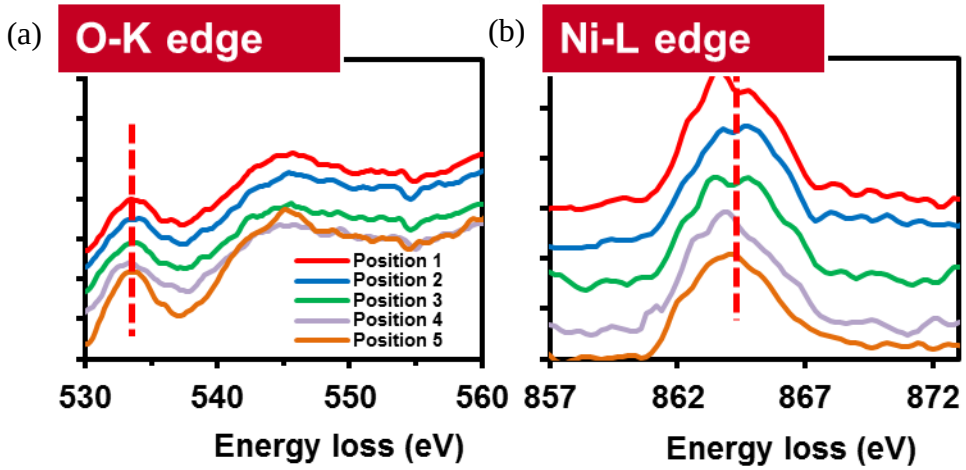

Figure 26 EELS of O-K edge, and Ni-L edge for post-annealed NCM cross section.Each position are denoted in Figure 24.

To investigate the excess lithium component's influence on the charge discharge cycle life and its existing place, the Li/Ni stoichiometry in the particle in a nano meter order of accuracy with three dimensions signals was studied. NanoSIMS was employed for the analysis. With EELS, it is hardly to accomplish it because EELS signal of lithium and nickel ion are much closed so it could hardly distinguish the Li from Ni. On the other

hand, NanoSIMS could distinguish it, because it has a high precision that could detect the isotope, so it could distinguish between not only Li and Ni but other additive elements [62]-[65]. Figure 28 shows the analysis results for the marked area shown in Figure 27. To confirm the accuracy of the analysis, signals were taken by 3 dimensions by Cs^+ etching, as shown in the area in Figure 27. The signals indicated important insight in that the poor cycle life particles show a higher Li concentration in the grain boundary.

Each minimum point of the Ni signal was consistent with the grain boundary for any line, as shown in Figure 27 by yellow lines. The Li/Ni composition at the grain boundaries is quite different from that of the crystallites. The minimum points of Ni intensity indicate the grain boundary. The Li/Ni concentration tends to be higher at the grain boundaries, and the shape of the intensity as a function of the scanning length showed the opposite intensity to that of Ni. These trends are same in any direction in this 3-dimensional scanning. A higher deviation of the Li/Ni concentration increased the particle cracking after battery cycling.

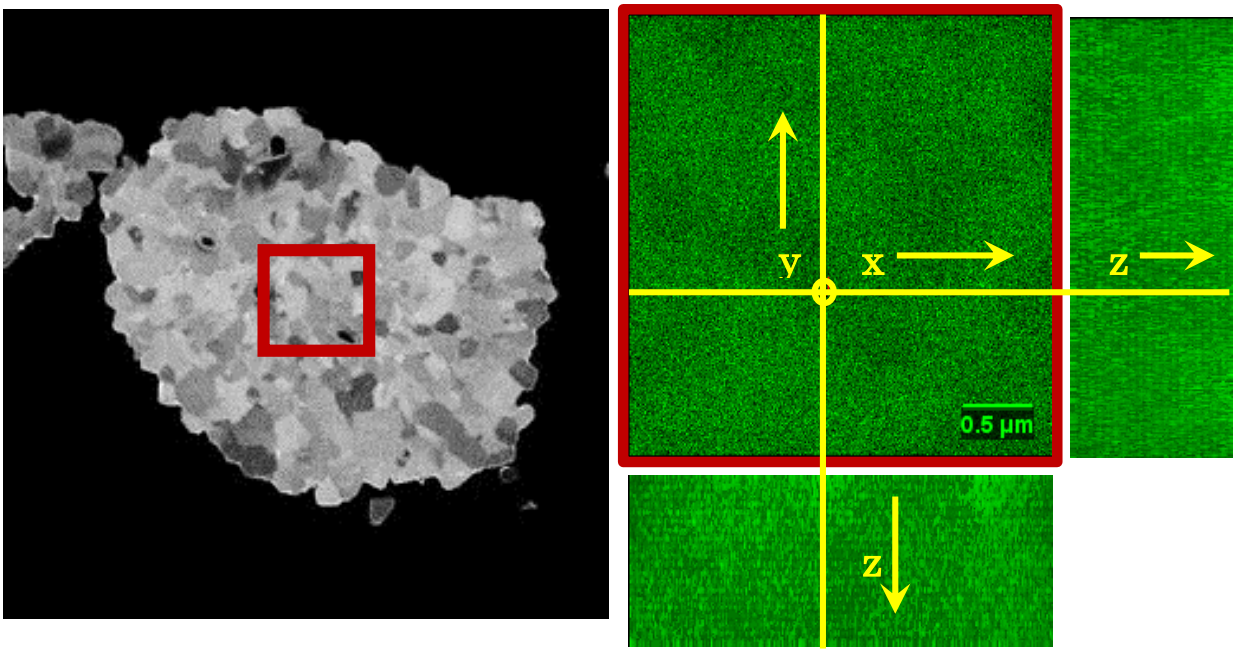

Figure 27 FIB-SIM image of as-prepared NCM crosscecton, and NanoSIMS eching area to observe the 3D element distribution (a), Net of Ni mapping obtained by 3D eching.

A comparison analysis of the samples shown in Figure 23 and Figure 24 was conducted, as shown in Figure 29 and,Figure 30. It is obvious that the tendency of

opposite Li/Ni intensity to that of Ni symmetry of the annealed NCM shown in Figure 29 (b) is weakened. This indicates that the Li concentration has been restricted by post annealing. These results are quite consistent with the EELS analysis; thus, it could be said that these analyses are quite reliable.

The results described clearly illustrate the importance of the suppression of the excess Li concentration that results in the homogeneous structure near the grain boundary. The reason that the particle in which the grain boundary Li is concentrated has a tendency of cracking during the charge discharge cycles will now be explained.

Figure 32 shows ex-situ cross section NanoSIMS mapping for the sample cross section after battery cycling. The high concentration of the Li-F and the Li-C coexisting after cycling, shown in (b) and (d), respectively, implies that high-resistivity byproducts reported in several studies [34]-[39] existed in the generated cracks. Figure 31 also supports the C and F existence in the crack.

Discharging curves in Figure 35 are reflected the resistance growth in the grain boundary shown in Figure 22, of which profile shape became linearly as the resistance increased.

Table 3 lists the theoretical density per Li estimated based on their true densities for a potential resistive composition. With the assumption based on the NCM's synthesis route, the lithium in the grain boundary is Li_2O. If they react with electrolytes along with the electrochemical reaction to the listed compounds, their volume could be at most approximately eighth the original Li_2O. This volume change must be remarkable with a higher Li concentration in the grain boundary that results in the grain boundary exfoliation so to call particle crack occurrence.

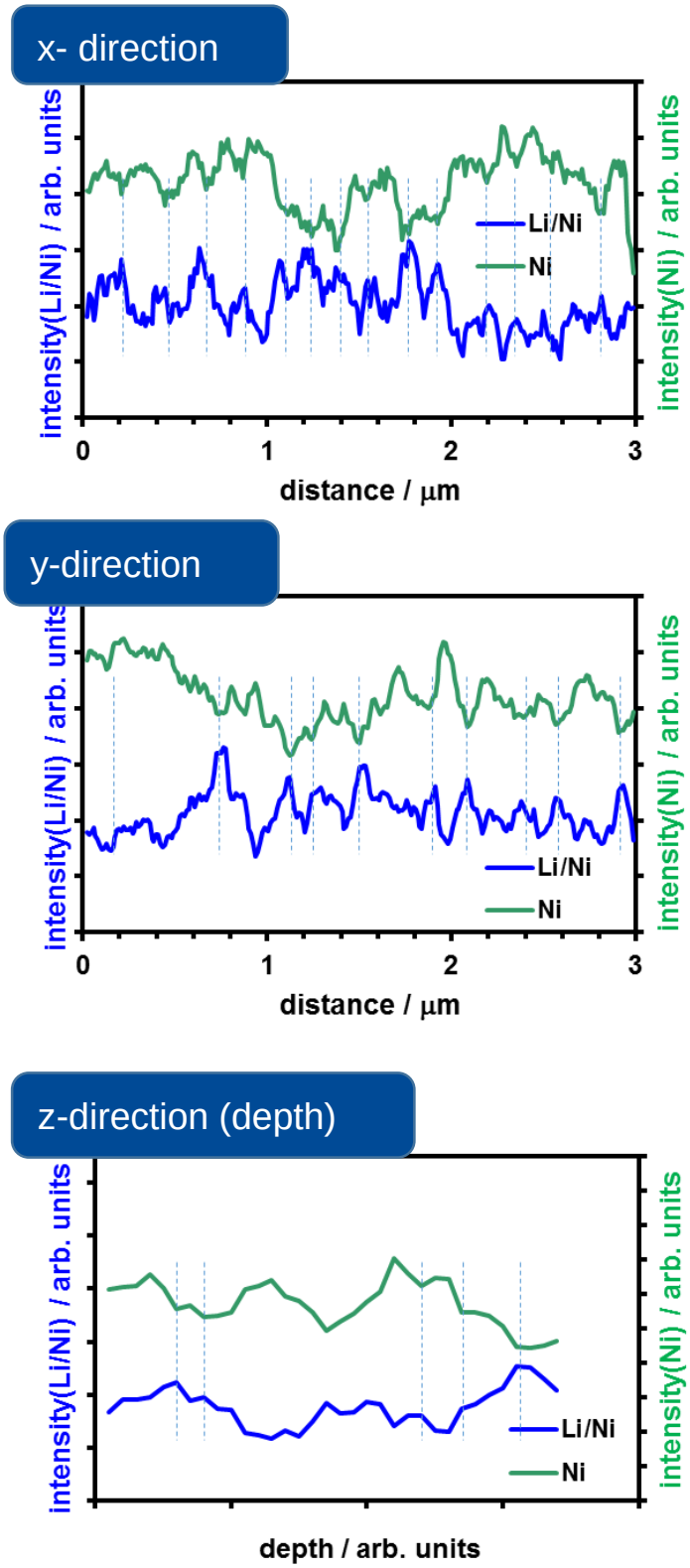

Figure 28 Line analysis of Ni, and Li/Ni in x, y, and z direction indicated in Figure 27.

Table 3 Theoretical density of some possible resistive films.

	true dens. g/cm^3	mol/cm^3	volume per-Li (-)	Volume change
Li_2O	2.01	0.067	1.00	-ref.
Li_2CO_3	2.11	0.06	1.1	expand
LiOH	1.46	0.03	4.6	
LiF	2.64	0.11	1.3	
Li$_2$EDC	1.64	0.01	7.7	
LiMC	1.36	0.02	8.1	

Li_2EDC: dilithium ethylene dicarbonate, LiMC: lithium methyl carbonate.

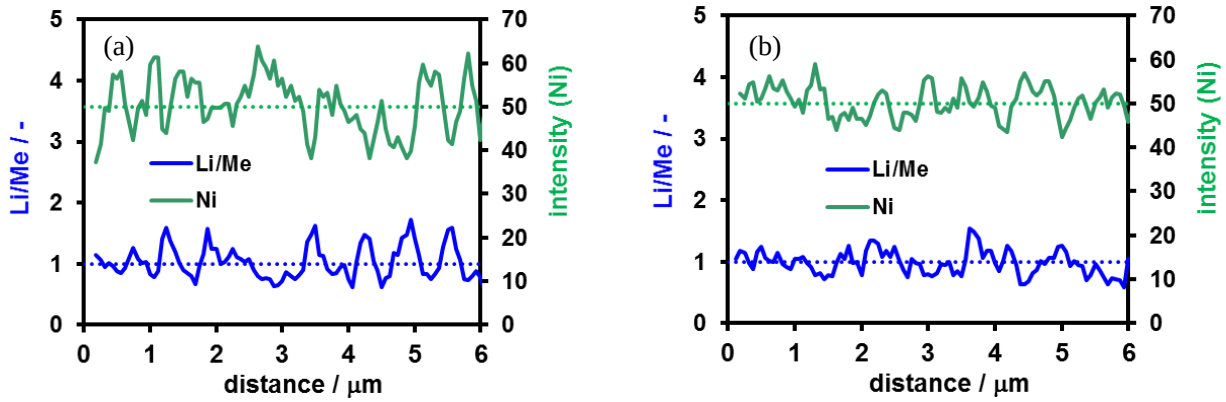

Figure 29 NanoSIMS analysis result for Ref. sample (a), and Annealed sample (b) before the cycle.

Figure 34 shows the proposed cracking model based on this study. As the charging proceeded, the lattice constant of the a-axis decreased, and then it made a slight space that could introduce the electrolyte into the clearance. If the sample contain the resistive domain of NiO and Li_2O in the grain boundary as shown in Figure 34 (a), the electrochemical Li^+ intercalation will be obstructed. Therefore, it is assumed that the side reaction of the solid/electrolyte interfacial reaction in grain boundary could easily be accelerated by a driving force of the electric double layer, then it result in the resistive film generation. From the perspective of a crystal study, this face has a high reactivity, which is called an edge face, and the high reactivity is reported in previous studies [66]. As the cycle proceeded, above resistive film grew thicker and filled the opened space of the boundary, and then it could no longer be closed again even if the a-axis returned to

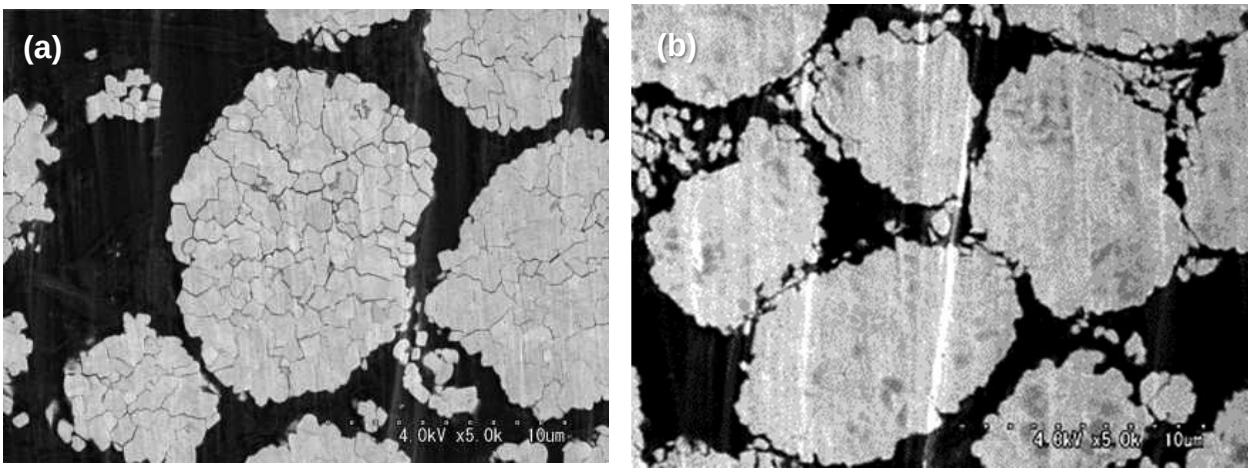

Figure 30 Electrode cross section of Ref. sample (a) and annealed sample (b) after cycle test.

the original value as with discharging. This is the primary cause for cracking due to the high lithium concentration.

Figure 34 (b) shows the cracking model having an improved cycling capacity durability with annealed sample shown in Figure 23 (a). There was less polarization and a lower lithium concentration than that before the annealing, so it generated a less resistive film in its grain boundary; however, as described, this sample also shows the small capacity fade with the charge discharge cycle. Even with this improved sample, the double layer in the grain boundary may have had some concentration of Li^+ ion or its counter anions due to the small electric double layer.

To obtain an improved performance of the cathode active material, an aggressive and efficient method is required. As a result, a material to overcome the market demands could be developed in addition to the standard conditions because only the optimization of the standard synthesis could not break its own constraint and could not produce breakthrough qualities.

One strategy is the introduction of the protective film into the grain boundary used in this study. In particular, it seems to be a desired experiment that could coat each crystallite in the polycrystalline particle. In the end of this section. The Li_2ZrO_3 coating effect will discussed as shown in Figure 34. The material was reported by Thackeray [67], [68], and since then, many effects of the protection properties have been studied [69], [70] . In order to confirm the effect of that coating, the Li_2ZrO_3 was coated especially on NCM's electrically active crystal edge face and then was characterized.

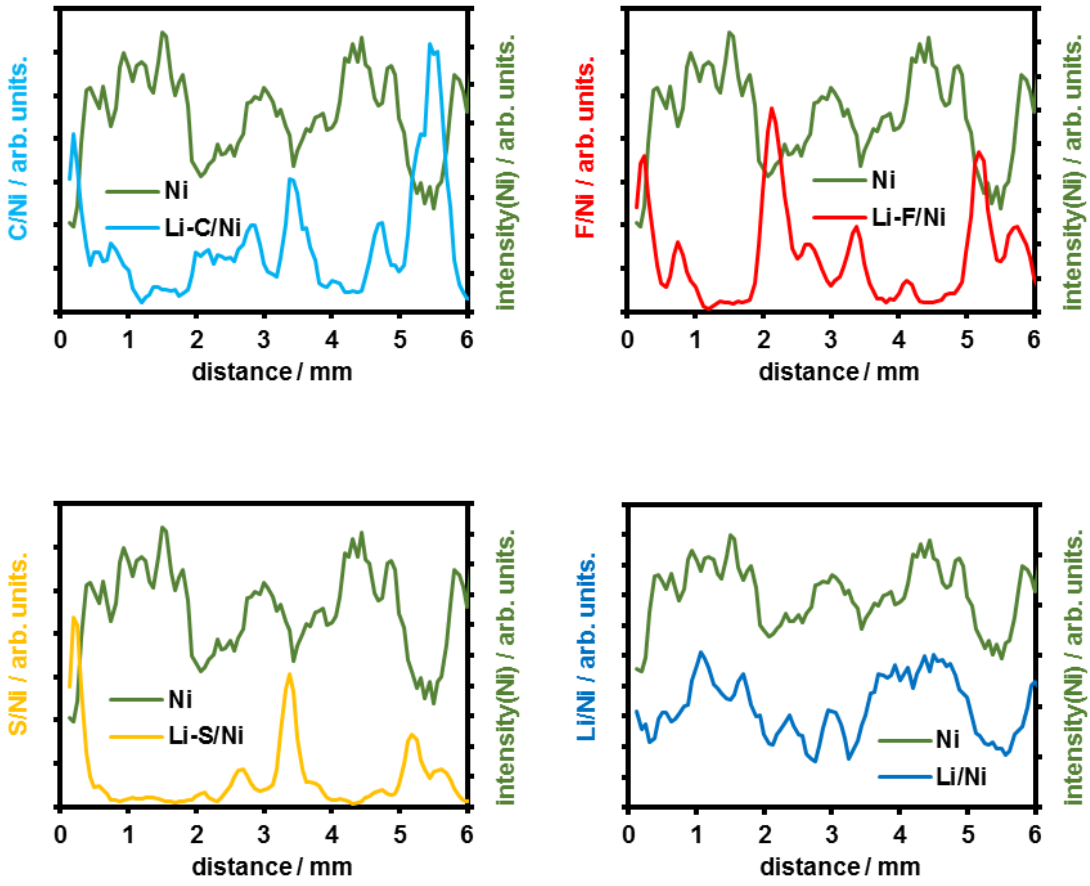

Figure 31 Line analysis for the images shown in Figure 32.

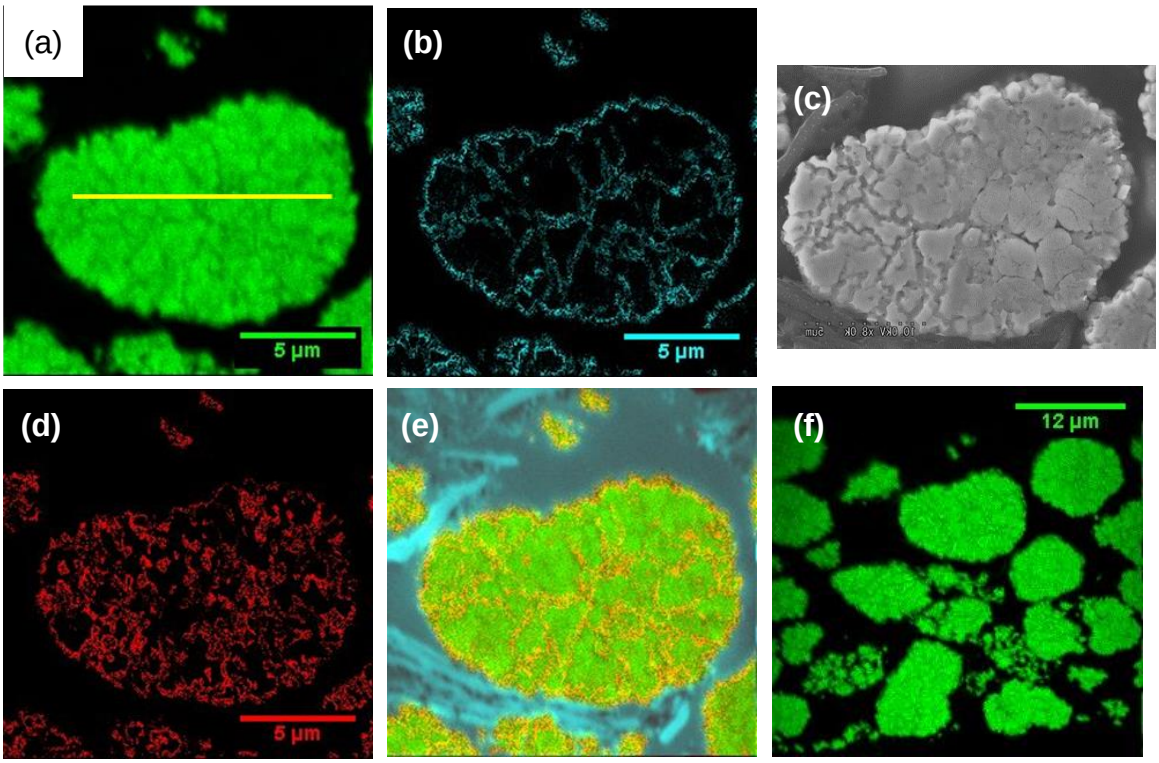

Figure 32 Mapping results obtained with NanoSIMS after cycle fade for the sample before annealing. Ni (a), Li-C coexisting (b), SEM (c), and Li-F coexisting (d), composite image of Ni and cracking (e), respectively.

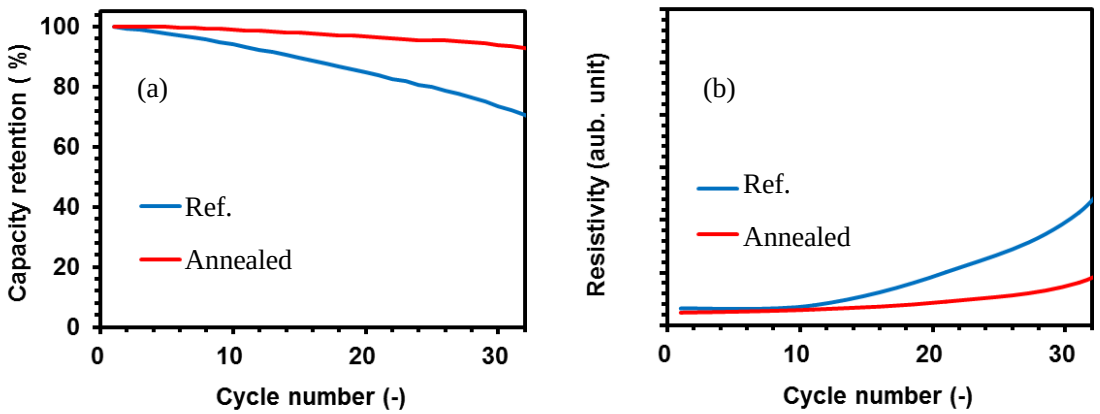

Figure 33 Comparison between before annealing (ref.) and post annealed sample.

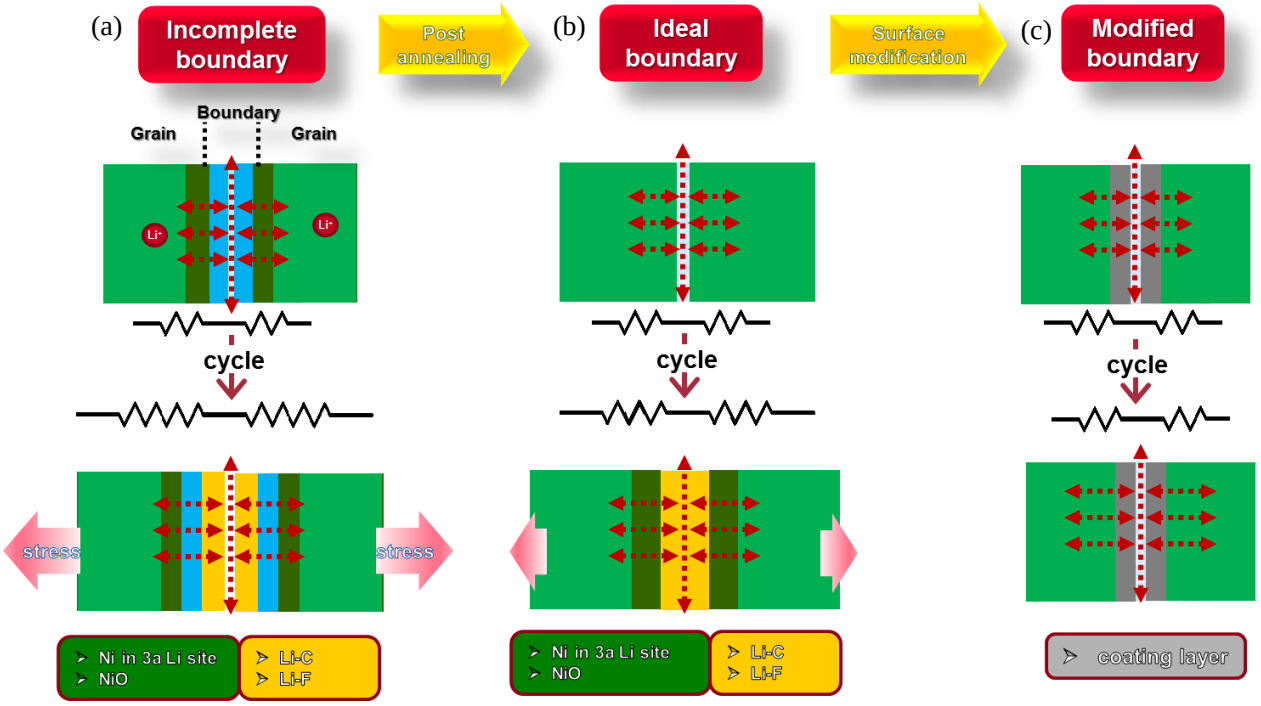

Figure 34 Schematic model of cracking along the grain boundary with growing the resistive film. Incomplete (a), Ideal (b), and Modified (c).

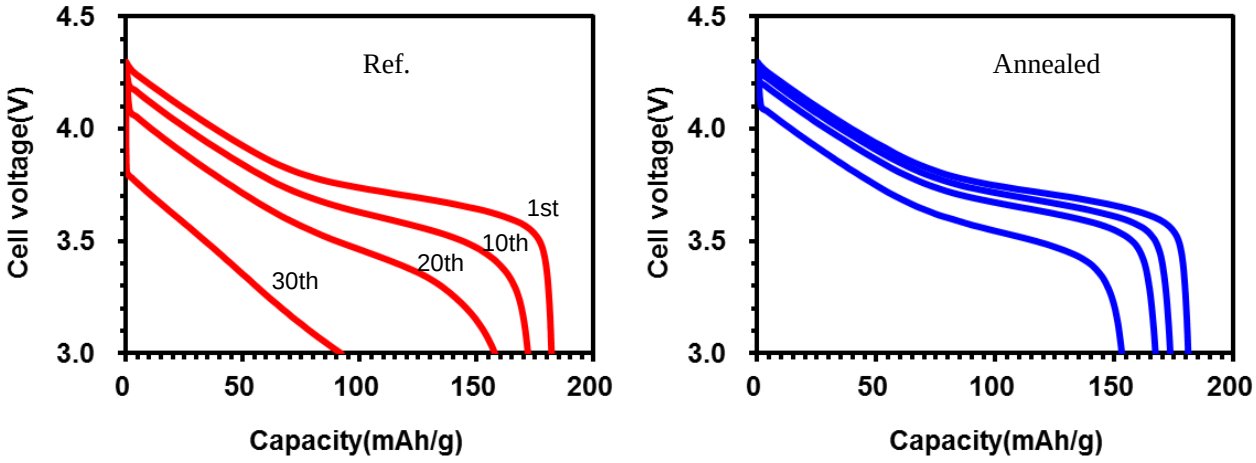

Figure 35 Discharge curves of post annealed sample.

2.2. Epitaxial thin film - analysis and exploration of coating elements -

2.2.1. Experimental

Because polycrystalline particle has complexed properties, such as local composition and geometrical shape, it is difficult to analyze the various reactions that take place inside of it.

Epitaxial-film electrodes offer the opportunity to have a modeling experiment focused on the interface reaction, with its nanometer range having a very thin thickness. Furthermore, the two-dimensional interface restricts its reaction fields, which could enable the selection of an appropriate lattice plane [69]. Hence, it could be expected that the thin film experiments' feedback its theoretical interfacial results to the interfacial reaction of the grain boundary in the practical use particle design. Furthermore, it could exclude the influence of binder and conductive agents. Namely, pure cathode active materials reactions could be evaluated with the film.

Epitaxial film electrodes were employed in this study to determine a guide for the efficient coating of the grain boundary in the polycrystalline particle.

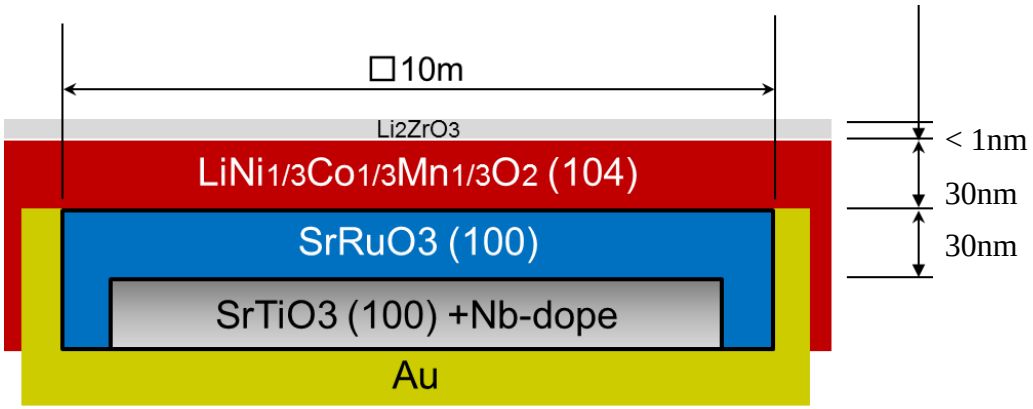

Figure 36 Schematic diagram of PLD electrode's cross section.

2.2.1.1. Film preparation (PLD)

The NCM epitaxial thin oriented in the (104) direction film electrodes were prepared with The Pulse Laser Deposition (PLD) technique. It was carried out with a system consisting of a 248 nm KrF excimer laser (Lambda Physik, COPex102, and CMPex201).

$SrTiO_3$ (STO) (100) wafers (10mm square, 0.5mm thickness) with 0.5wt% doped Nb were used as substrates in this study. Nb doping increases electric conductivity of STO. At first, $SrRuO_3$ (SRO), which has the same crystal texture, was deposited as an enhancement layer for electrical conductivity. Then, gold was deposited to the opposite face of the SRO because it could work as a current collector when assembled in an electrochemical coin cell to investigate its electrode characterization. The PLD conditions for this study are summarized in Table 4.

Table 4 Preparation conditions of PLD synthesis for NCM and coated NCM thin film electrodes.

Target		**SRO**	**NCM**	**LZO**
substrate		STO(100)	SRO(100) /STO(100)	NCM(104) /SRO,STO(100)
Temperature		700	650	500
heating and cooling rate	°C/min.	10	10	10
target distance from substrates	mm	60.6	60.6	60.6
laser energy	mJ	49	126	25
laser frequency	Hz	5	3	5
atmosphere	-	O_2	O_2	O_2
oxygen pressure (on heating)	Pa	15	10	10
oxygen pressure (deposition)	Pa	15	75	10
oxygen pressure (on cooling)	Pa	50	75	10
deposition time	min	20	10	4

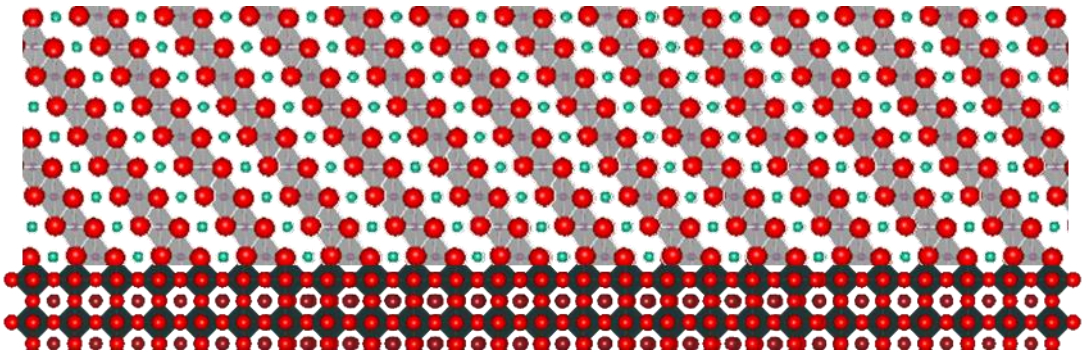

Figure 37 Schematic cross section image of epitaxial membrane, NCM(104) on SRO(100) substrate.

2.2.1.2. XRD characterization

Thicknesses of the thin films were carried out with an X-ray diffractometer (RIGAKU ATX-G), with Cu Kα radiation, of 50kV, 300mA condition. The thickness of the films were analyzed using X-ray reflectivity curves, with a condition of 2 θ/ω, 0.2-4°, scan speed = 0.3°/min, and step width of 0.02°.

The orientation of the films was confirmed both for out-of-plane and in-plane. The condition was 50kV, 300mA for Cu Kα radiation. Scanning range for the out-of-plane was 2θ/ω = 10-100°, with a scanning speed and step of 5°/min. and 0.02°, respectively. The in-plane diffraction pattern was obtained with 2 θκ/π, ranging from 10 to 100°, with a 5°/min. scan speed of 0.02° step.

2.2.1.3. Charge discharge test

Coin cells 2032 were assembled to evaluate the electrochemical properties of the epitaxial thin electrodes. The cells were composed of a thin electrode as a working electrode and 1 ml 1M-$LiPF_6$/(EC+DMC) (1:2 in volume) electrolyte as well as lithium metal as the counter electrode. The separator was a polypropylene sheet (from Celgard LLC; #2400).

The galvanostatic charge discharge test was done within a cut-off range of 3.0 to 4.3 V, with a 0.5 C current density. Cells were stored in a 25°C evacuator during the test. The TOP view objection was observed with a Scanning Electron Microscope (SEM) (JEOL JSM-7100F). Energy Dispersive X-ray Spectroscopy (EDS) was used to obtain color mapping of the desired elements. The operating condition was 5kV, 100mA, and had a 100 count per every part.

2.2.1.4. TEM-EDS, Electron diffraction

Cross-sections after the cycle FIB cross-sections and TEM lamellas were prepared with a JEM-9320 Focused Ion Beam (FIB) (JEOL), with 20 kV and 20 nA Ga beams. The lamellas of the electrode, which were obtained in a predetermined direction, were carried to the Mo stage with a Van der Waals' force generated on the tip of the glass capillary. Then, the JEM-2100 Transmission Electron Microscope and EDS system (TEM) (JEOL) were used for image and composition observation.

2.2.1.5. Results

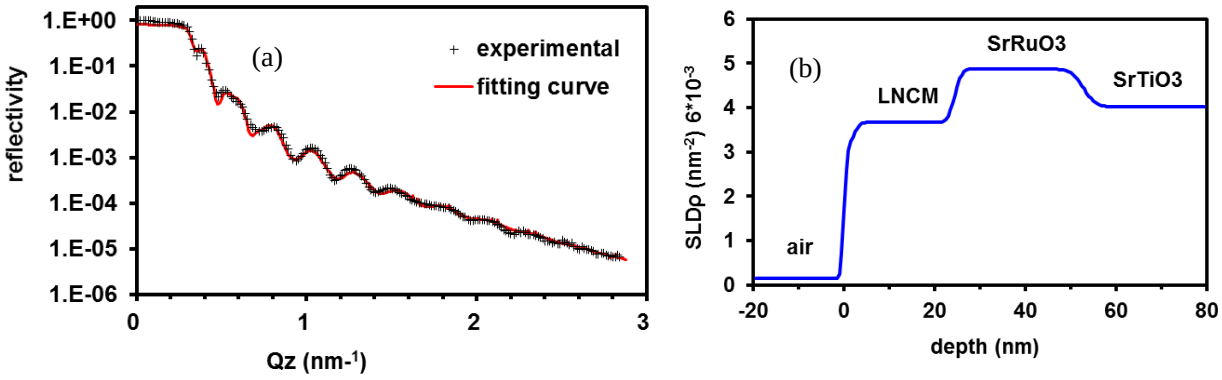

Figure 38 Measurement and fitting Results of the thin film thickness, XRR curve and fitting (a), estimated thickness of each layer by the fitting (b).

Figure 38 shows the observed XRR spectra and the fitted curves for the film. The spectra were plotted as a function of the scattering vector Qz ¼ 4πsinθ/λ, where λ is the wavelength (1.541 Å) and θ is the angle of incidence of the X-rays. The refined parameters for the thickness and density were 32 nm and 4.7 g cm^{-3}, respectively. The fitting process was performed using a value of 5.12 g cm^{-3} for the $SrTiO_3$ substrate density. The best fits were obtained using a three-layer model. Figure 38 shows the thickness of each layer of the fitting result.

Although LZO is reportedly excellent for the protecting film of the particle surface coating, it has much larger resistivity than that of NCM. Therefore, the required LZO coating thickness was estimated at only 0.8 nm. The thickness was determined based on many trial experiences for the product's scale particle performance. It is thought that less

than a 1% weight coating for the particles is best because the very thin coating could hardly be refined with its XRR pattern. Therefore, the PLD parameters of deposition time of were decided and interpolated with the preliminary experiment's data of both the film's thickness and deposition time relation.

Figure 39 shows out-of-plane XRD patterns and in-plane patterns along the (100) substrate direction for the NCM film. The SrRuO3 is identified as having an (h00) orientation-based diffraction peak in the out-of-plane patterns. The existence of NCM (10–4) peak alone in this out-of-plane indicated the successful orientation of this thin film, which was the same as in previous studies. [66] The in-plane patterns were also consistent with the epitaxial growth of the NCM-oriented (104) film. The estimated lattice parameters were 2.85 and 14.175 Å for the a- and c-axes, respectively.

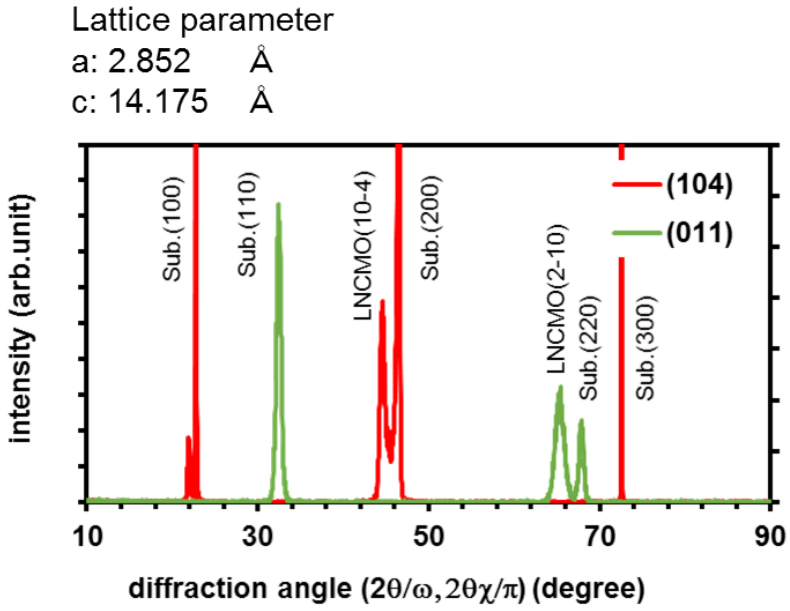

Figure 39 Thin film XRD pattern, in plane (green) and out of plane (red).

SEM-EDS, as shown in Figure 41, indicated the homogeneous coating of all elements on the surface of the $SrTiO_3$ substrates, in which Ni, Co, and Ru were coated, except on the masked area during the deposition. Conversely, the Sr signal intensity was higher in the masked area. The stoichiometry of this thin NCM film was confirmed with ICP measurements as $LiNi_{1/3}Co_{1/3}Mn_{1/3}O_2$.

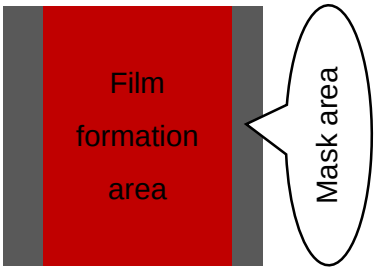

Figure 40 Schematic diagram of 10×10mm epitaxial film.

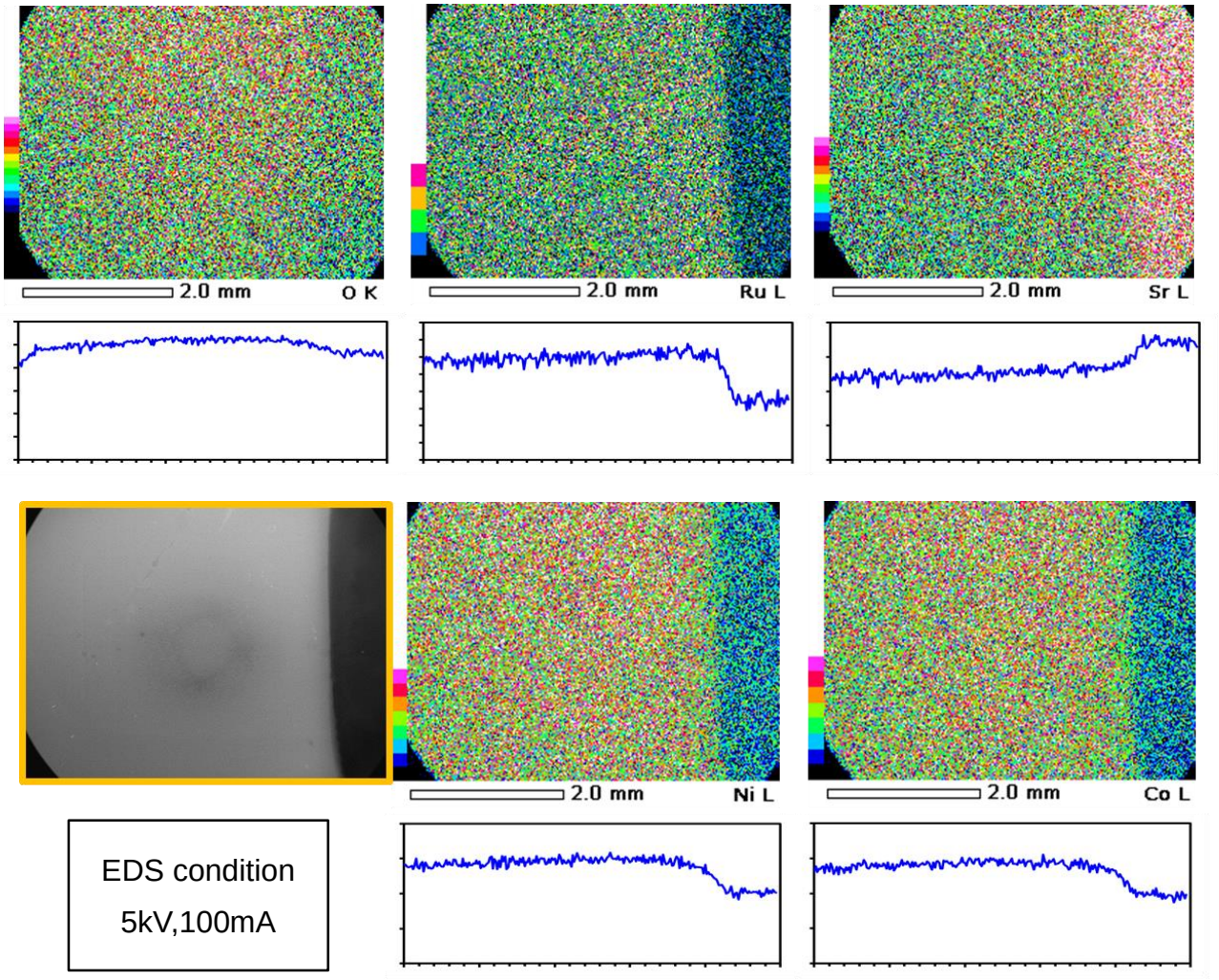

Figure 41 EDS mapping image.

The thin film was evaluated for electrochemical charge discharge cycling. Figure 43 shows the capacity retention (a) and discharge potential profile in every 10th cycle (b). The specific resistances, shown in (c), were estimated using the IR drop at the depth of

discharge (DOD) 0%.

In spite of a rather thin coating of LZO, the electrode showed excellent stability against cycling when compared to that of pristine NCM film. Only the first three cycle capacities were smaller than the pristine electrode, which was due to the higher resistivity of the LZO coating the film. However, the resistivity became negligible as the cycles proceeded. After than fourth cycle, the IR drop of the pristine film continuously increased and gradually saturated around the 50th cycle. In contrast, the resistivity of the coated film showed only a slight increase, which was only one-seventh of that for the pristine film at the end of the 50th cycle. Their discharge capacities consistently decreased with resistance growth. The potential profiles during the discharge also reflected the resistance growth; as the resistance increased, the profile shape became linear. These phenomena implied both the presence and growth of a resistive component on the pristine NCM film. Additionally, they had quite a similar change in shape to that of the discharging curve of the polycrystalline, as shown in Figure 33

Next, the origin of the resistance was investigated by the ex-situ method. Cycled electrodes were taken from the coin cell and rinsed with DMC solvent. Figure 42 shows the top view of the film electrodes after the cycle. Obviously, there were many impurities on the surface of the pristine membrane. Although localization of the impurity products were observed, it is possible that some films were washed out with DMC rinse because of a rather flat mirror-faced surface of the thin film. In contrast, the LZO-coated film electrode showed no film-like impurities, but rather small dots were observed. No Zr component could detected, but there was a small amount of carbon. It was thought that these impurity dots originated from the pristine NCM spot because the very short and weak PLD coating of the LZO made some uncoated spots on the NCM film surface

The cross-section TEM images of these cycled films are shown in Figure 44 and 45 for pristine and LZO-coated film, respectively. Before the lamellas were dug with the focused Ga ion beam, the film surfaces were protected with a Pt sputter coating layer. Figure 44 proves that the correct estimation of each films' thickness was 30 nm. Additionally, the images showed the obvious byproduct presence on the NCM surface, which had a thickness of more than 15 nm. Although it did not provide an accurate composition, the EDS analysis revealed the presence of carbon and oxygen in the byproduct film. The presence of carbon was also observed with NanoSIMS analysis in

the product base's particle grain boundary after its cycle capacity had faded. This consistency implied a resistive byproduct of Li_2CO_3 or lithium alkyl carbonate. Hence, 15 nm resistive film easily formed on the interface between the electrolyte and the NCM (104) active face. In general, a 10μm size NCM particle does not show such a fast capacity fade with this battery test. Fast degradation of pristine NCM film seems to originate from its sensitive nature, which only has an interface volume from the productive large particle's scale.

Figure 45 shows the LZO-coated film, which showed quite a different result from that of the pristine film. There was quite a clean (104) surface of original NCM. EDS also indicated no impurity component other than oxygen. These observations revealed the LZO effect to prevent the byproduct generation on the NCM R-3m active edge face with less than 1 nm thickness.

These LZO coating effects appeared not only on the surface but also on the NCM bulk. Figure 46 shows the electron diffraction of the NCM cross-section of cycled film with an LZO coating. NCM spots along the (104) projection were quite bright and had high contrast, which was the same as the SRO substrate. In addition, the stacking image of both spots showed good matching with their texture, indicating excellent structural sustainability of the LZO-coated NCM.

Figure 47 shows that, for pristine NCM, there is evidence of Ni disordering in the NCM R-3m structure. Although, the NCM showed a clear (104) projection plot with no impurity spots, which was the same as for the LZO NCM. However, the dot distance was 1 to 2% smaller than that of the SRO. As described above, the Ni based R-3m structure had a tendency toward Ni migration into the Li site (cation mixing). If the same

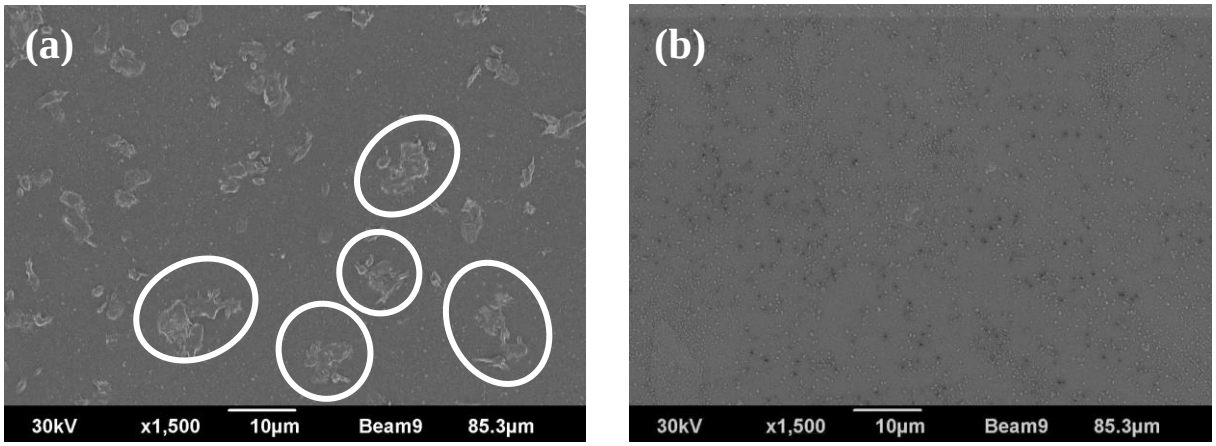

Figure 42 SEM top view image of cycled PLD electrode for pristine (a) and Li_2ZrO_3 coated (b)..

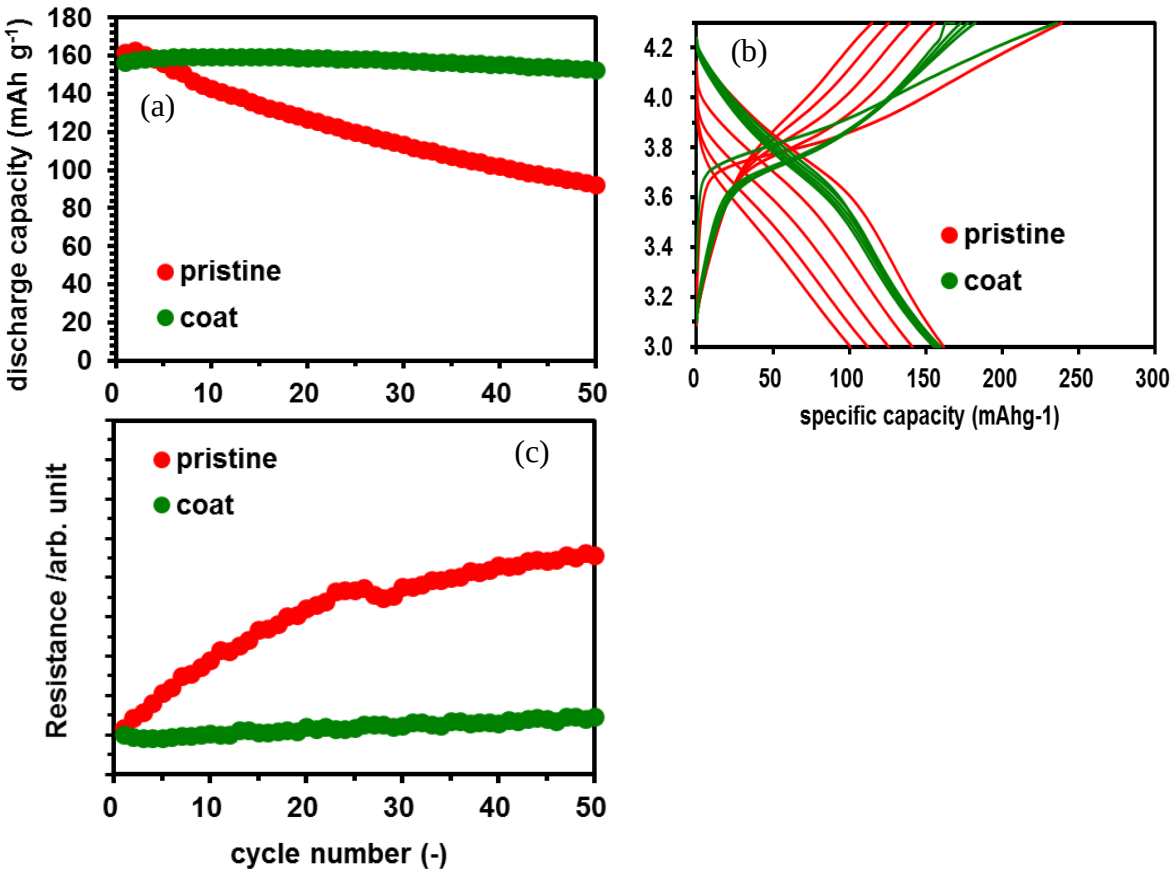

Figure 43 Results of charge discharge cycle test, capacity retention (a), Potential profile every 10th cycle (b), Estimated resistance with IR drop at DOD 0% (c).

Ni disordering described in Figure 19 had taken place, the (104) projection would not have been able to distinguish cation mixing because both the Ni and Li site were arranged in the same (104) projection array. The other way to judge the mixing is through the lattice's constant change. Figure 48 shows the lattice expansion (spot pattern contraction) with cation mixing, which is consistent with what we currently understand. However, the Ni distribution from the perpendicular projection should be confirmed such as (-120). Therefore, the presence of resistive film seemed to be a promoter of an electronic double layer that resulted in an unexpected side reaction to the interface.

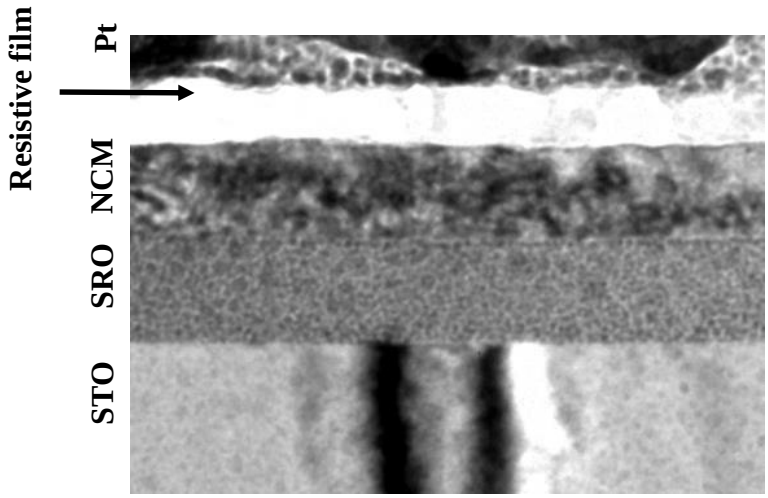

Figure 44 Cross section TEM image of pristine PLD electrode, after cycle test.

Table 5 Cross section TEM EDS of pristine PLD electrode, after cycle test.

at%	C	O	Ni	Co	Mn	Sr	Ru
Resistive film	35	54	0	0	0	0	0
NCM	0	71	6	15	8	0	0
SRO	0	53	0	0	0	24	24

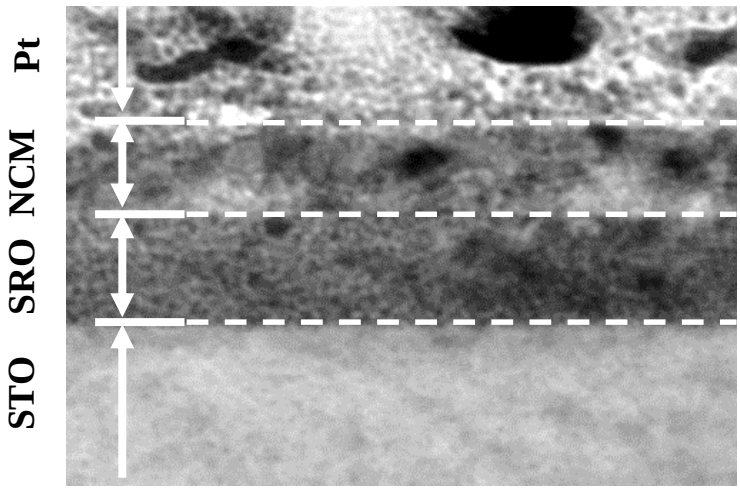

Figure 45 TEM image for Cross section of LZO coated PLD electrode, after cycle test.

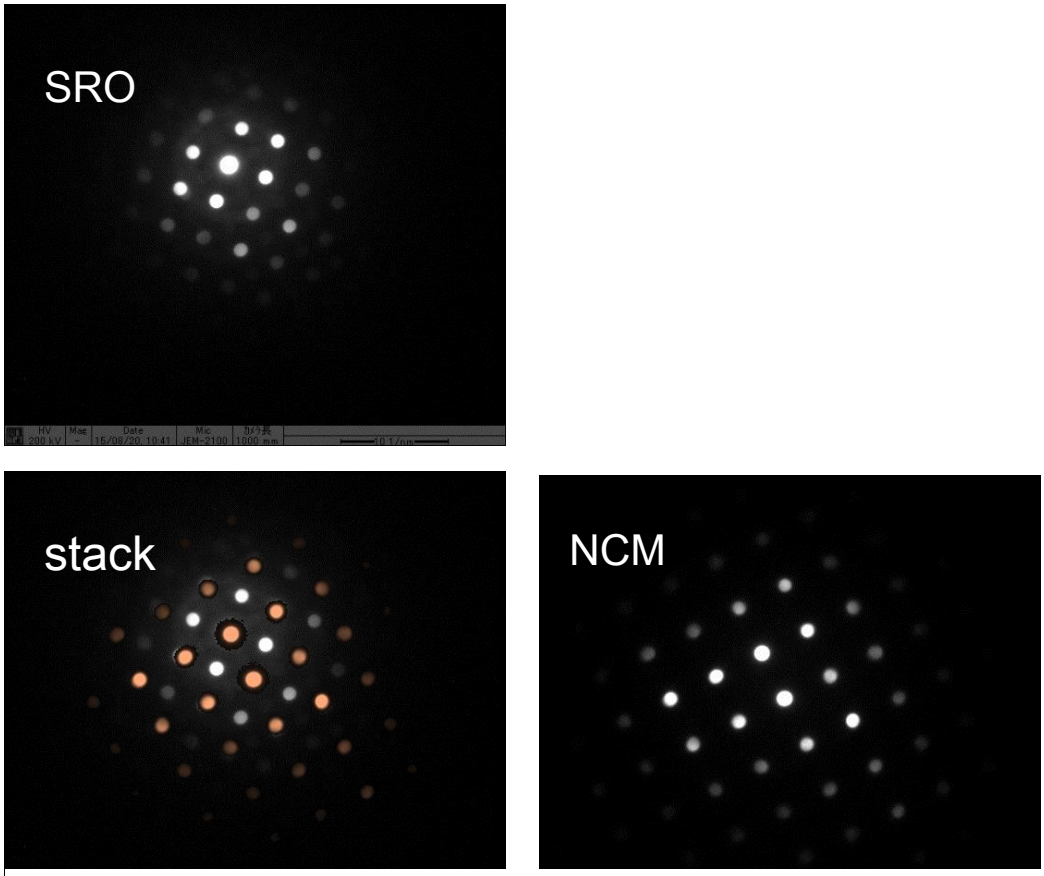

Figure 46 Electron Diffraction for the Zr Coated PLD electrode after cycle test..

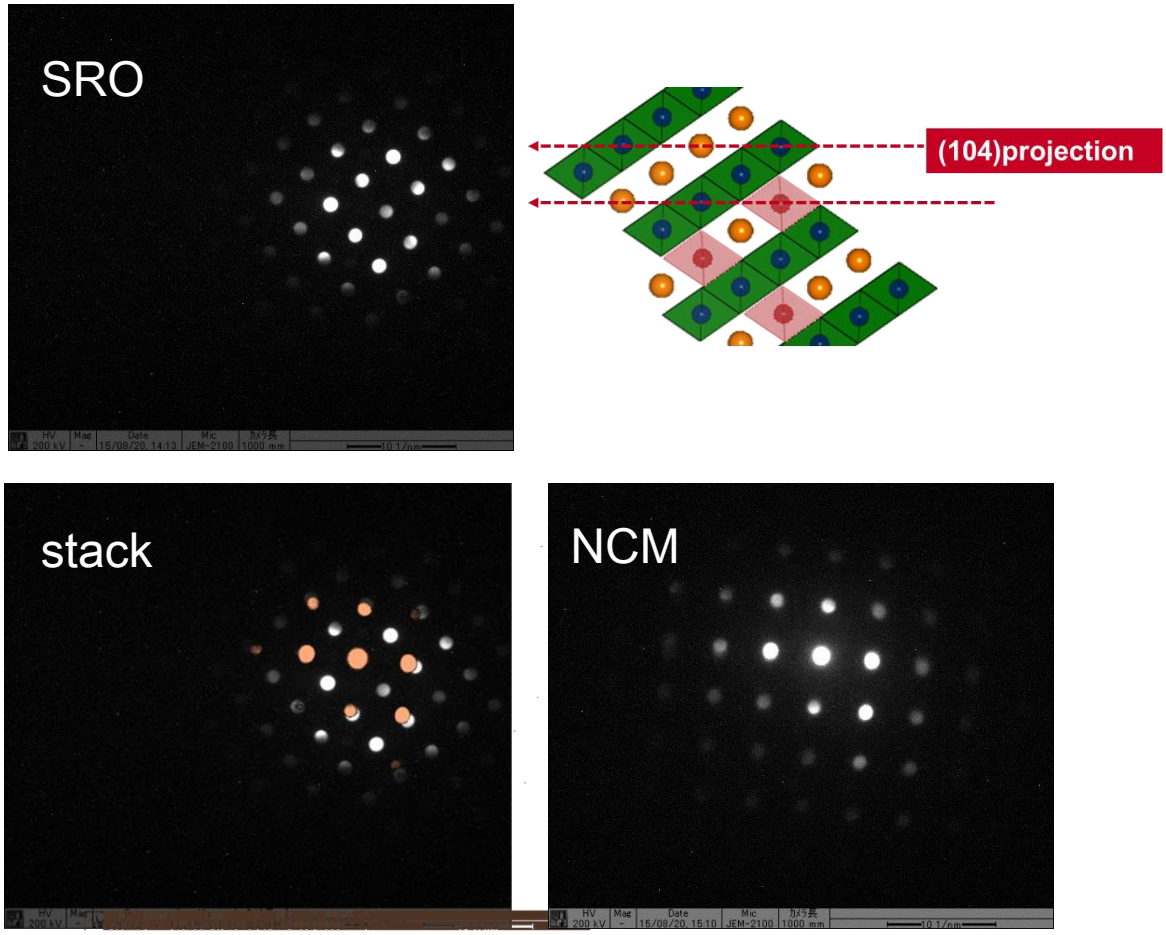

Figure 47 Electron Diffraction for the Pristine PLD electrode after cycle test.

Table 6 Cross section TEM EDS of LZO coated PLD electrode, after cycle test

at%	C	O	Ni	Co	Mn	Sr	Ru
interface	0	99	0	0	0	0	0
NCM	0	56	11	22	11	0	0
SRO	0	46	0	0	0	25	29

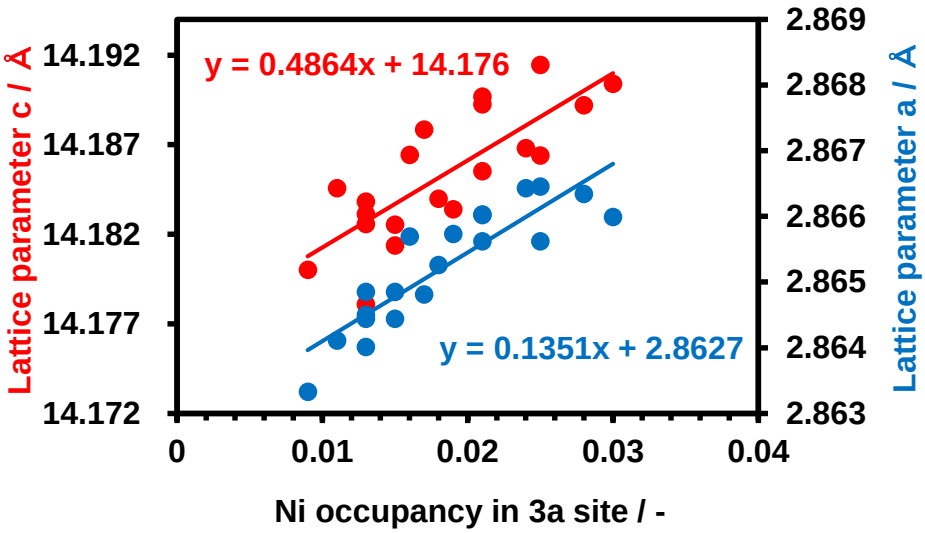

Figure 48 Lattice expansion with Ni migration to 3a Li site.

The above results revealed that there were many similar phenomena between grain boundaries in the productive cathode active particle and epitaxial thin film active material. The consistent interfacial side reactions were resistive to film reaction, byproduct compound, Ni migration, resistance increase, capacity fade, and so on.

2.3. Result (Feedback of the thin design).

Hence, it is quite useful to transfer this knowledge for the commercial product. In this case, it was a grain boundary modification. Figure 49 is an analysis of fine structure NanoSIMS analysis results for the product NCM polycrystalline, in which LZO had been introduced to the grain boundary. The line analysis shows the clear mirror symmetry, indicating each crystallite was coated by LZO.

Figure 51 shows the 100-cycle capacity change with a condition of 60°C and 1C, summarized with all the NCM materials in this study. Figure 52 is a cross-section mapping of Li-C, which coexisted after the cycled NCM. With NCM, in which LZO was introduced to a coated crystallite in it, there was almost no cracking, and no carbon was detected in the particle; namely, it was able to keep its original nature. These phenomena were quite similar to those of PLD epitaxial thin films.

The results obtained in this study would be quite effective for the screening and exploration of other coating components. Protective modification for the grain boundary is quite important, even if in the 10μm order of large particles, particularly with grain unit coating. It seems to be a promising technique to rebound the crystal expansion and extraction and result in long life battery use.

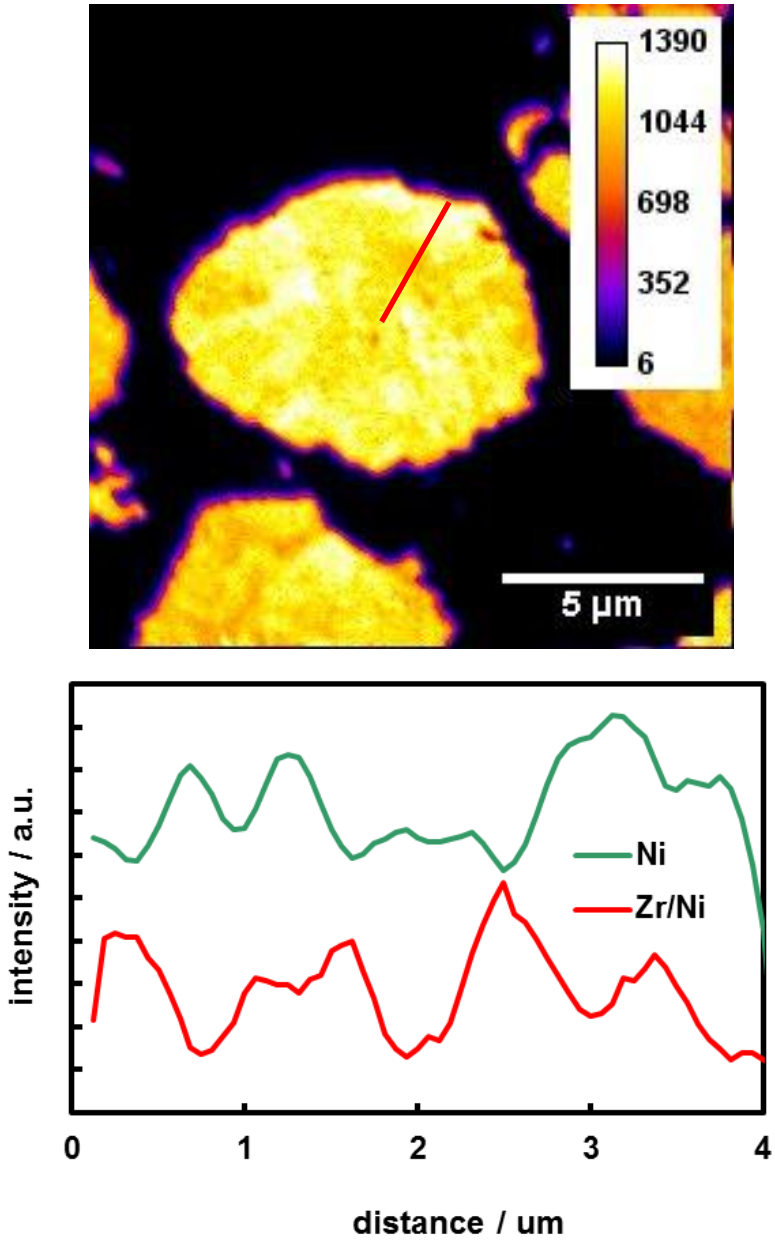

Figure 49 NanoSIMS analysis result for the product NCM, in which Li_2ZrO_3 has introduced in its grain boundary.

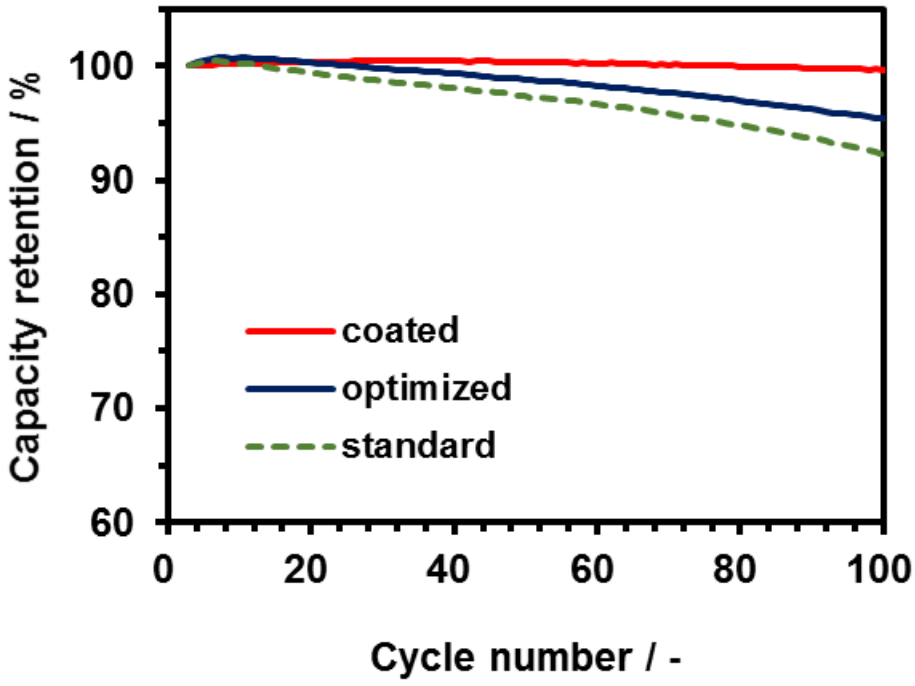

Figure 51 Cycle performance of polycrystalline NCM.

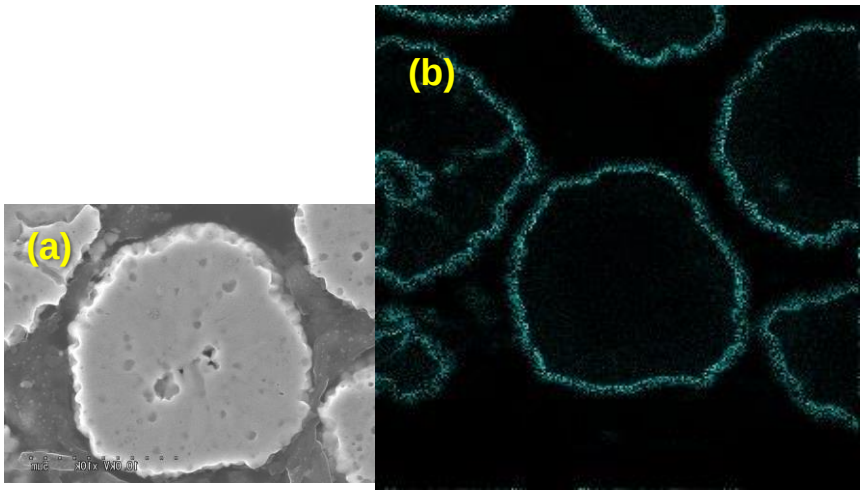

Figure 52 Cross section Image of Zr introduced NCM after 100 cycle test, SEM image (a), Li-C mapping (b) by NanoSIMS analysis.

Chapter 3. High-voltage interfacial reaction in cathode matrix

3.1. High-Voltage interfacial reaction and its improvements

3.1.1. Introduction

As described in 1.1, deep charging of the battery causes the cut-off voltage to rise. To avoid potential safety issues, durability at 4.5 V is necessary. However, 4.5 V is no longer the normal point at which the battery components such as the electrolyte, conductive agent, and binder begin to exhibit abnormal reactions. Here, this thesis describes the contributions of various conductive agents to gas generation. The interfacial reaction model and the key factor for improvements are also discussed.

HV spinel is a useful active material to study the cathode-electrolyte interface in the high-voltage state because it has a redox potential of 4.7 V versus Li^+/Li. The novel results of this investigation were an abnormal electrochemical reaction of the conductive agent and a local battery-like reaction including HV spinel, the electrolyte, and the carbon materials. The proposed reaction is discussed in this chapter.

Electrochemically stable electrodes at high voltages are in strong demand for power sources for EV and grid energy storage. Although many high-voltage cathode active materials for lithium-ion batteries have been developed [75]-[83], [47]. the large gas evolution at the positive electrode caused by electrolyte oxidation obstructs the commercialization of these materials as shown in Figure 53. This gas evolution is caused by the interfacial reaction between the cathode and electrolyte. Intensive studies have been performed to determine the reaction mechanism[84]-[89], elucidate the compositions of the passive film that result in the gas evolution[90]-[93], and reduce the reaction by surface modification[94]-[100]. Several approaches have been reported to overcome these issues such as surface modification of the cathode and the inclusion of additives in the electrolyte [98], [101], [102].

However, the reaction between the electrolyte and carbon additives as conducting agents has not been heavily investigated for high-voltage cathodes. The reaction between carbon and the electrolyte (or supporting electrolyte salt) has been reported to involve anion intercalation to the carbon electrodes [85]. Generally, Li^+ de-intercalates from the cathode when the battery has been charged. However, when the active material originally contains no extractable cation, the charge valance of the system is maintained by anion intercalation. In an electrochemical dual graphite (GR) cell using carbon as both the

cathode and anode, for example, anion intercalation to GR as the positive electrode proceeded with a charge over 4.5 V [86]. The anion intercalation accompanied gas evolution, which originated from electrolyte decomposition at a low-rate charge-discharge current. These results suggest that a conductive agent such as carbon conductive agents in the positive electrode might induce similar reactions as GR in the voltage region in which the high-voltage cathode works as an intercalation electrode. Furthermore, Pieczonka et al. reported that carbon conductive agents plays a key role in the oxidative decomposition of the electrolyte in the $LiNi_{0.5}Mn_{1.5}O_4$ (LNMO) cathode system [102]. Much larger amounts of decomposition products were observed on the carbon surface than on the LNMO surfaces [87], which indicates high activity of the carbon additives.

In the present study, the characteristics of carbon conductive agents were examined in the high-voltage region using high-voltage spinel cathode materials. The carbon conductive agents, which coexist with the active material and binder in the actual cathode system, provide the interface with the organic electrolyte. The anomalous anion intercalation in the high-voltage region was examined, and the effect on the powder properties was clarified for the mixture of cathode materials with various specific surface areas, crystallinities, metallic impurities and densities, and carbon conducting agents (acetylene black (AB), furnace black (FB), graphite (GR), and specially customized AB). Quantitative analysis of the gas evolution caused by the carbon materials is reported.

Figure 53 Typical picture of High Voltage swelled Laminate cell.

3.2. Experimental

3.2.1. Conductive agents

Table 7 summarizes the powder properties for each conductive agent used in the

present study. Conventional and customized carbon conductive agents were used, including AB (crystallite size: 35 nm); high-crystalline AB (crystallite size: 60 nm), AB (H-C); and AB with large specific surface area, AB (L-S) (Denki Kagaku Kogyo K. K.). Furnace black (FB) was also used as another commercial carbon conductive agents (Super-P: TIMCAL). Furthermore, GR was selected as a well-crystallized conductive agent.

Table 7 Powder properties of various conductive agents.

Sample name	Specific surface area (m^2/g)	Crystallite size (nm)	Impurity (a.u.)
AB	68	35	2
AB(L-S)	133	25	2
AB(H-C)	34	60	42
FB	63	22	8
GR	20	75	25

Table 8 Formulation of each Electrode used this study.

	LNMO	GR	AB	AB (H-C)	AB(L-S)	FB	PVDF
Electrode-1	0.85	0	0.10	0	0	0	0.05
Electrode-2	0.90	0	0.05	0	0	0	0.05
Electrode-3	0.85	0	0.05	0.05	0	0	0.05
Electrode-4	0.85	0.05	0.05	0	0	0	0.05
Electrode-5	0.90	0	0	0	0.05	0	0.05
Electrode-6	0.90	0	0	0	0	0.05	0.05
Electrode-7	0.80	0	0.10	0	0	0	0.10

A stoichiometric composition of LNMO with low specific surface area (BASF TODA Battery Materials LLC.) was used as the cathode material. A $LiCoO_2$ (LCO) cathode material (BASF TODA Battery Materials LLC.) was used as the standard electrode to elucidate the gas evolution from the carbon anode.

Laminate cells with a capacity and the volume of approximately 0.1 Ah and 7.5 cm^3, respectively, were evaluated for the gas evolution. The cells were composed of approximately 0.7 g LNMO and 1 ml 1M-$LiPF_6$/(EC+DEC) (1:1 in volume) electrolyte. No additives for the electrolyte were used in order to evaluate the fundamental properties

of the electrode. Each conductive agent was thoroughly mixed with LNMO and PVDF in appropriate ratio as listed in Table 8 to obtain a good paint property and accurate capacity and was then coated on an aluminum current collector to dry at 110 °C in air. Then, the electrodes were compressed until the electrode density reached 3.0 g/cm^3 followed by vacuum drying at 100 °C overnight. The anode was a mixture of MCMB (from JFE chemicals; TKG-L) and PVDF (from KUREHA; L#7208) with a MCMB/PVDF ratio of 6/4 by weight. The separator used in the present study was a polypropylene sheet (from Celgard LLC; #2400), which is stable against high-voltage usage.

3.2.2. Gas generation test

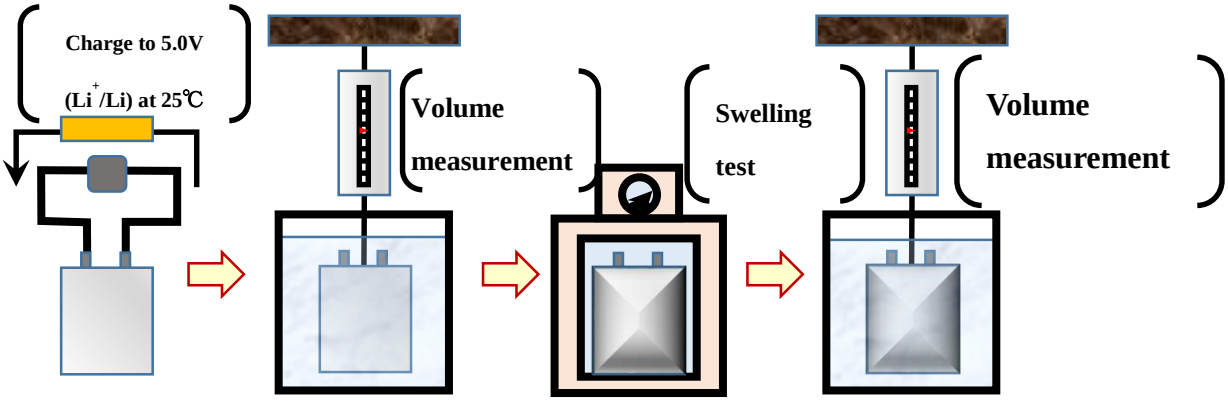

Figure 54 Schematic diagram of the experimental procedure for swelling measurements

The capacity of the laminate cell constructed was confirmed by the 1st cycle charge and discharge test. Then, the cells were charged until the cell voltage reach 5.0 V and maintained at that voltage until the current was decreased to 1/100 C at 25 °C. The laminate cell charged to 5.0 V was then stored at 60 °C in the open-circuit situation. The volume change during these storage processes was measured every 24 h. The cells stored in the oven were removed for volume measurements using the Archimedes method at 25 °C.

The amount of gas evolution contributed by each cathode component was determined by solving the determinant, which consisted of each electrode's composition under the condition that the gas evolution was proportional to the mass of each cathode component. To analyze the results, the fundamental electrochemical properties were measured using a 2032-type coin cell, in which the working electrode was composed of each conductive agent and binder in a 1:1 weight ratio on an aluminum current collector

(carbon electrode), and the counter electrode was Li metal. The cut-off voltages for the cyclic voltammetry were 3.0 and 5.0 V with a scan rate of 0.17 mV s^{-1} at 60 °C.

3.2.2.1. Cyclic voltammogram

The same cell construction described above was used as that for the cyclic voltammogram experiments. The test conditions were cut-off voltages of 3.0 and 5.0 V, a sweep rate of 0.17 mV min. $^{-1}$ in 60°C controlled incubator.

3.2.2.2. Alternative Current Impedance

Impedance spectroscopy measurements were collected with a Solartoron-1252A, a frequency response analyzer with a Solartoron-SL1287 electrochemical interface. The measurement conditions were as follows: applied amplitude test condition of 10 mV and frequency range of 10-1 to 3×10^5 Hz. The data were obtained with the cell potential every 0.2 V ranging from 4.0 to 5.2 V. The cell was equilibrated for 30 min after the constant voltage step using each intermittent charge and discharge mode at 60 °C.

3.2.2.3. Leak current

Before the Impedance measurements at predetermined voltage, cells were charged or discharged with a constant current then kept the voltage for 20 min. the leak current or residual current were measured in that time.

3.2.2.4. Charge-discharge tests

Galvanostatic charge-discharge tests were also performed for the carbon electrodes described above. The same cell construction was used as that for the cyclic voltammogram experiments. The test conditions were cut-off voltages of 3.0 and 5.0 V, a current density of 0.3 mA mg^{-1}, and a charge-discharge cycle number of 81 cycles.

3.2.2.5. *in-situ* XRD analysis

The phase changes of the carbon conductive agents during the charge-discharge test were examined by in-situ X-ray diffraction (XRD) measurements using an in-situ XRD lithium battery cell (Rigaku Corp.; in-situ attachment) and Smart-Lab diffractometer (Rigaku Corp.). The XRD patterns were recorded using Cu Kα radiation (45 kV, 200 mA), 2θ diffraction angles ranging from 20° to 40° with a 0.02° step width,

and a fixed time of each step of 1.0 s. The cell voltage was maintained during the XRD measurement at 5.0 V and 3.0 V for the 100% and 0% charge states, respectively, at the 81st cycle.

3.2.2.6. OCV test

The open-circuit-voltage (OCV) stability of the carbon electrodes once charged to 5.0 V was evaluated by monitoring the OCV during the storage at 60 °C.

3.3. Results and Discussions

3.3.1. Swelling: Quantification of the gas evolution

Table 8 summarizes the electrode compositions used in the present study. Each composition was determined to have an appropriate paint viscosity, which avoids excess carbon addition. The number of electrodes was determined, which allows the construction of a square matrix to solve simultaneous equations.

Table 9 summarizes the amount of gas evolution from each electrode during the 60 °C storage. As the swelling data contains both the cathode and anode gas evolution, the anode gas evolution was subtracted from the swelling raw data in order to obtain a precise value of the cathode gas evolution. The gas evolution from the GR anode was produced by solid electrolyte interphase (SEI) formation upon charging the battery. To evaluate the amount of gas evolution resulting from that reductive reaction, the cell using the LCO cathode was examined, as the gas evolution from the LCO cathode is almost negligible in the voltage range examined (3.0–4.5 V). The gas evolution of the LCO/MCMB laminate cell was determined to be only 0.007 cm3 per gram of MCMB (0.02 $cm^3\ g^{-1}$ per LCO/MCMB cell), which has almost no effect on the gas evolution from the LNMO cathode. The gas evolution from the aluminum current collector can be neglected, as Al metal does not participate in the electrolyte oxidation because of the protective film that is formed with the F^- anion of the $LiPF_6$ salt [103].

The amount of gas evolution contributed by each cathode component was estimated from the experimental results of the laminate cells measured in each 24-h interval. The calculations were performed under the assumption that the gas evolution is proportional to the content of each electrode component.

Figure 56 shows the amount of specific gas evolution from each electrode component during the 60 °C storage; 8 to 16 times more gas was generated by the carbon

materials than the LNMO cathode active material. This finding indicates that the gas evolution was induced not only by the high-voltage cathode, LNMO, but also by the carbon used as conductive agents. These results demonstrate the importance of the reaction between the carbon additives and electrolyte even for the cathode electrode matrix. The amount of gas evolution depends on the crystallinity and specific surface area of the AB; the AB (H-C) with a crystallite size of 60 nm generates more gas than the AB with the smaller crystallite size of 35 nm, and the AB (L-S) with a specific surface area of 180 $m^2 g^{-1}$ generates more gas than the AB with the specific surface area of 68 $m^2 g^{-1}$. Figure 57 is a rearrangement of that of Figure 56 with a vertical axis of cm^3 gas per cm^2 conductive agents. The graph could separate carbon samples into two group, one is a 60 nm crystallite size group, ant another is a 30 nm group, that indicate that the larger crystallite of the carbon agent increase the gas generation. In contrast, glassy carbon has no gas generation in this study, that consistent with our consideration because it is perfectly amorphous.

The amount of gas evolution continuously increased with storage time for all the carbon materials and was not saturated during the experimental periods used in the present study. In the case the SEI formation on the anode was reported only during the first stage of the charge and discharge cycle, and thus, the relative gas generation occurred only during the first stage. On the contrary, the finding in present study indicates that the cells continued to continuously swell with side reactions that generate gas, such as electrolyte decomposition on the cathode. As the electrolyte system used in the present study contains no additives such as FEC [101] or LiBOB [102] that prevent oxidative decomposition of the electrolyte or form a protective surface layer, the electrolyte provides no effective SEI formation, resulting in the gas evolution during storage.

Table 9 Gas evolution from each electrode.

	0h	24h	48h	72h	96h
Electrode-1	1.3	4.7	7.7	11.6	29.5
Electrode-2	1.4	4.3	6.7	9.6	26.3
Electrode-3	1.4	5.9	9.9	14.4	31.6
Electrode-4	1.6	5.2	8.7	12.4	29.4
Electrode-5	1.4	5.5	8.3	12.0	29.6
Electrode-6	1.5	4.6	7.4	10.6	27.7
Electrode-7	1.2	4.4	8.3	12.4	29.7

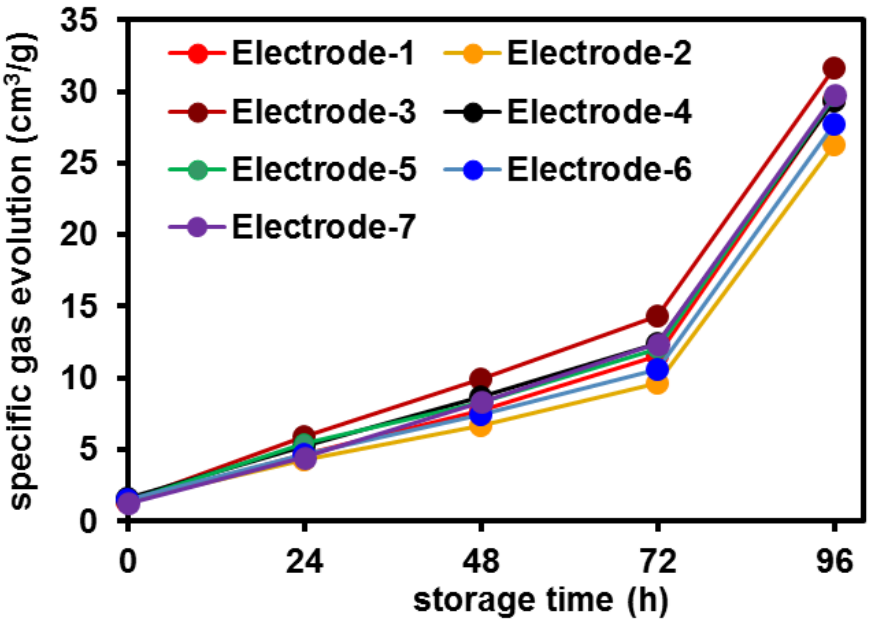

Figure 55 Gas evolution from each formulated cathode.

Table 10 Specific gas evolution from each cathode component.

	0h	24h	48h	72h
AB	0.17	10.82	25.26	46.08
AB(L-S)	0.09	33.34	56.92	93.91
AB(H-C)	2.24	35.04	69.11	101.52
FB	1.67	17.07	39.29	65.37
GR	5.46	21.50	44.59	61.82
Glassy Carbon	0	0	0	0

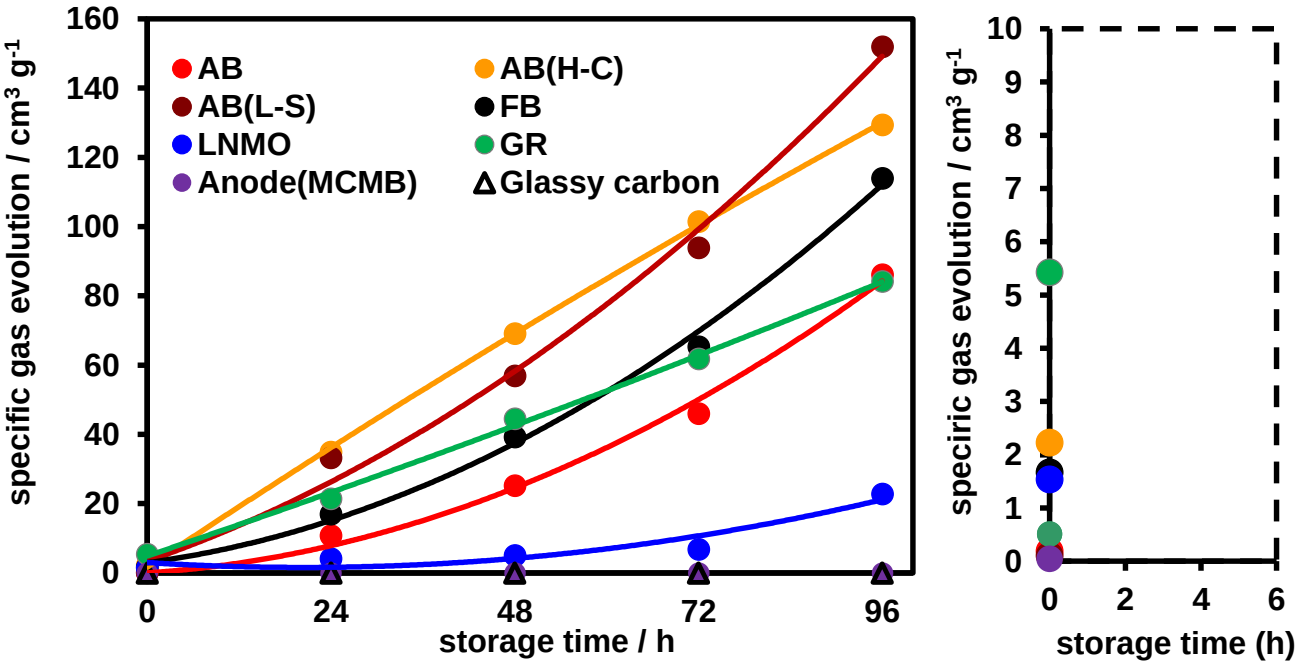

Figure 56 Specific gas evolution from each cathode component.

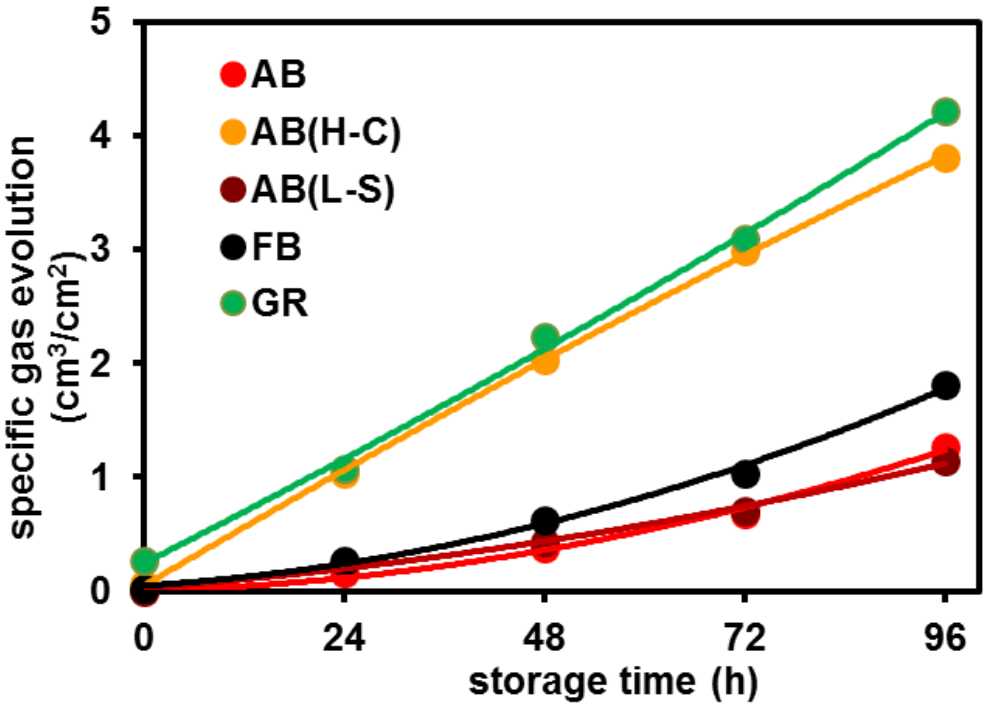

Figure 57 Specific gas evolution as a function of specific surface area of each conductive agents.

3.3.2. Cycle test for each carbon electrode

As carbon materials show anion intercalations in high-voltage regions [104]-[106], a reaction between the carbon and supporting electrolyte might be expected. The electrochemical reactions of the carbon materials in high-voltage regions were therefore examined using high-voltage galvanostatic charge-discharge cycle tests for the conductive agents listed in Table 7

The cells were examined without active cathode materials and tested at 60 °C. Figure 58 shows the discharge capacity changes with cycling during the high-voltage charge-discharge cycling test for the cells using AB, AB(H-C), AB(L-S), and GR as working electrodes. The cells show the charge-discharge behavior with a capacity of 5–40 mA h g^{-1}. Figure 61 show changes in the potential profiles every 10 cycles for the cells with GR, AB, and AB(H-C), and AB(L-S) electrodes, respectively.

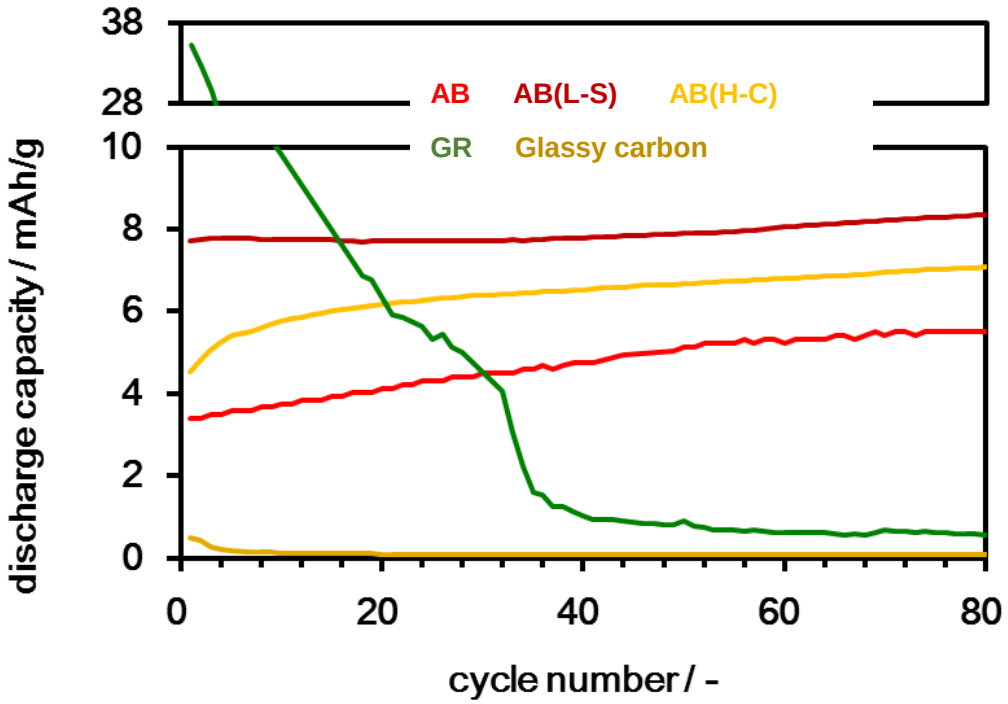

Figure 58 Cycle performance of various conductive agents.

Significant differences in the cycling characteristics between GR and the other carbon materials (AB, AB(H-C), AB(L-S)) were observed. The cell with GR exhibits high capacity only during the early stage of cycling; after the steep capacity decreasing during the 5 cycle, it gradually decreases until the 30th cycles, and then, almost no capacity is retained after 40 cycles. However, the cells with the other carbon materials, AB, AB(H-C), AB(L-S), exhibit discharge capacities of 5–10 mA h g^{-1} at the first cycle, and a gradual increase in the capacities occurs with cycling, which is the opposite behavior of the GR electrode.

The discharge curves of GR shown in Figure 61 reveal a plateau region ranging from 5.0 to 4.0 V in the first cycle, which corresponds to the anion intercalation [105][106]. The decrease in the cell voltage indicates an increase in the iR values with cycling. The abrupt decrease in capacity at the early stage of cycling is due to the increase in the cell resistance, which results from the formation of a passivation layer.

The discontinuous capacity drop observed near the 5th and 33rd cycles might be due to the exfoliation of the GR layer [108]. These results indicate that the GR lost its property as a conductive agent in the high-voltage region. And these results also consistent with the result showed in magnified graph of Figure 56, in which the gas evolution that contributed to the GR showed the largest capacity only at the first storage stage.

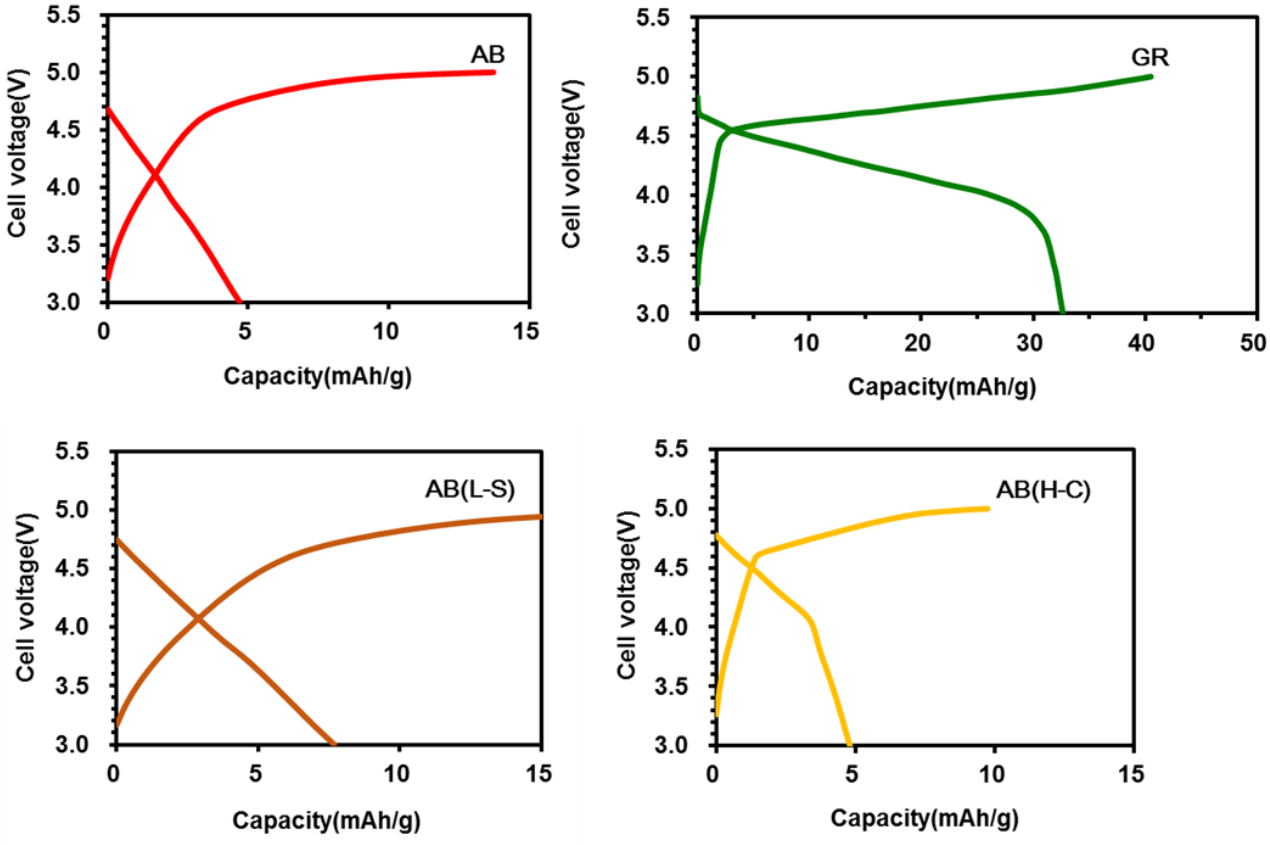

Figure 59 1st charge discharge curve for AB, GR, AB(L-S) and AB(H-C).

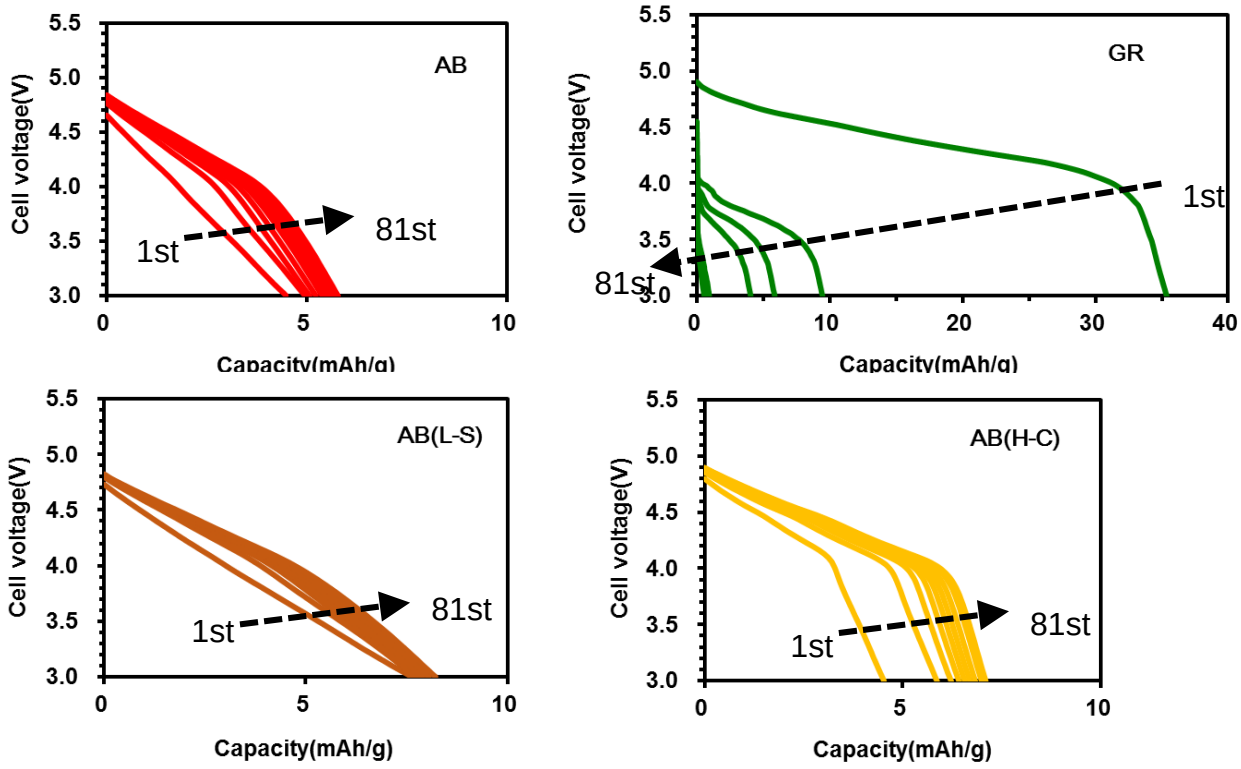

Figure 610 Discharge curve in every 10th cycle during the 1C charge discharge at 60°C.

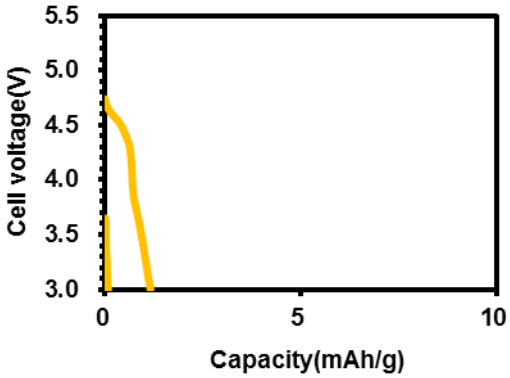

Figure 61 Discharge curve during the cycle test for Glassy Carbon (every 10th cycle).

Both similar and opposite behavior to the GR were observed for the AB electrode on charge discharge cycle test. At first, the similar point is the discharge curves. Figure 61 reveal gradual voltage drops of AB from 5.0 to 4.0 V and from 4.0 to 3.0 V in two steps, which is a typical behavior of the AB electrode. Because the voltage range from 5.0 to 4.0 V corresponds to anion intercalation to the GR electrode [109], the

electrochemical behavior of AB might be due to the anion intercalation to the graphene layers in the AB structure. Next, the opposite behavior of the AB electrode to that of GR was the capacity retention against the repetitive charge discharge cycle. Whereas the GR electrode showed the capacity decrease during the cycle, AB electrodes exhibited capacity increase. As the cycle proceeded, the capacity of the voltage region between 5.0 and 4.0 V increased, and the voltage step that corresponds to the electrochemical reaction became more apparent. A study to evaluate the origin of this specific behavior for the AB is now in progress, and some structural change during more than thousand long cycling has been observed. The investigation is now in preparing for submission.

In the discharge curve of the AB(H-C) electrode shown in Figure 61, the voltage step in the curve is clearer than that observed for AB even during an initial cycle, and the capacity between 5 and 4 V is larger than that for AB. The AB(L-S) electrode shown in Figure 61 has the largest capacity among these three AB electrodes. The discharge behavior is similar to that of other ABs, whereas the voltage step is not as clear as that observed in AB(H-C). Note that the capacity increased with cycling for these carbon materials (AB, AB(H-C), AB(L-S)), which might correspond to the activation process of the anion intercalation reaction for these carbon materials with cycling.

To investigate the activation of the AB electrode, the cycling test was extended to 1000 cycles as shown in Figure 69. AB activation was rapidly started at the beginning of the cycling until the first 100 cycle then gradually saturated to the 1000th cycle. Ex-situ Raman analysis of the electrode was employed to confirm the structural change of AB. As shown in Figure 68, of which intensity is normalized by that of D-band, I_G/I_D ratio of the AB electrodes against the cycle number also over plotted in the Figure 69. It showed good consistency with its discharging capacity.

These experimental results indicate that the unique electrochemical reaction especially, anion intercalation. In the high voltage state, there is a misreading risk if we recognize the carbon materials only as an electron conductor. The evidence of AB anion intercalation is discussed again in-situ XRD.

3.3.2.1. Cyclic voltammogram

Cyclic voltammogram was measured for each conductive agents as shown in Figure 62. As same as galvanostatic charge discharge test, GR showed the largest activity

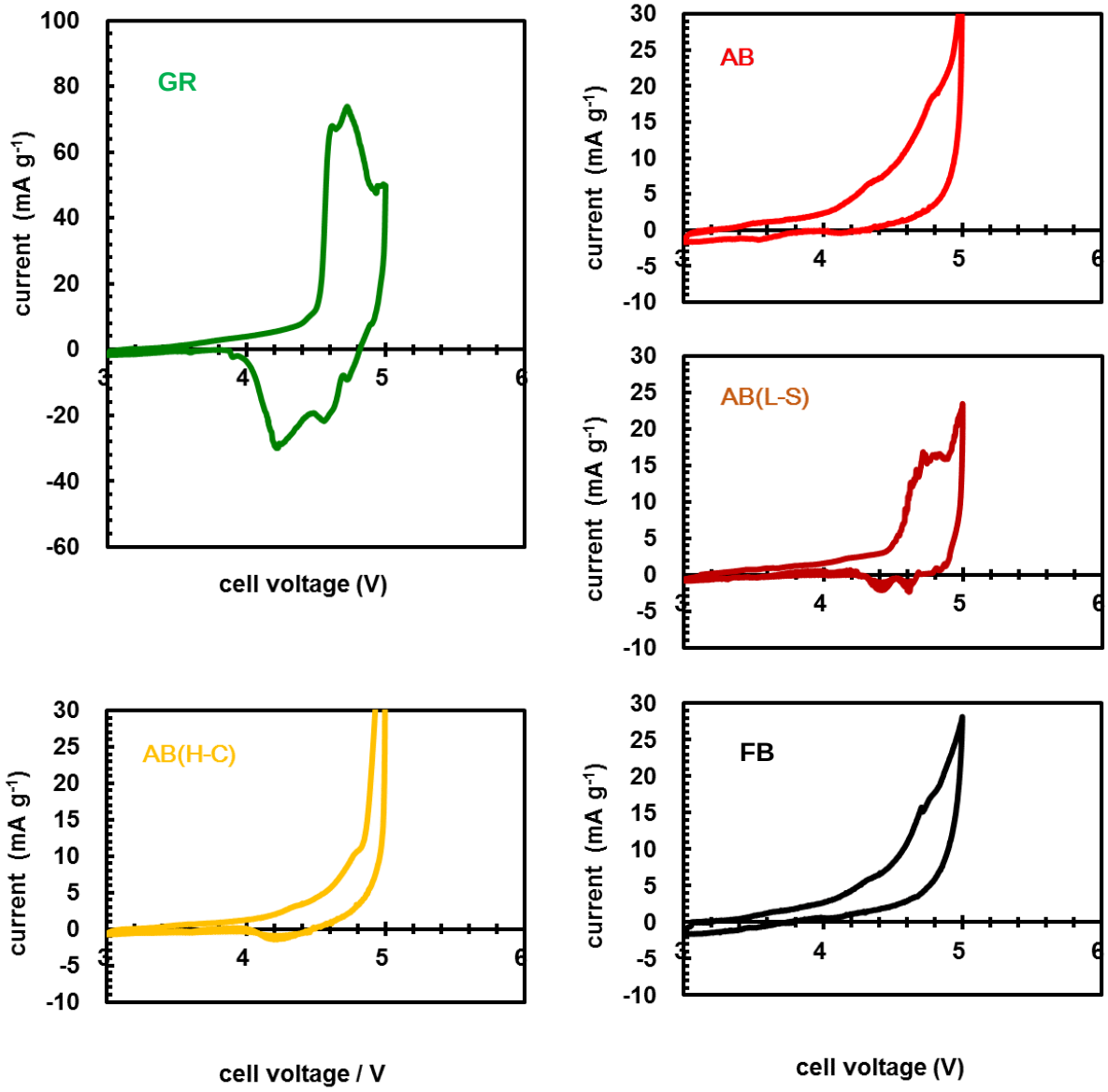

Figure 62 Cyclic voltammetry for various conductive agents at 60°C.

in which starting of oxidation current around 4.5V. It is interesting because this peak consist of three peaks. It might due to the stage change of anion intercalation reported by Dahn [109]. The voltammograms for AB, AB(L-S) and AB(H-C) have not so sharp redox peal, that is same tendency of charge discharge test. Table 11show their reversibility of these redox reactions. These factor have a relation with gas generation.

Table 11 Summary of the main results of cyclic voltamogram for various conductive agents.

	anodic charge / c g^{-1}	reversibility(anodic/cathodic)
AB	0.17	9.5
AB(L-S)	0.10	19.6
AB(H-C)	0.20	19.2
FB	0.24	14.1
GR	0.75	43.4

3.3.2.2. AC impedance

To further analyze the high-voltage behavior, the changes in the impedance and voltage under 0.2-V intermittent charge-discharge were measured for the AB and GR carbon electrodes. Figure 63 presents the potential profiles and impedance growth during intermittent charge and discharge experiments. The frequency response of the AC impedance spectra exhibited a typical shape, which contains a high-frequency intercept, a semi-circle at high to middle frequencies, and an inclined line at low frequencies, attributed to the solution resistance, charge-transfer resistance and SEI resistance, and diffusion processes, respectively. The spectra were evaluated using the equivalent circuit shown in Figure 63 and the Z-View program [114].

Figure 63 shows the voltage and resistance during the 0.2-V intermittent charge and discharge for GR and AB. For the GR shown in Figure 63, the electrochemical reaction starts at approximately 4.5 V with a charge capacity of approximately 100 mAh g^{-1}. A gradual increase in the resistance is observed at approximately 4.8 V, indicating a side reaction in the high-voltage region. In the subsequent discharge shown in Figure 63, the resistance kept increasing and exhibited a remarkable increase at the end of the discharge accompanied by a potential drop to 4.0 V. Although a side reaction such as electrolyte decomposition might be reduced at lower electrode potential, a rapid increase in the resistance in this voltage region suggests a more complicated reaction mechanism

in this voltage region such as anion intercalation. However, the increase in the resistance for AB was smaller than that for GR and was on the same order for the other samples, AB(H-S), AB(L-S), and FB. As mentioned above, the capacity of the GR decreased rapidly with a charge-discharge cycle in the high-voltage region at 60 °C. The rapid impedance increase during the charge-discharge cycle is due to the resistive surface film formed on the GR sheet produced by a side reaction [87], [93], [102], [107],[110]-[113], which might explain the abrupt decrease in the GR cycling performance. In the high-voltage system, the conductive agent is exposed to the high-voltage environment, and the GR also participates in the charge-discharge reaction, which caused activity loss as a conductive agent.

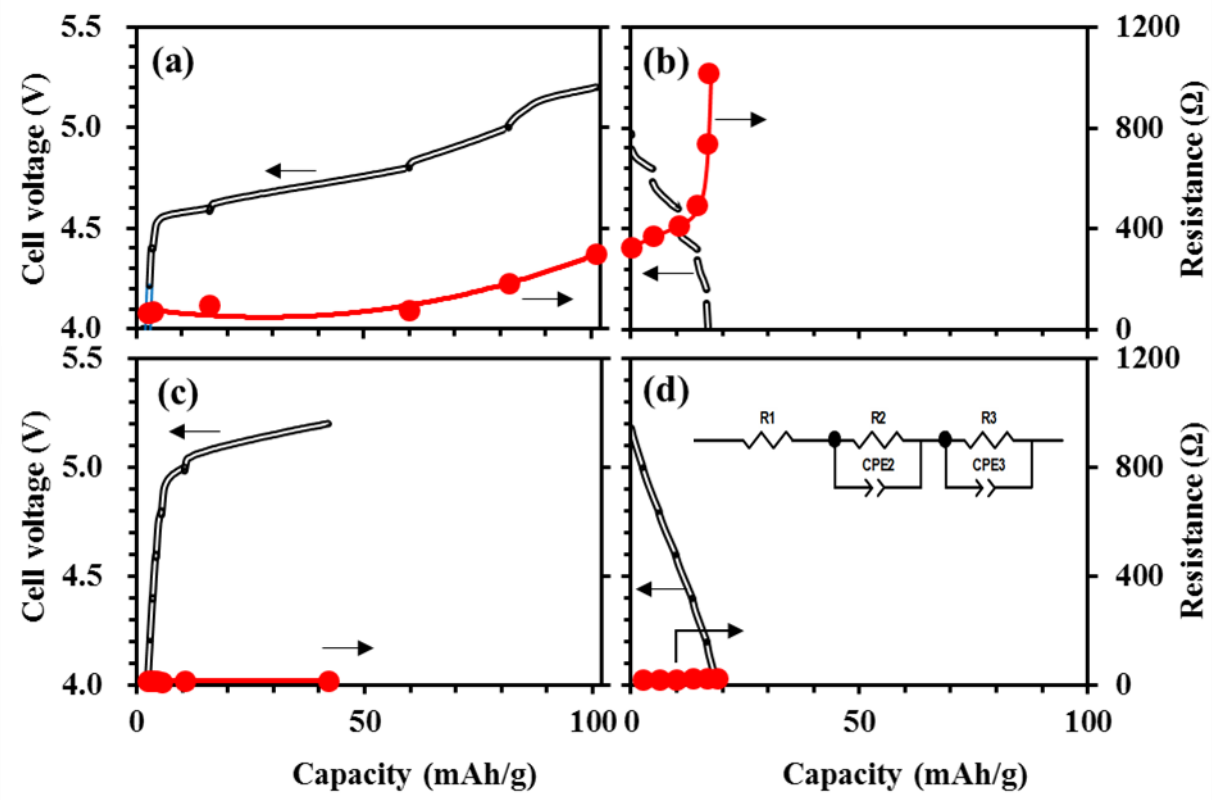

Figure 63 Potential profile and R2+R3 of AC Impedance at 4.0, 4.2, 4.4, 4.6, 4.8, 5.0, 5.2 V.
Each graph of (a), (b) are charging and discharging of AB, respectively.
(c), (d) are those of GR, respectively.

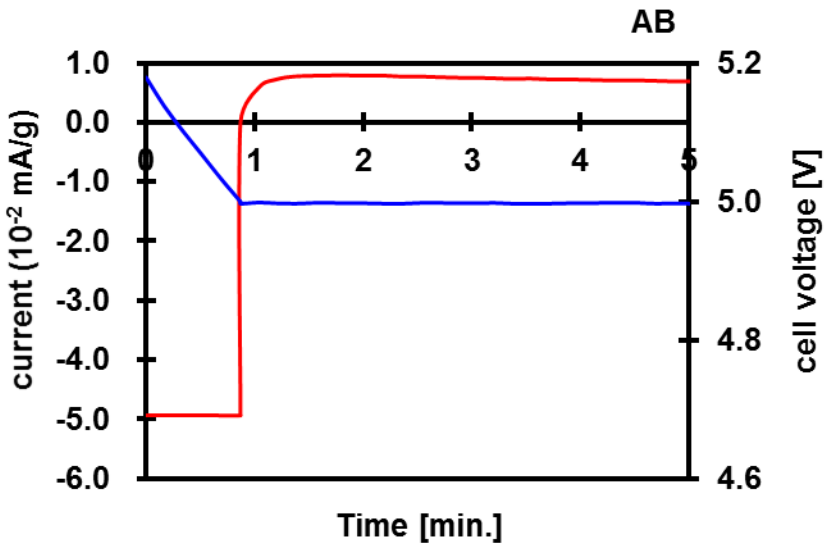

Figure 64 Leak current of AB during a constant 5.0 V mode.

3.3.2.3. OCV effect on the leak current

Figure 64 shows the current changes during a discharge test with the combination of both constant-current and constant-voltage mode. The current behavior suggests the differences between conductive agents and conventional active materials. For the general active materials, the residual discharge current kept flowing until reaching the equilibrium state of the intercalated Li^+ by the applied potential for the constant-voltage mode. Then, the residual current gradually decreased to zero. In contrast, for the conductive agent electrodes using AB, when the discharge mode switched from constant-current to constant-voltage mode, the current direction changed from discharge to charge, which indicates self-discharge behavior in the high-voltage region.

These leak current were observed not only at 5.0 V but also other keep voltage as shown in Figure 66. All leak current value for the various conductive agents are summarized with various keeping voltage as shown in Figure 65.

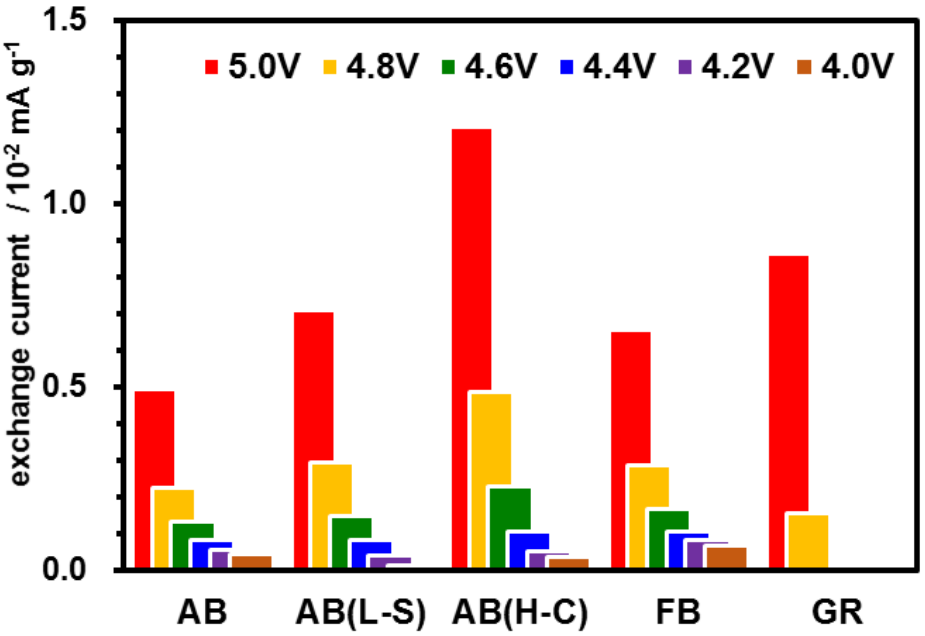

Figure 65 Summary of the exchange current of various conduct agents.

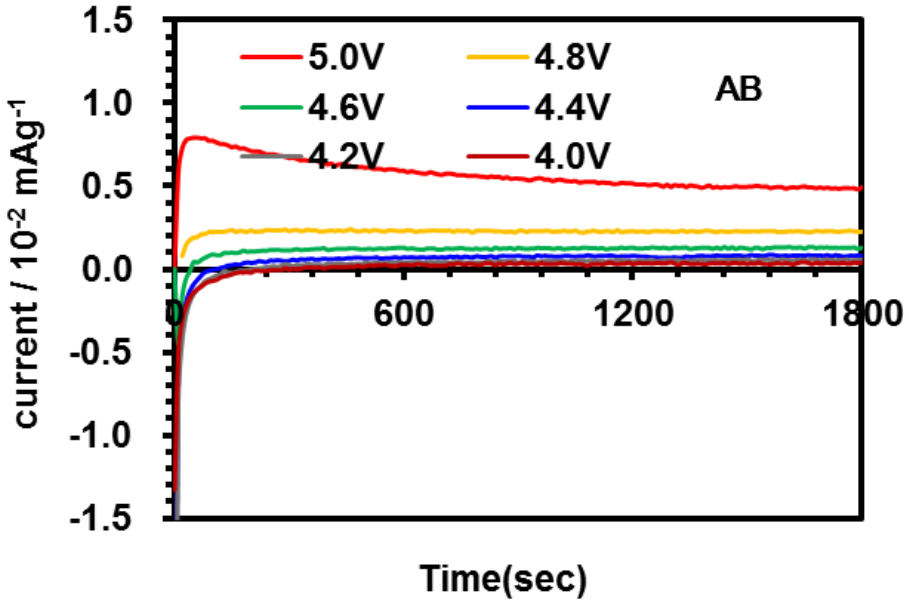

Figure 66 Residual current of AB during constant voltage charging at each voltage.

3.3.2.4. In-situ XRD measurements

No XRD data have been reported for carbon conductive agents during high-voltage charge and discharge cycling except for a GR electrode [105], [109]. The structural changes of AB during the charge-discharge reactions were examined by in-situ XRD measurements. Figure 67 presents the XRD patterns for AB before cycling and at 5 V after the 81st cycling experiment. Before cycling, the 002 diffraction peak was observed at approximately 26° for all the diffraction patterns. After the 81st cycle, two new diffraction peaks together with the original 002 diffraction peak appeared at approximately 2θ = 24.7, and 28.6°. These reflections might be due to a new staging structure produced by the anion intercalation since they could be indexed as 003 and 004 diffraction peak, respectively, with their proposed equation under an assumption that the phase stage was 7. This phase stage is quite similar to that observed for the shallow charging state in the GR electrode [109]. The XRD results of the AB electrodes indicate the multi-phase coexistence reaction for the charge-discharge cycles.

$$n = \frac{1}{\frac{\sin\theta_{00(n+1)}}{\sin\theta_{00n}} - 1}$$

n: stage number

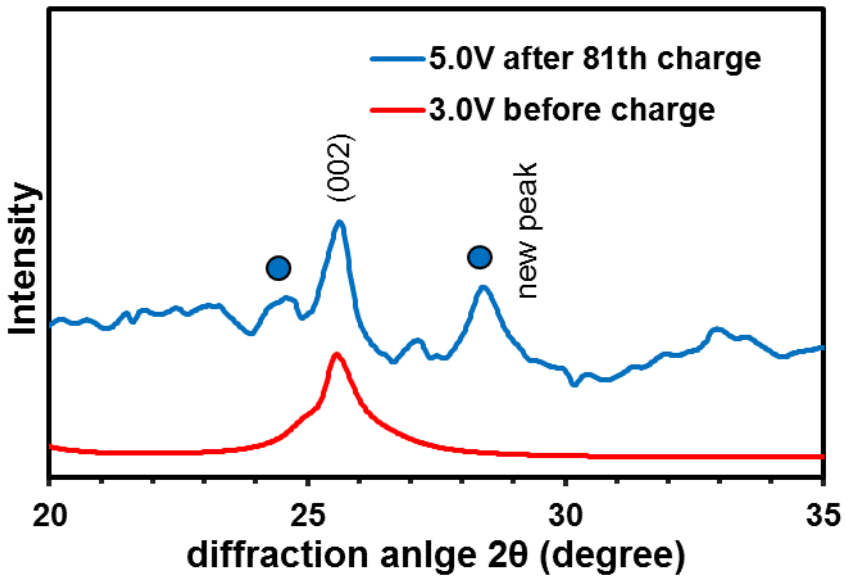

Figure 67 *in-situ* XRD pattern of before and after charging of AB.

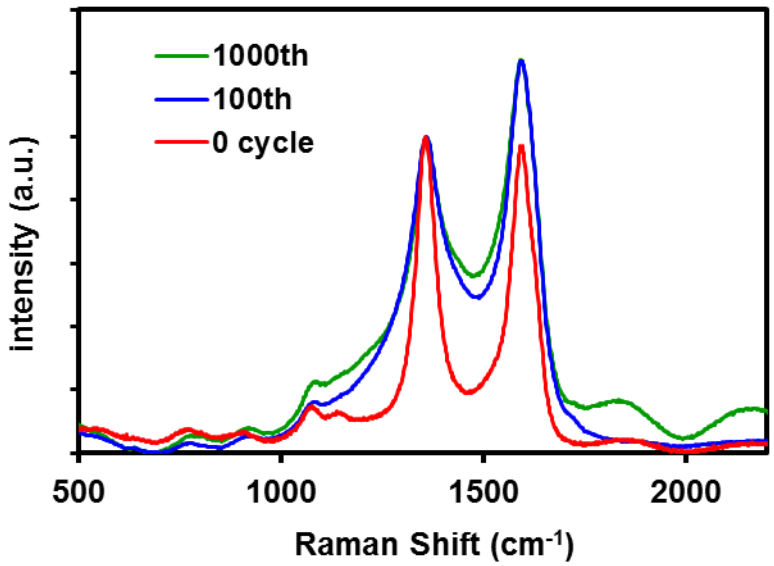

Figure 68 Raman peak of cycled AB electrodes.

3.3.2.5. OCV drop of carbon and its influence

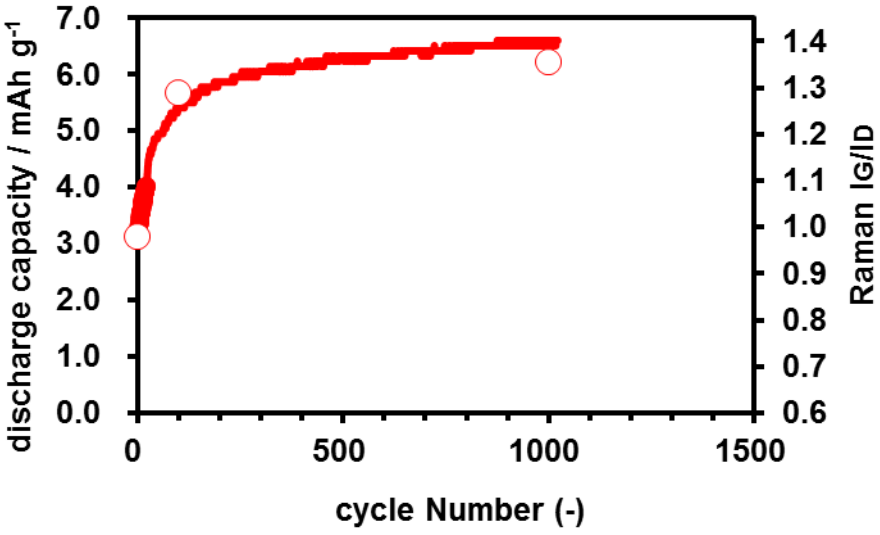

Figure 69 Long charge discharge cycle test of AB and Intensity ratio of G and D-band of Raman spectra.

Figure 70Figure 73 show changes in the OCV for the AB electrode charged at 5.0 V in 60 °C storage. The OCV decreased gradually from 5.0 to 4.2 V, which indicates a spontaneous reaction for the AB in the charged state, for example, the deintercalation

of the anions from AB. During the self-discharge reaction, reduction of the carbon might be accompanied by the electrolyte oxidation and thus form the passivation layer, which causes the resistivity increase in the cells. The self-discharge might be a key issue both in the gas evolution and impedance growth.

3.3.3. OCV drop of complex cathode due to AB

Figure 71 and Figure 72 shows the OCV change for composite cathodes with different AB contents. Figure 73 show the voltage and capacity change during intermittent charging. Once AB was charged, voltage raised drawing its charging curve. The voltage is gradually drop but recovered with same charge shape of potential profile by re-charging, implying the self-anion de-intercalation during the rest time. Due to influence of the AB's OCV drop characteristic, LNMO cathode could not keep its OCV in a weekly basis storage time. In general, potential profile during the galvanostatic discharging show the equivalent capacities that resulting from either Ni^{4+} to Ni^{3+} or Ni^{3+} to Ni^{2+} reduction around 4.73 and 4.70 V, respectively. However, the OCV durability in Figure 71 showed the strange profiles, in which higher voltage plateau showed shorter time duration. Those OCV drop phenomena were consistent with the OCV drop tendency of AB, and the property became remarkable with AB concentration in the cathode system.

Figure 74 (b) is an attempt to summarize the schematic reaction during above constant-voltage mode for Figure 64:

① Local self-discharge reaction (reduction) at a part of the electrode.

② The other part of the system is oxidized to compensate for the reduction of ①, electrolyte decomposition followed by gas evolution. The gas evolution caused by the electrolyte decomposition is reported as an oxidation of ethylene carbonate followed by carbon dioxide evolution [111]. The reaction is well known to proceed as a ring opening and then generate CO_2 and alkyl carbonates. The generated gas was determined to be more than 96 % CO_2 in this study, which indicates gas evolution by solvent oxidation. The resulting byproduct, such as alkyl carbonates, caused the impedance to increase.

③ The local potential drop resulting from ① and ② should be recovered by re-charging because constant voltage is applied to the system. ④ Electron flow consists of the summation of ② and ③, which is equal to the saturated leak current shown in Figure 64. ⑤ The leak current denoted in ④ is balanced with the continuous redox reaction at the interface between the conductive agent and electrolyte. This current had

been reported to be observed remarkably on actual cathode systems compared to ideal electrodes [115], such as platinum and grassy carbon, in which there are no anion intercalations. Although it is difficult to explain the origin of these differences, which are generally referred to as the catalysis effect, we would like to propose that one of the key triggers of this current is the anion-intercalation property of a carbon-conductive agent. In particular, we know that there are multiple electrolyte-decomposition factors at the solid–liquid interface between a carbon agent and an electrolyte. One is electrolyte electrolysis that can be observed on both platinum and grassy-carbon electrodes, and another is the counterpart oxidation for anion deintercalation. Our experimental results, which have detailed the larger evolution of gas AB(H-C) than that of gas AB, were consistent with the above consideration, since the anion-deintercalation capacity of AB(H-C) was greater than that of AB even though their specific surface areas are similar.

Taking these findings into account, we believe that there are two processes through which gas evolution can be suppressed, as we describe herein. First is the improvement of the carbon-conductive agent(s). Initially, it is important to suppress the anion-intercalation property of the conductive agent denoted as ③ to prevent the reactions of ① and ② shown in Figure 8 . In this study, gas evolution occurred due to grassy carbon was almost negligible. Second is the increase in the oxidative duration of the electrolyte as shown in Figure 70. Since the greater durability of the electrolyte's oxidative duration can apparently decrease the reaction rate of ②, then this decrease should result in the suppression of the anion deintercalation of ①, even if anion intercalation has already taken place in Figure 74 (b) or (c). In a preliminary experiment in which FEC was used as a solvent instead of EC, the CO_2 evolution decreased by approximately 30 vol%. However, remarkably, no net gas evolution was observed, since nearly 30 vol% CO, which resulted from the electrolyte reduction on the anode, was detected at the same time. Although the electrolyte necessarily had a higher voltage window, it is also required to keep its reduction duration against the anion-intercalation properties of the carbon-conductive agents.

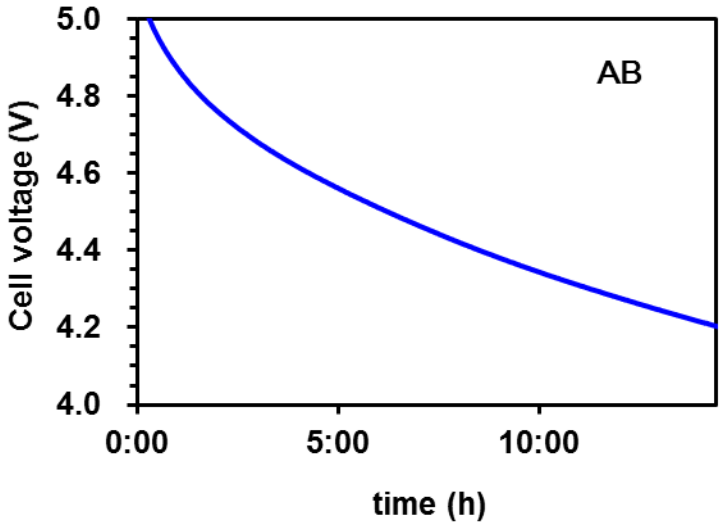

Figure 70 OCV drop of AB electrode during the 60 °C storage.

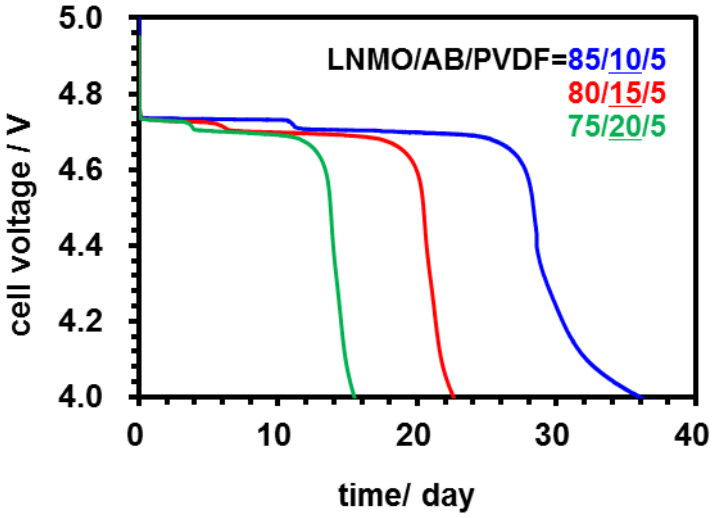

Figure 71 OCV drop of Composite High Voltage Electrodes with various AB content.

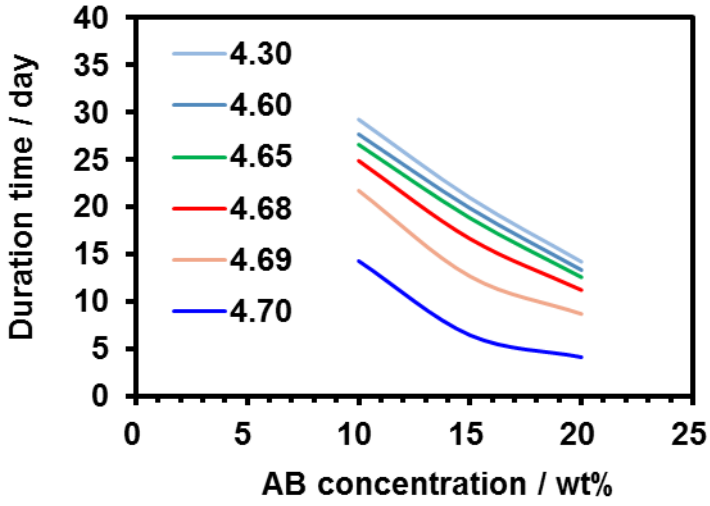

Figure 72 AB content vs. OCV duration time analyzed from Figure 71.

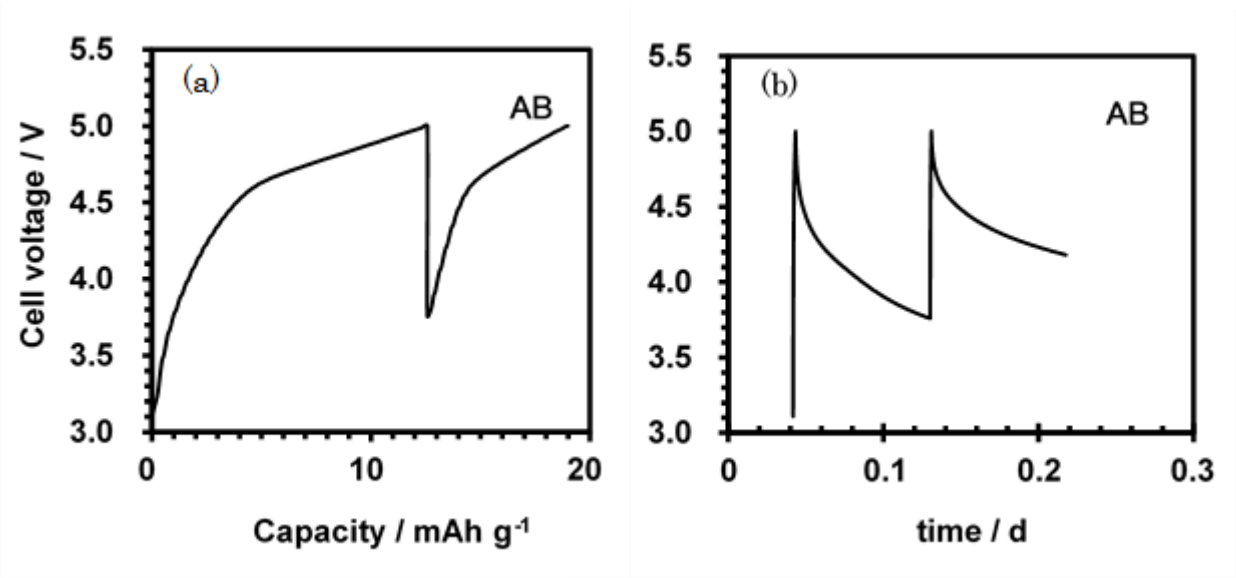

Figure 73 Self-discharge and following re-charging, potential profile vs. anion intercalation capacity (a), potential change during charging and storage time (b).

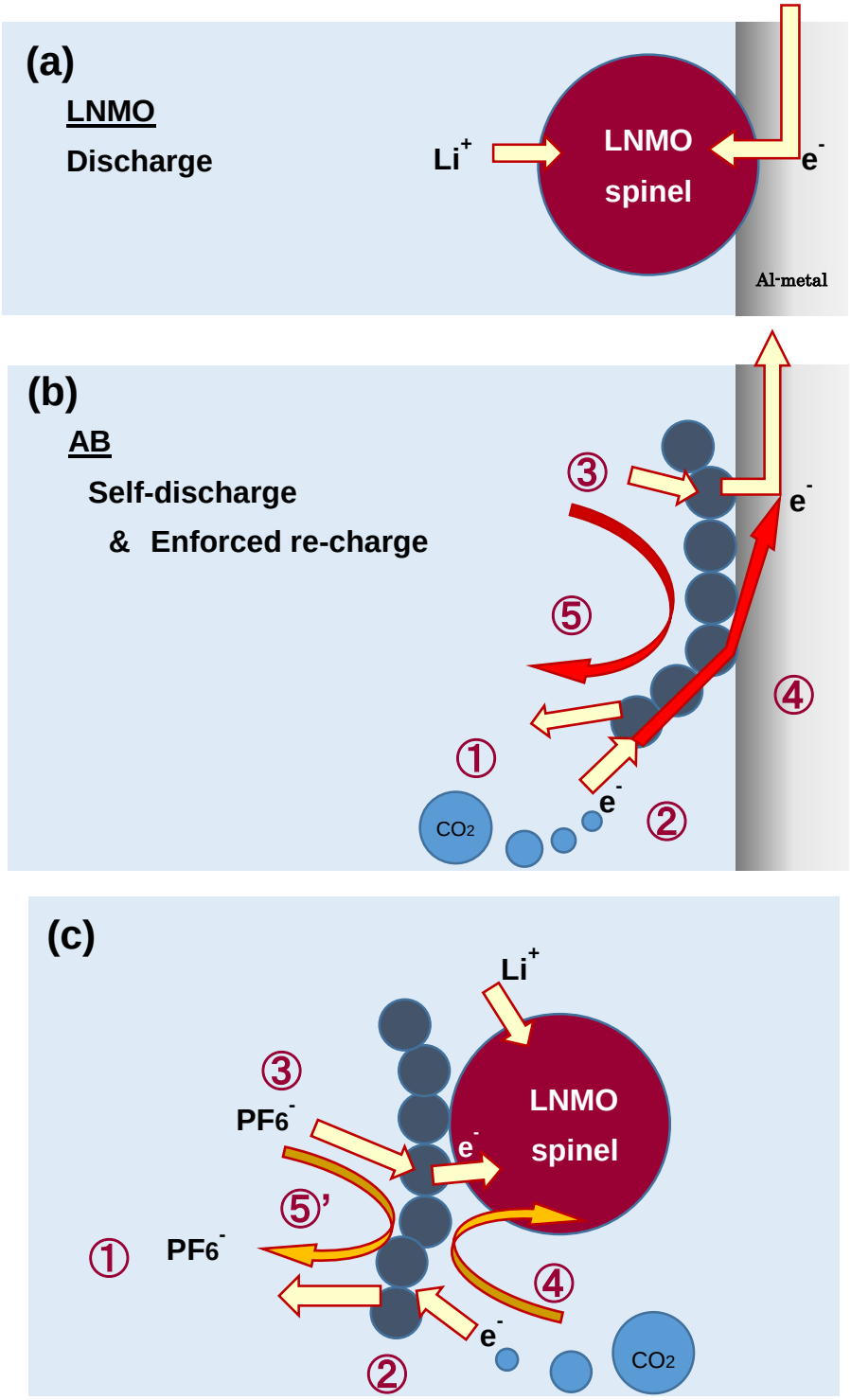

Figure 74 Schematic Image of the reaction model, general Li intercalation of LNMO (a), AB in constant voltage mode (b), and LNMO and AB interaction in open circuit environment.

Proposed model

Figure 74 presents a schematic diagram of the electrochemical reaction for the individual (a) and composite electrode of LNMO with carbon materials (c). On the discharge, lithium is inserted into the LNMO electrode from the electrolyte together with the electron supply from the current collector, and thus, the reduction of Ni ion occurs in the LNMO. The close contact of LNMO and the conductive agent caused a simultaneous redox reaction for the carbon in the high-voltage state, which might result in a local battery reaction. Because of the large capacity of LNMO, the local battery reaction continuously proceeded even if the cell is in the open-circuit state, and the carbon is kept charging by LNMO shown in Figure 74 (c). Consequently, the redox cycling on carbon ⑤’ proceeded, which accompanied with gradual LNMO OCV drop as shown in Figure 71.

Chapter 4. Summary

Interfacial reactions play a key role in the properties of lithium batteries. Therefore, understanding the existing side reactions can lead to the increase in the capacity and voltage of the active materials, and finding the new phenomena might develop the next generation batteries.

This thesis mainly consist of two key issues. One is the interfacial reaction that take place in the grain boundary in the cathode active material particles. Second is the interfacial reaction in High-Voltage complex cathode matrix. Both of them has quite closed relationship since the quest for the higher energy battery result in the increase in overcharge localization domain in the interface due to a kinetics affect even if the battery works in the conventional voltage window. On the other hand, the anomalous higher voltage reaction take place in the High-Voltage battery even in the potentially equilibrium state.

In chapter 1, the grain boundary composition of cathode active material particles, which influences battery capacity fading, were studied, and key measures to suppress capacity fading are discussed. The cracking behavior of cathode active material particles during repetitive charge–discharge cycles were one of the serious problem that result in the battery capacity deterioration. A nano size analysis revealed that the capacity fading of Li/Ni-based oxide cathode active materials is affected by the composition both at the grain boundary. Nanoscale secondary ion mass spectroscopy analysis (NanoSIMS) was performed to study this phenomenon. The research also gave the traces of a side reaction in the grain boundary crack of capacity faded particles. The byproduct in there seemed to generate by overcharge driving force, since it was accompanied with some localized overcharge phase transition.

The trigger of these undesired reaction is considered to be both the consequent crystal volume change of Li^+ intercalation and the electrical double layer in the grain boundary. Though the simply resistance decrease by the impurity elimination could not give a sufficient effect, we protect the grain boundary with fine coating. The confirmation of the coating effect was investigated with PLD epitaxial thin film. Especially, most electrochemically active crystal face, which might be a cause of capacity fade in cathode

product particle, was selected to the protection examination. The LZO coating showed the excellent protect properties both for NCM bulk and surface, in which no byproduct and no resistance increase were observed. Obtained effect was quite effective for increase in the battery life of the product scale cathode active materials. The modification with LZO showed the quite similar effect in the grain boundary, therefore, it is an interesting and important evidence that the interfacial treatment could overcome the mechanical stress by means of repetitive crystal volume change.

In chapter 2, this thesis focused on the gas evolution of high-voltage batteries. The gas evolution was observed to be caused by the interaction between the high-voltage cathode components, carbon conductive agents and the active cathode material. The trigger for this gas evolution seems to be the de-intercalation of anions from the conductive agent. During the charging state in the high-voltage region, anions once intercalate into the carbon matrix. However, simultaneously, the instability of the matrix also give rise to the self-anion de-intercalation from the matrix, and it together with the Li^+ intercalation into the cathode active material.

The intercalation and deintercalation of the anions in the carbon matrix proceed continuously and produce a pseudo-exchange current. The continuous exchange reaction might be due to the contact and thus the short circuit between the active material and conductive agent. The intercalation reaction of the anion species easily proceeds in the high-voltage region with the contact between the high-voltage cathode and carbon in the organic electrolyte, which results in continuous intercalation into the carbon matrix. The intercalation and deintercalation are related to the gas evolution, and the both crystallinity and specific surface area of the conductive agent are related to the stability in the high-voltage regions and is one of the factors affecting the gas generation. Further study with the conductive agents that is lowered its crystallinity is now under proceeding.

References

[1] K. Mizushima, P. C. Jones, P. J. Wiseman and J. B. Goodenough, Mat.Res.Bull.15(1980)783-789.

[2] E. Peled: Chapter 3, J. P Gabano Ed., Academic Press, New York (1983).

[3] R. Yazami et al., International Meeting on Lithium Batteries, Rome, April 27–29, 1982, C.L.U.P. Ed. Milan, Abstract #23.

[4] T. Ohzuku, A. Ueda, and M. Nagayama, J. Electrochem. Soc., 140 (1993) 1862.

[5] N. Yabuuchi, Y. Kawamoto, R. Hara, T. Ishigaki, A. Hiroshikawa, M. Yonemura, T. kamiyama, and S. Komaba, ACS Inorganic chemistry 52 (2013) 9131.

[6] A. Rougier, P. Gravereau, C. Delmas, J. Electrochem. Soc., 143 (1996) 1168.

[7] C. Pouillerie, E. Suard, C. Delmas, J. Solid State Chem., 158 (2001) 187.

[8] D. P. Abraham, R. D. Twesten, M. Balasubramanian, J. Kropf, D. Fischer, J. McBreen, I. Petrov, and K. Amine, J. Electrochem. Soc., 150 (2003) A1450.

[9] E. S. Lee, A. Huq, H. Y. Chang, and A. Manthiram, Chem. Mater. 24 (2012) 600.

[10] H. Konishi, K. Suzuki, S. Taminato, K. Kim, Y. Zheng, S. Kim, J. Lim, M. Hirayama, J. Y. Son, Y. Cui, and R. Kanno, J. Power Sources 269 (2014) 293.

[11] R. Qiao, Y. Wang, P. O. Velasco, H. Li, Y. S. Hu, W. Yang, J. Power Sources 273 (2015) 1120.

[12] P. Sun, Y. Liao, H. Xie, T. Chen, M. Rao, W. Li, J. Power Sources 269 (2014) 299.

[13] H. Wang, Z. Shi, J. Li, S. Yang, R. Ren, J. Cui, J. Xiao, B. Zhang, J. Power Sources 288 (2015) 206.

[14] N. Yabuuchi, K. Yoshii, S. T. Myung, I. Nakai, and S. Komaba, J. Am. Chem. Soc. 133 (2011) 4404.

[15] Z. Lu, Z. Chen, and J. R. Dahn, Chem. Mater. 15 (2003) 3214.

[16] E. Castel, E. J. Berg, M. E. Kazzi, P. Novák, and C. Villevieille, Chem. Mater. 26 (2014) 5051.

[17] J. Christensen, and J. Newman, J. Electrochem. Soc. 150 (2003) A1416.

[18] J. Christensen, and J. Newman, J. Electrochem. Soc. 151 (2004) A1977.

[19] D. B. Tow, E. Peled, and L. Burstein, J. Electrochem. Soc. 146 (1999) 824.

[20] H. Ota, Y. Sakata, A. Inoue, and S. Yamaguchi, J. Electrochem. Soc. 151 (2004) A1459.

[21] S. S. Zhang, J. Power Sources 162 (2006) 1379.
[22] M. S. Zheng, Q. F. Dong, H. Q. Cai, M. G. Jin, Z. G. Lin, and S. G. Sun, J. Electrochem. Soc. 152 (2005) A2207.
[23] M. Balasubramanian, H. S. Lee, X. Sun, X. Q. Yang, A. R. Moodenbaugh, J. McBreen, D. A. Fischer, and Z. Fu, Electrochemical and Solid-State Letters 5 (2002) A22.
[24] M. Doyle, P. Arora and R E. White, J. Electrochem. Soc. 145 (1998).
[25] A. M. Andersson, A. Henningsob, H. Siegbahb, U. Jansson, and K. Edstrom, J. Power Sources. 119-121 (2003) 522.
[26] F. Kong, R. Kstecki, G. Nadeau, X. Song, K. Zaghib, K. Kinoshita, and F. Mclarnon, J. Power Sources, 97-98 (2001) 58.
[27] D. Aurbach, M. Koltypin, and H. Teller, Langmuir 18 (2002) 9000.
[28] M. D. Levi and D. Aurbach, J. Phys. Chem. B 101 (1997) 4630.
[29] L. Larush, E. Zinigrad, Y. Goffer, and D. Aurbach, Langmuir 23 (2007) 12910.
[30] D. Aurbach, M. Moshkovich, Y. Cohen, and A. Schechter, Langmuir, 15 (1999) 2947.
[31] D. Aurbach, M. D. Levi, E. Levi, and A. Schechter, J. Phys. Chem. B 101 (1997) 2195.
[32] K. Tasaki, and S. J. Harris, J. Phys. Chem. C 114 (2010) 8076.
[33] O. Borodin, and D. Bedrov, J. Phys. Chem. C 118 (2014) 18362.
[34] A. Wuersig, W. Scheifele, and P. Novak. 154 (2007) A449.
[35] J. Lei, L. Li, R. Kostecki, R. Muller, and F. McLarnon, J. Electrochem. Soc. 152 (2005) A774.
[36] Y. Wang, X. Guo, S. Greenbaum, J. Liu and K. Amine, Electrochemical and Solid-State Letters, 4-6 (2001) A68.
[37] B. M. Meyer, N. Leifer, S. sakamoto, S. G. Greenbaum, and C. P. Grey, Electrochemical and Solid-State Letters, 8 (2005) A145.
[38] R. Dedryvere, S. Jaruelle, S. Grugeon, L. Gireaud, J. M. Tarascon, and D. Goubeau, J. Electrochem. Soc., 152 (2005) A689.
[39] E. M. Erickson, C. Ghanty, and D. Aurbach, J. Phys. Chem. Lett. 5 (2014) 3313.
[40] P. G. Bruce, A. Lisowska-Oleksiak, M. Y. Saide, and C. A. Vincent, Solid State Ionics 57 (1992) 353.
[41] A. Honders, J. M. d. Kinderen, A H. van Heeren, J. H. W. de Wit and G. H. J. Broers, Solid State Ionics 15(1985) 265.

[42] M. G. S. R. Thomas, P. G. Bruce and J. B. Goodenough, Solid State Ionics, 18/19 (1986) 794.
[43] S. Kikkawa, S. Miyazaki and M. Koizumi, J. Power Sources, 14 (1985) 231.
[44] L. Chen and J. Schoonman, Solid State Ionics, 67 (1993) 17.
[45] J. B. Bates, F. X. Hart, D. Lubben, B. S. Kwak and A. Van omeren, Proc. Of the Symposium of Rechargeable Lithium and Lithium ion Batteries, 49 -28 (1995) 342.
[46] D. Gyumard and J. M. Tarascon, J. Electrochem. Soc., 139 (1992) 937.
[47] Y. Mishima, T. Hojo, T. Nishio, A. Kajiyama, C. Moriyoshi, Y. Kuroiwa、J. Physics and Chemistry of Solids, In Press, Available online 5 August 2015, Page PCSD1500667.
[48] T. Ohzuku, S. Takeda, M. Iwanaga, J. Power Sources 81-82 (1999) 90.
[49] J. G. Swallow, W. H. Woodford, F. P. McGrogan, N. Ferralies, Y. M. Chiang, and K. J. V. Vliet, J. Electrochem. Soc., 161 (2014) F3084.
[50] Y. Itou and Y. Ukyo, J. Power Sources, 146 (2005) 39.
[51] M. Kerlau, J. A. Reimer, and E. J. Cirns, Electrochem. Communications, 7 (2005) 1249.
[52] H. Wang, Y. I. Jang, B. Huang, D. R. Sadoway, and Y. M. Chiang, J. Power Sources, 81-82 (1999) 594.
[53] K. Dokko, M. Nishizawa, S. Horikoshi, T. Itoh, M. Mohamedi, and I. Uchida, Electrochem. Solid-state Lett. 3 (2000) 125.
[54] H. Gabrisch, R. Yazami, and B. Fultz, J. Power Sources 199-121 (2003) 674.
[55] G. Chen, X. Song, and T. J. Richardson Elecrochem. Solid-State Lett. 9 (2006) A295.
[56] S. Bhattacharya, A. R. Riahi, and A. T. Alpas, J. Power Sources 196 (2011) 8719.
[57] X. Hao, X. Lin, and B. M. Brtlett, ACS Appl. Mater. Interfaces (2014).
[58] K. Jiang, X. L. Wu, Y. X. Yin, J. S. Lee, J. Kim, and Y. G. Guo, ACS Appl. Mater. Interfaces 4 (2012) 4858.
[59] J. Li, Y. Zhu, L. Wang, and C. Cao, ACS Appl. Mater. Interfaces 6 (2014) 18742.
[60] J. S. Park, X, Meng, J. W. Elam, S. Hao, C. Wolverton, C. Kim and J. Cabana, Chem. Mater. 26 (2014) 3128.
[61] R. Kanno, H. Kubo, Y. Kawamoto, T. Kamiyama, F. Izumi, Y. Takeda, and M. Takano, J. Solid State Chem., 110 (1994) 216.
[62] T. E. Hong, E. D. Jeong, S. R. Baek, M. R. Byeon, Y. S. Lee, F. N. Khan, H. S. Yang, J. Appl. Electrochem. 42 (2012) 41.

[63] J. Zheng, M. Gu, A. Genc, J. Xiao, P. Xu, X. Chen, Z. Zhu, W. Zhao, L. Pullan, C. Wang, and J. Zhang, Nano Lett., 14 (2014) 2628.

[64] Y. B. Kima, J. S. Parka, T. M. Gürb, F. Prinza, J. Power Sources, 196 (2011) 10550.

[65] Y. Suzuki, K. Kami, K. Watanabe, N. Imanishi, Solid State Ionics 278 (2015) 222.

[66] K. Sakamoto, M. Hirayama, N. Sonoyama, D. Mori, A. Yamada, K. Tamura, J. Mizuki, and R. Kanno, Chem. Mater. 21, (2009) 2632.

[67] M. M. Thackeray, C. S. Johnson, J. S. Kim, K. C. Lauzze, J. T. Vaughey, N. Dietz, D. Abraham, S. A. Hachney, W. Zeltner, and M. A. Anderson, Electrochemical Communicaiton, 5 (2003) 752.

[68] J. S. Kim, C. S. Johnson, and M. M. Thaceray, Electrochemistry Communication 4 (2002) 205.

[69] N. Taguchi, H. Sakaebe, T. Akita, K. Tatsumi, and Z. Ogumi, J. Electrochem. Soc., 161 (2014) A1521.

[70] J. Kikkawa, S. Terada, A. Gunji, T. Nagai, K. Kurashima, and K. Kimoto, J. Phys. Chem. C, 119 (2015) 15823.

[71] R. Robert and P. Novak, J. Electrochem. Soc, 162 (2015) A1823.

[72] A. Kajiyama, R. Masaki, T. Wakiyama, K. Matsumoto, and R. Kanno, LiBD 2015, Arcachon, (2015) P82.

[73] H. J. Peng, S. Urbonaite, C. Villevieille, H. Wolf, K. Leitner, and P. Novak, Arcachon France (2015), O05.

[74] J. Ni, H. Zhou, J. Chen, and X. Zhang, Electrochimica Acta, 53 (2008) 2075.

[75] H. Kawai, M. Nagata, H. Tsukamoto, and A. R. West, J. Power Sources, 81-82 (1999), 67.

[76] Q. Zhong, A. Bonakdarpour, M. Zhang, Y. Gao, and J. R. Dahn, J. Electrochem. Soc., 144 (1997) 205

[77] G. T. K Fey, W. Li, and J. R. Dahn, J. Electrochem. Soc., 151 (1994) 2279.

[78] H. Kawai, M. Nagata, H. Kageyama, H. Tsukamoto, and A. R. West, Electrocim. Acta 45 (1999) 315

[79] C. Sigala, A. Verbaere, J. L. Mansot, D. Gyuomard, Y. Piffard, and M. Tournoux, J. Solid State Chem. 132 (1997) 372.

[80] G.T-K. Fey, J.R. Dahn, M. Zhang, W. Li, J. Power Sources 68 (1997) 549.

[81] Y. Ein-Eli, W.F. Howard Jr., S.H. Lu, S. Mukerjee, J. McBreen, J. T. Vaughey, M.M. Thackeray, J. Electrochem. Soc. 145 (1998) 1238.

[82] K. Amine, H. Yasuda, and M. Yamachi, Electrochemical and Solid-State Letters, 3 (2000) 178.

[83] A. Kajiyama, K. Takada, T. Inada, M. Kouguchi, S. Kondo, and M. Watanabe, J. Electrochem. Soc., 148 (2001) A981.

[84] R. Imhof and P. Novak, J. Electrochem. Soc., 145 (1998) 1081.

[85] R. Imhof and P. Novak, J. Electrochem. Soc., 145 (1999) 1702.

[86] A Wuersig, W. Scheifele, and P. Novak, J. Electrochem. Soc., 154 (2007) A449.

[87] B. Rasch, E. Cattaneo, P. Novak, and W. Vielstich, Electrochim. Acta 36 (1991) 1397.

[88] M. Hirayama, H. Ido, K. Kim, W Cho, K Tamura, J. Mizuki, and R. Kanno, J. Am. Chem. Soc., 132 (2010) 15269.

[89] K. Kumai, H. Miyashiro, Y. Kobayashi, K. Takei and T. Iwahori, Research Reports on Central Research institute of Electric Power Industry, (2002) T99040.

[90] D. Aurbach, B. Markovsky, G. Salitra, E. Markevich, Y. Talyosef, M. Koltypin, L. Nazar, B. Ellis, and D. Kovacheva, J. Power Sources 165 (2007) 491

[91] K. J. Carroll, M. C. Yang, G. M. Veith, N. J. Dudney, and Y. S. Meng, Electrochem. and Solid-State Letters 15 (2012) A72.

[92] X. Li, Y. Chen, C. C. Nguyen, M. Nie, and B. Lucht, J. Electrochem. Soc., 161 (2014) A576.

[93] T. Noguchi, M. Uehara, Y. Kato, H. Sasaki, and K. Utsugi, 220th ECS Meet. Abstr., MA2012-02(10) (2012) 824.

[94] M. M. hantel, V. Presser, J. K. McDonough G. Feng, P. T. Cummings, Y. Gogotsi, and R. Kotz, J. Electrochem. Soc., 159 (2012) A1897.

[95] X. Xu, K. Takada, K. Watanabe, I. Sakaguchi, K. Akatsuka, B. T. Hang, T. Ohnishi, and T. Sasaki, Chem., Mater. 23 (2011) 2798.

[96] K. Takada, K. Fujimoto, T. Inada, A. Kajiyama, M. Kouguchi, S. Kondo, and M. Watanabe, Applied Surface Science, 189 (2002) 300.

[97] C. Yada, A. Ohmori, K. Ide, H. Yamasaki, T. Kato, T. Saito, F. Sagane, and Y. Iriyama, Adv. Energy Mater., 4 (2014) 130416.

[98] D. Aurbach, B. Marlovsky, Y. Talyossef, G. Salitra, H. J. Kim, and S. Choi, J. Power Source 162 (2006) 780.

[99] J. H. Park, J. M. Kim, J. S. Kim, E. G. Kim and S. Y. Lee, J. Materials Chemistry A, 1 (2013) 12441.

[100] M. Xu, N. Tsiouvaras, A. Garsuch, H. A. Gasteiger, and B. L. Lucht, J. Phys.

Chem. C 118 (2014) 7363.

[101] K. Fridman, R, Sharabi, R. Elazari, G. Gershinsky, E. Markevich, G. Salitra, D. Aurbach, A Garsuch, and J. Lampert, Electrochem. Comm.33 (2013)31.

[102] N. P. W. Pieczonka, L. Yang, M. P. Balogh, B. T. Powell, K. Chemelewski, A. Manthiram, S. A. Krachkovskiy, G. R. Goward, M. Liu and J. H. Kim, J. Physical Chem. C, 117 (2013) 22603

[103] M. Morita, T. Shibata, N. Yoshimoto, and M. Ishikawa, Electrochim. Acta 47 (2002) 2787.

[104] A. Kajiyama, A. Yoda, R. Masaki, T. Wakiyama, T. Inada, K. Matsumoto, and H. Yokota, Meet. Abstr. 17th International Meeting on Lithium Batteries, MA2014-4 (2) (2014) PO-0201.

[105] A. Jobert, Ph. Touzain and L. Bonnetain, Carbon 19 (1981) 193.

[106] S. R. Li, C. H. Chen, J. Camardese and J. R. Dahn, J. Electrochem. Soc., 160 (2013) A1517.

[107] V. Suryanarayanan, M. Noel, J. Power Sources, 94 (2001), 137.

[108] J. A. Seel and J. R. Dahn, J. Electrochem. Soc., 147 (2000) 892.

[109] A. M. Andersson, D/ P/ Abraham, R. Haasch, S. MacLaren, J. Liu and K. Amine, J. Electrochem. Soc., 149 (2002) A1358.

[110] J. S. Gnanaraj, M. D. Levi, Y. Gofer, D. Aurbach and M. Schmidt, J. Electrochem. Soc., 150 (2003) A445.

[111] K. Tasaki, K. Kanda, S. Nakamura, and M. Ue, J. Electrochem. Soc., 150 (2003) A1628.

[112] S. E. Sloop, J. K. Pugh, S. Wang, J. G. Kerr, and K. Kinoshita, Electrochem. and Solid-state letters, 4 (2001) A42.

[113] L. Xing, W. Li, C. Wand, F. Gu, M. Xu, C. Tan, and J. Yi, J. Phys. Chem. B, 113 (2009) 16596.

[114] ZView Ver. 3.3C, Scribner Associates, Inc.

[115] K. Xu, S. P. Ding, and T. R. Jow, J. Electrochem. Soc., 146 (1999) 4172.

[116] Q. Zhong, A. Bonakdarpour, M. Zhang, Yuan Gao, and J. R. Dahn, J. Electrochem. Soc., 144 (1997) 205-213.

[117] A. Kajiyama, A. Yoda, R. Masaki, T. Wakiyama, K. Matsumoto, T. Inada, H. Yokota, and R. Kanno, J. Electrochem. Soc., 162 (2015) A1516-A1522.

[118] J. A. Seel and J. R. Dahn, J. Electrochem. Soc., 147 (2000) 892-898.

[119] T. Ishihara, M. Koga, H. Matsumoto, and M. Yoshio, Electrochem. and Solid-State Letters, 10 (2007) A74-A76.

[120] S. R. Li, C. H. Chen, J. Camardese, and J. R. Dahn, J. Electrochem. Soc., 169 (2013) A1517-A1523.

[121] Y. Cho, S. Lee, Y. Lee, T. Hong, and J. Cho, Advanced Energy Materials, 1 (2001) 821.

Acknowledgements

The author would greatly appreciate to Professor Ryoji Kanno of Tokyo Institute of Technology for giving me some inspirations and important logics of this thesis. And also would like to thanks Associate Professor Masaaki Hirayama of Tokyo Institute of Technology for his continuous encouragement and useful discussions for PLD thin membrane experiments.

The author wishes to make a grateful acknowledgement to Dr. Kazutoshi Matsumoto and my colleagues in BASF TODA Battery materials, and also for members of Kanno-Hirayama laboratory for their guidance and kindness.

The author also would greatly appreciate to Dr. Kazunori Takada of National Institute for Materials Science and Professor Tatsuya Nakamura of University of Hyogo for giving me much precious knowledges in my younger days.

And also, it should be mentioned that this study had never been accomplished without my family's understanding and help.

The author wishes to thanks to "Nanotechnology Platform" (project No.12024046) of the Ministry of Education, Culture, Sports, Science and Technology (MEXT), for supporting NanoSIMS analysis of the sample interface.

The author wishes to thanks to "Innovation Center of Yamaguchi University" for supporting TEM-EDS, and its Electron diffraction measurements.

September 2015

Akihisa Kajiyama